Emerging concepts in time-resolved quantum nanoelectronics

Benoit Gaury

To cite this version:

Benoit Gaury. Emerging concepts in time-resolved quantum nanoelectronics. Physics [physics]. Université de Grenoble, 2014. English. NNT : 2014GRENY026 . tel-01163511v2

HAL Id: tel-01163511
https://theses.hal.science/tel-01163511v2

Submitted on 19 Jan 2017

UNIVERSITÉ DE GRENOBLE

THÈSE

Pour obtenir le grade de

DOCTEUR DE L'UNIVERSITÉ DE GRENOBLE

Spécialité : **Physique théorique**

Arrêté ministériel : 7 août 2006

Présentée par

Benoit GAURY

Thèse dirigée par **Xavier WAINTAL**

préparée au sein **INAC/SPSMS/GT**
et de **l'Ecole Doctorale de Physique**

Emerging concepts in time-resolved quantum nanoelectronics

Thèse soutenue publiquement le **14 octobre 2014**,
devant le jury composé de :

M. Christopher BÄUERLE
Directeur de recherche CNRS, Institut Néel, Président
M. Anton AKHMEROV
Assistant Professor, Delft University of Technology, Rapporteur
M. Christian GLATTLI
Directeur de recherche, CEA-Saclay, Rapporteur
M. Pascal DEGIOVANNI
Directeur de recherche CNRS, Ecole Normale Supérieure de Lyon, Examinateur
M. Peter SAMUELSSON
Associate Professor, Lund University, Examinateur
M. Xavier WAINTAL
Ingénieur-Chercheur, CEA-Grenoble, Directeur de thèse

ABSTRACT

With the recent technical progress, single electron sources have moved from theory to the lab. Conceptually new types of experiments where one probes directly the internal quantum dynamics of the devices are within grasp. In this thesis we develop the analytical and numerical tools for handling such situations. The simulations require appropriate spatial resolution for the systems, and simulated times long enough so that one can probe their internal characteristic times. So far the standard theoretical approach used to treat such problems numerically—known as Keldysh or NEGF (Non Equilibrium Green's Functions) formalism—has not been very successful mainly because of a prohibitive computational cost. We propose a reformulation of the NEGF technique in terms of the electronic wave functions of the system in an energy–time representation. The numerical algorithm we obtain scales now linearly with the simulated time and the volume of the system, and makes simulation of systems with $10^5 - 10^6$ atoms/sites feasible. We leverage this tool to propose new intriguing effects and experiments. In particular we introduce the concept of dynamical modification of interference pattern of a quantum system. For instance, we show that when raising a DC voltage V on an electronic Mach-Zehnder interferometer, the transient current response oscillates as $\cos(eVt/\hbar)$. We expect a wealth of new effects when nanoelectronic circuits are probed fast enough, and the tools and concepts developed in this work shall play a key role in the analysis and proposal of upcoming experiments.

ACKNOWLEDGMENTS

I am very grateful to my supervisor, Xavier Waintal, for trusting me with this topic and for his guidance during these three years. Xavier, you have been a a great advisor. Thank you for teaching me your scientific rigor, for your ever lasting enthusiasm and good mood. You are incredibly good at motivating people and making them give their best. I will keep in mind your precious quotations and pass them to future generations.

I want to thank Christopher Bäuerle, Pascal Degiovanni, Perter Samuelsson, Christian Glattli and Anton Akhmerov for reading my work and being in my PhD defense committee.

A PhD thesis is also about the lab and the office mates. I started my PhD with Oleksii Shevtsov who helped me go through the Keldysh formalism and the Green's functions. I will remember you as the guy for whom everything is "simple". I also think of Caroline Richard and Driss Badiane for our conversations about physics. Not all the questions were answered but it was definitely good brainstorming. I also spent some good time with Vladimir Mariassin who taught me a few Russian words. I hope you will keep the chocolate breaks alive. Regarding this thesis work, I thank Matthieu Santin who participated on the propagation and spreading of a voltage pulse. I also thank Joseph Weston for his nice work on the numerical aspects. You did a good job Joseph, and lots of results I can present here are because of your efforts. I appreciated our conversations about physics and life with Vladimir, it was a lot of fun.

I also thank Christoph Groth, our computer guru, for his help in my various numerical implementations, and David Luc for making a nice 3D picture for the Fabry-Perot cavity. In the lab I also spent some time with Julia Meyer and Manuel Houzet, thank you for your advice in presenting my work.

Finally I thank my parents, Marie-Elise and Jacques, and my elder brother Matthieu for their presence and constant support from the beginning of it all.

CONTENTS

Part I

GENERAL INTRODUCTION

1

INTRODUCTION (ENGLISH)

In this thesis we study the theory of low temperature nanoelectronic experiments in the GHz range and above. Keeping in mind that 1 K corresponds to 20 GHz, one finds that as the signals frequencies get higher, they become larger than the thermal background and eventually reach the internal characteristic frequencies of the systems. Conceptually new types of experiments become possible where one probes directly the internal quantum dynamics of the devices. Let us start by discussing a simple example. The device is an electronic Mach-Zehnder interferometer, as sketched in Fig. 1.1(a), implemented in a two-dimensional electron gas under high magnetic field (we will come back to it later). In the quantum Hall regime the bulk of the electronic gas is insulating and the electrons propagate only on the edges of the sample. Quantum point contacts (A and B) act as beamsplitters and make the system a two-path interferometer. The upper arm is much longer than the lower one, which implies an extra time of flight $\tau_F = L/v_g$ (with L the extra length of the upper arm with respect to the lower one and v_g the group velocity of the edge state). At $t = 0$ one raises the bias voltage applied on contact 0 and monitors the current $I_1(t)$ as a function of time. The most noteworthy feature of Fig. 1.1(b) lies in the transient regime; the current oscillates with frequency eV_b/h around a DC component (V_b final value of the DC bias). The reasoning leading to this behavior is quite straightforward. As we raise the voltage bias, the wave function originated from contact 0 accumulates a phase difference $e^{ieV_bt/\hbar}$ between its front and its rear. The device uses the delay time τ_F between

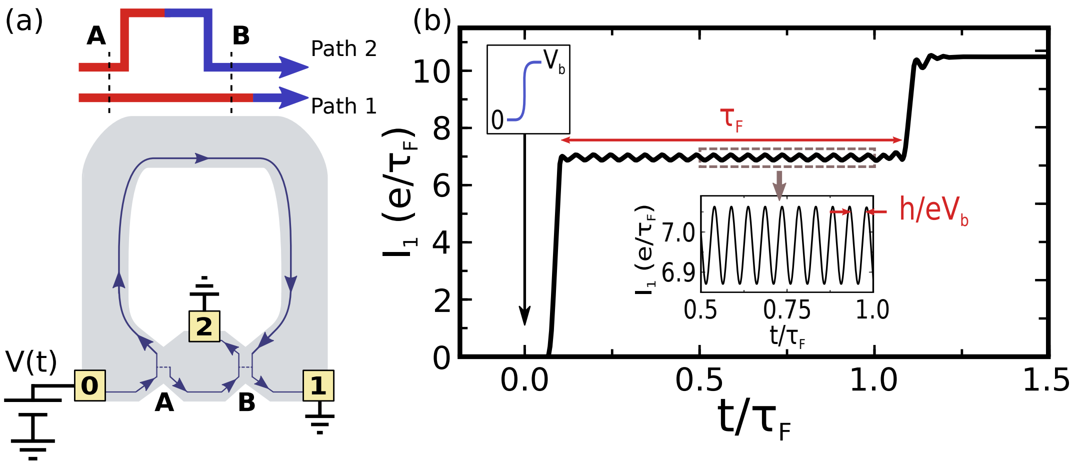

Figure 1.1 – (a) A 3 terminal Mach-Zehnder interferometer in the quantum Hall regime. The semi-transparent quantum point contacts A and B act as beamsplitters. Upper inset: schematics of the two interfering paths. (b) Transmitted current at contact 1.

the two arms to create an interference between the rear and the front of the wave function, generating the oscillatory behavior. Here we probed the time of flight of the interferometer by raising a DC potential faster than τ_F. We will later call this effect *dynamical control of interference pattern*.

The objective of this work is twofold. On the one hand, we aim to develop the analytical and numerical tools for handling the example above. This requires to simulate devices with an appropriate spatial resolution (three terminals and magnetic field in that case), for times long enough so that one can probe the internal characteristic times of the systems (the delay time τ_F in the example above). While there already exist standard approaches to investigate time-dependent quantum transport, the numerical implementation has lacked of efficiency so far. On the other hand, the kind of effect presented above calls for new concepts as we have just shown. We shall provide along this thesis with new ways of thinking the quantum transport beyond the adiabatic limit.

This introduction is organized as follows. We start with an overview of the field of mesoscopic physics to which this work belongs in section 1.1, with a particular emphasis on electronic interferometers. We will continue in section 1.2 with a review of the theoretical developments of AC and time-resolved quantum transport, and we will finally summarize our work in section 1.3 with an outline of our results for each chapter.

1.1 ELECTRONIC INTERFEROMETERS IN MESOSCOPIC PHYSICS

The domain of mesoscopic physics lies between particle physics and bulk physics. In the former, the characteristic size of a device is small enough for it to exhibit a quantum behavior while in the latter, it is large enough to present many-body features. The characteristic lengths limiting the scope of the mesoscopic domain are then the atomic scale (the angstrom) and the phase coherence length L_ϕ. This latter length represents the distance over which the phase of the electronic wave function remains unchanged. Beyond this length, all interference effects resulting from the wave-like nature of electrons are washed out, and their quantum behavior is lost [1, 2]. That is why phase coherence can be considered as the hallmark of mesoscopic physics. The rise of the domain in the 90s is related to the increased capability to reduce the dimensionality of the systems, which enhances the quantum interference effects. One defines the dimensionality of a system by comparing its characteristic size with the Fermi wave length λ_F [3]:

$$\begin{aligned}
3D&: \quad \lambda_F \ll L_x \sim L_y \sim L_z \\
2D&: \quad L_x < \lambda_F \ll L_y \sim L_z \\
1D&: \quad L_x \sim L_y < \lambda_F \ll L_z \\
0D&: \quad L_x \sim L_y \sim L_z < \lambda_F
\end{aligned}$$

In the early years, normal metals like gold were the usual material for experiments. However, the high carrier density of metals (of the order of

10^{22} cm^{-3}) has two main drawbacks. First it makes the Fermi wave length very small (of the order of the angstrom), which renders a confinement of electrons difficult even in two dimensions. The second consequence is the impossibility to use gate voltages to vary this carrier density (this would cost a huge amount of electrostatic energy). In addition, the phase coherence length of metals is of the order of the micrometer only [4]. One bright aspect of metals is that some of them become superconducting at low temperature (e.g. aluminium below 1.2 K) [5]. The superconducting phase becoming another "button" to play with. In the 1990s semiconductors started to be used. Their great advantage over metals is that one can control their lower carrier density (between 10^{14} cm^{-3} and 10^{19} cm^{-3}) by nearby metallic gates. It allows one to reduce the dimensionality of devices to $1D$ or even down to $0D$ to form quantum dots [6]. A typical example of such semiconductor structure is the two-dimensional electron gas formed at the interface of the GaAs/AlGaAs heterostructure. The formation of this electron gas is described in Fig. 1.2. Before the line-up of energy levels, the Fermi energy in the n-doped AlGaAs layer is higher than in the intrinsic GaAs layer. Electrons therefore pour in GaAs from AlGaAs leaving positively charged donors behind (plus symbols in Fig.1.2(b). This creates an electric field that bends the bands. At equilibrium the Fermi levels are aligned and a two-dimensional electron gas has formed at the GaAs/AlGaAs interface.

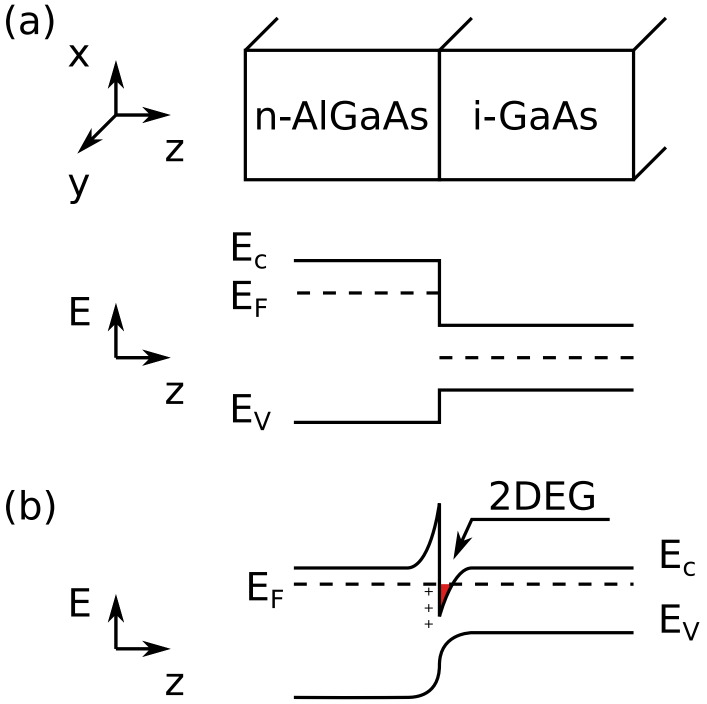

Figure 1.2 – Conduction and valence bands line-up in a heterojunction made of n-doped AlGaAs and intrinsic GaAs, (a) before and (b) after the charge transfer. Plus symbols are positively charged donors and the red area is the two-dimensional electron gas.

Although the phase of the electronic wave function is a central object for a mesoscopic physicist, one has to resort to interference processes to probe it—as it cannot be measured directly. The effects of such processes are naturally present in mesoscopic systems—for instance in the universal conductance fluctuations [7]—but can also be engineered with well defined interferometers. An important ingredient of mesoscopic experiments is the magnetic field and the associated Aharonov-Bohm effect [8]. Unlike photons, electrons are charged particles and couple to the vector potential $\vec{A}$ of the electromagnetic field even when the local magnetic field $\vec{B}$ is zero (realized when $\vec{B} = \vec{\nabla} \times \vec{A} = \vec{0}$). As an electron propagates along an identified path p, its wave function acquires a phase given by $\int_p d\vec{r} \cdot (\vec{k}(\vec{r}) + e\vec{A}(\vec{r}))$ with $\vec{k}$ the wave vector. The first term comes from the geometrical path followed by the electron, and the second one arises from its coupling with the vector potential. In 1985 Webb *et al.* observed for the first time the oscillations of the magnetoresistance with the number of magnetic flux quanta (h/e) crossing through a gold ring [9] (see Fig. 1.3). While such a system might be called a two-path interferometer, it suffers from the existence of multiple paths around the ring. One can remedy this spurious effect using, for instance, a flying qubit configuration [10]. Other types of interferometers derive from setups usually found in optics. For example Fabry-Perot cavities (two reflecting surfaces facing each other) are present in numerous devices. Such a resonator can be implemented using carbon nanotubes [11, 12], where the Shottky barriers that form at the nanotube-contact interfaces act as the reflecting barriers (role played by the mirrors in optics). As one reduces the transparency of the “mirrors”, the modes of the cavity become true bound states of the system. Such a situation is very close to the Andreev bound states occurring in Josephson junctions [13]. Fabry-Perot cavities also appear in semiconductor nanowires [14] in a similar way, or can be en-

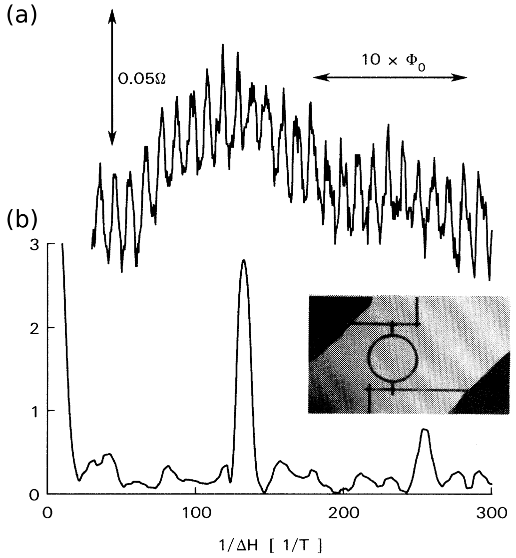

Figure 1.3 – (a) Magnetoresistance of a gold ring measured at $T = 0.01$ K. (b) Fourier power spectrum of the magnetoresistance containing peaks at h/e and $h/(2e)$. Inset: photograph of the ring with inside diameter 784 nm and wire width of 41 nm [9].

gineered in a two-dimensional electron gas in the quantum Hall regime [15]. A more involved setup is the electronic analogue of the Mach-Zehnder interferometer [16, 17, 18]. Fig. 1.4 depicts the three-terminal device used in [17], realizing a two-path interference between quantum Hall edge channels. These edge channels are separated and recombined by the quantum point contacts G_1 and G_2. A lateral gate (LG) can be used to modify the length of the lower path. This interferometer is experimentally complex to realize (central contact, high magnetic field), but it is very simple from a theoretical point of view. Indeed, as shown by the white lines in Fig. 1.4 only two paths can interfere.

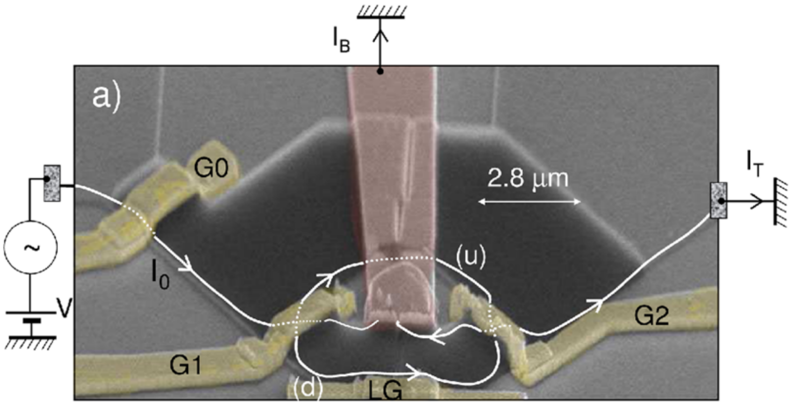

Figure 1.4 – Scanning electron microscope view of Mach-Zehnder interferometer. G0, G1, and G2 are quantum point contacts acting as beamsplitters. The white lines represent the two interfering edge channels [17].

In this context we are interested in the physics of time-resolved quantum transport in low-dimensional devices. The term "time-resolved" means that the typical duration of the time-dependent perturbations can be considered finite. We present this domain in the next section.

1.2 FROM AC TO TIME-RESOLVED QUANTUM TRANSPORT

The history of AC quantum transport probably starts in the 1960s with the prediction and measurement of the photon assisted tunneling [19]. Tien and Gordon described the quantum transport in a two-terminal nanostructure subjected to both DC and AC voltages in a simple manner. They related the DC current in presence of an AC bias voltage with frequency ω to the I-V curves $I(V)$ of this nanostructure in absence of AC voltage [20],

$$I_{dc}(V) = \sum_n p_n I(V + n\hbar\omega/e), \tag{1.1}$$

where the coefficients p_n depend on the amplitude and the shape of the AC perturbation. This effect, also known as the Tien-Gordon effect, has attracted some renewed attention recently in the context of noise measurements [21]. A motivation for such experiments lies in the possibility given by today's technology to work at frequencies higher than thermal noise

($\hbar\omega > k_B T$), allowing for the observation of the effects of quantum fluctuations on the mesoscopic apparatus (circuits amplifiers, detectors) [22]. Around the same time was the discovery of the AC Josephson effect [23, 24]. On applying a DC voltage bias V on a superconducting junction, one obtains an AC current oscillating at the frequency $2eV/h$. Other early experiments showed that it was possible to generate a DC current with the help of an AC perturbation in the absence of DC bias, which is called pumping [25, 26]. The AC perturbation can be radio-frequency voltages applied to gates using the Coulomb blockade effect [27] or, the modulation of the phase of the order parameter of superconducting electrodes using the aforementioned AC Josephson effect [28]. More recent experiments include the measurement of a quantum LC circuit [29], the statistics of the photons emitted by a tunnel junction [30, 31] and the minimization of the shot noise using multiple harmonics [32].

An important point that was recognized early by Büttiker and his collaborators is that a proper treatment of the electrostatics of a nanostructure was crucial when dealing with finite frequency quantum transport [33, 34, 35, 36, 37]. Solving naively the time-dependent Schrödinger equation incorporating the AC perturbation does not suffice to compute the correct AC current response. At finite frequency two main issues arise. On the one hand, in the non-interacting AC theory the electronic density fluctuates with space and time. As a result the current is no longer a conserved quantity. On the other hand, the particle current response (not identical to the electrical current anymore as it is in DC) depends on the voltage distribution across the nanostructure. Both problems are dealt with using nearby gates capacitively coupled to the conductors that screen the extra charges accumulated in the system. This restores the neutrality of the global system, as well as current conservation once the displacement currents (currents flowing through the plates of the capacitors) are properly included. One then finds that it is difficult to observe the internal time scales of a device as they are often smaller than the classical RC time of the above capacitors. The theory of AC quantum transport has now evolved into a field in itself which is not the focus of this work. We refer to [38] for an introduction to the (Floquet) scattering theory and to [39] for the numerical aspects.

Time-resolved quantum transport is not, *a priori*, very different from AC quantum transport. A series of seminal works on time-resolved quantum electronics showed however that the current noise associated with voltage pulses crucially depends on their actual shape (i.e. on the details of the harmonics content and of the relative phases of the various harmonics) [40, 41]. More precisely, Levitov and collaborators found that pulses of Lorentzian shape can be noiseless while other shapes are associated with extra electron-holes excitations that increase the noise of the signal. These predictions are the object of an intensive experimental activity [42, 43]. Meanwhile, other experiments are looking for various ways to construct coherent single electron sources and reproduce known quantum optics experiments with electrons. This rising field is sometimes referred to as "electronic quantum optics". Ref. [44] used a small quantum dot to make such a source [45, 46, 47, 48] which was later used in a Hanbury-Brown and Twiss setup [49], and in [50] to perform an electronic Hong-Ou-Mandel experiment. A similar source, yet working at much larger energy has been recently demonstrated in [51]. Another route used surface acoustic waves to generate a propagating confining potential that transports single electrons through the sample [52, 53]. These experiments are mostly performed in the two-dimensional gases heterostructures introduced earlier taking advantage of the small velocities (estimated around $10^4 - 10^5$ m.s^{-1} in the quantum Hall regime) and large sizes (usually several μm) to work in the GHz range. Smaller devices, such as carbon nanotubes, require the use of frequencies in the THz range. Although THz frequencies are still experimentally challenging, detection schemes in these range have been reported recently [54]. Progress in cryogenic technology makes it possible to access the high frequencies that are necessary to probe the internal time scale of nanoelectronic devices. The motivation for such work relate to the control over the orbital and spin degrees of freedom of single electrons in the wider picture of quantum computation [55], quantum information processing [56, 57], and quantum teleportation [58, 59].

1.3 OUTLINE OF THIS THESIS

In this thesis we reformulate the standard approach to time-dependent transport with a wave function in an energy–time representation. This work allows us to simulate systems containing more than 10^5 sites during 10^6 time steps going beyond the adiabatic limit and optics physics. In addition we propose new concepts and experiments. We showed the dynamical control of interference at the beginning of this introduction and we propose ways to observe it experimentally; we also propose to stop and release an electron of a charge pulse in the quantum Hall regime. Here we review the present research results accessible in each chapter.

1.3.1 *Chapter 3: Various approaches to time-resolved quantum transport*

Chapter 3 contains the theory of time-dependent transport developed in this thesis work. We consider a generic system made of several semi-infinite electrodes and a central region as sketched in Fig. 1.5. The tight-binding Hamiltonian for such a system reads

$$\hat{\mathbf{H}}(t) = \sum_{i,j} \mathbf{H}_{ij}(t) c_i^\dagger c_j, \tag{1.2}$$

where $c_i^\dagger$ (c_j) are the Fermionic creation (annihilation) operators of a one-particle state on site i. The basic objects of the Keldysh or NEGF formalism are the Retarded (G^R) and Lesser ($G^<$) Green's functions defined in the central region $\bar{0}$. Integrating out the degrees of freedom of the leads into

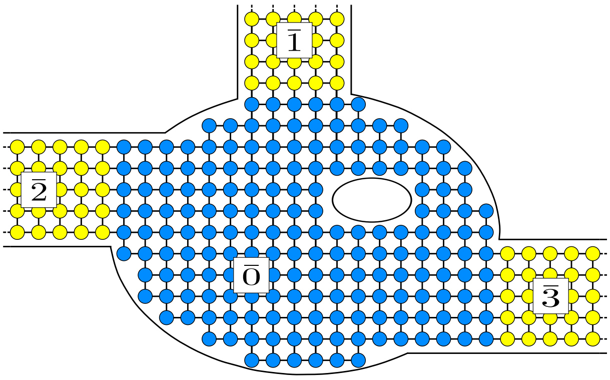

Figure 1.5 – Sketch of a generic multiterminal system where the central part $\bar{0}$ (blue circles) is connected to three semi-infinite leads $\bar{1}$, $\bar{2}$, $\bar{3}$ (yellow circles). The leads are kept at equilibrium with temperature $T_{\bar{m}}$ and chemical potential $\mu_{\bar{m}}$.

self-energy terms, one obtains effective equations of motion for G^R and $G^<$ [60, 61],

$$i\partial_t G^R(t,t') = \mathbf{H}_{\bar{0}\bar{0}}(t) G^R(t,t') + \int du\ \Sigma^R(t,u) G^R(u,t') \tag{1.3}$$

$$G^<(t,t') = \int du \int dv\ G^R(t,u)\Sigma^<(u,v)[G^R(t',v)]^\dagger \tag{1.4}$$

Introducing the wave function $\Psi_{\alpha E}(\vec{r},t)$ which depends on space $\vec{r}$ and time t as well as on the injection energy E and mode α, we find that it obeys a Schrödinger equation with an additional source term,

$$i\hbar\frac{\partial}{\partial t}\Psi_{\alpha E}(\vec{r},t) = \mathbf{H}_{\bar{0}\bar{0}}(t)\Psi_{\alpha E}(\vec{r},t) + \int du\ \Sigma^R(t-u)\Psi_{\alpha E}(u) + \sqrt{v_\alpha}\xi_{\alpha E}(\vec{r})e^{-iEt/\hbar}, \tag{1.5}$$

where $\xi_{\alpha E}(\vec{r})$ corresponds to the transverse wave function of the conducting channel α at the electrode–device interface (the number α is labeling both the different channels and the electrodes to which they are associated) and v_α is the associated mode velocity. The Lesser Green's function, hence the physical observables (density, current, ...), are then simply expressed in terms of these wave functions,

$$G^<(t,t') = \sum_\alpha \int \frac{dE}{2\pi}\, i f_\alpha(E)\Psi_{\alpha E}(t)\Psi_{\alpha E}(t')^\dagger, \tag{1.6}$$

where $f_\alpha(E)$ is the Fermi function in the electrode of channel α. The source term and mode velocities in Eq. (1.5) are standard objects of the theory of stationary quantum transport and are readily obtained, while Eq. (1.5) itself can (and will) be integrated numerically.

In addition to the reformulation of the NEGF technique, we draw explicit connections with two other approaches to time-dependent transport. We first show the equivalence of our wave function method with the scattering approach. By constructing the scattering states we find that they coincide with the wave function $\Psi_{\alpha E}(t)$ inside the central region of the system. A second connection is drawn with the partition-free approach mentioned in the previous section. We show that our wave function and the one obtained within the partition-free approach are the same.

1.3.2 *Chapter 4: Landauer formula for voltage pulses*

Chapter 4 is devoted to the derivation of a generalization of the Landauer formula to voltage pulses in multiterminal systems. We find that the number of particles is a relevant quantity for time-resolved quantum transport. Indeed we show that it is conserved and gauge invariant. We first assume a system at thermal equilibrium without net current flowing; and also that the electrons do not experience any reflection at the location of the voltage pulse. We thus find that on applying a voltage pulse $V_{\bar{m}}$ on lead $\bar{m}$, the number of particles received in lead $\bar{p}$ reads,

$$\begin{aligned} n_{\bar{p}} &= \sum_{\bar{m}} N_{\bar{p}\bar{m}} \\ N_{\bar{p}\bar{m}} &= \sum_{\beta\in\bar{p}} \sum_{\alpha\in\bar{m}} \int \frac{d\epsilon}{2\pi} |S^0_{\bar{p}\beta,\bar{m}\alpha}(\epsilon)|^2 \int \frac{dE}{2\pi} |K_{\bar{m}}(E-\epsilon)|^2 \left[f(E) - f(\epsilon)\right], \end{aligned} \tag{1.7}$$

where $S^0_{\bar{p}\beta,\bar{m}\alpha}(\epsilon)$ is the DC scattering matrix of the system in the absence of a voltage pulse, and $K_{\bar{m}}(E)$ is the harmonic content of the pulse applied on lead $\bar{m}$,

$$K_{\bar{m}}(E) = \int dt\ e^{i\phi_{\bar{m}}(t)+iEt}, \tag{1.8}$$

with $\phi_{\bar{m}}(t) = \int_{-\infty}^{t} du\ V_{\bar{m}}(u)$.

1.3.3 *Chapter 5: Strategies for numerical simulations*

Chapter 5 deals with the numerical aspects of the NEGF and wave function (WF) approaches discussed in chapter 3. We propose several schemes (three for NEGF and four for the wave function) illustrated with the propagation of a voltage pulse along a one-dimensional chain. The relative comparison of the relevant implementations is given in Table 1.1. We denote N the total number of sites of the central region and S the number of sites connected to the electrodes. WF-D is our best algorithm and is the one used in the rest of this work. While the numerical resolution of Eq. (1.5) is done without difficulty, the integration over energy is often a source of complication. In particular, we show that contributions with vanishing velocity make it difficult to obtain particle conservation. We show that one recovers particle conservation when integrating over a long time. We propose to filter these contributions of low energy to recover a Fermi level physics expected in the long-time limit. Finally we discuss our choice of boundary

Algorithm	CPU (1D)	Estimated CPU (2D)	Scaling of CPU
WF-D	1	10^4	$(t/h_t)N_E[N+\gamma tS]$
WF-B	40	4.10^7	$(t/h_t)N_E[N+(t/h_t)S^2]$
GF-C	10^4	10^{12}	$(t/h_t)^2S^3$ (*)
GF-A	10^5	10^{14}	$(t/h_t)^2S^2N$ (*)

Table 1.1 – Computation time in seconds for a calculation performed on a single computing core. 1D case: 20 sites (for GF-A the calculation has been done in parallel using 48 cores in order to obtain the results within a few hours). 2D case: 100×100 sites. The CPU time is estimated from the scaling laws except for WF-D where calculations of similar sizes could be performed. Third column: typical scaling of the computing time. A notable additional difference between the WF and GF methods is that the GF methods (*) only provide the observables at one given time per calculation while the WF methods give the full curve in one run. The typical number of energy points N_E is 100 in this example.

conditions in the electrodes and we justify our model of an abrupt voltage drop used in this work.

1.3.4 *Chapter 6: Propagation and spreading of a charge pulse*

We study in chapter 6 the propagation and spreading of a charge pulse created by a voltage pulse applied to an Ohmic contact. We begin with a scattering approach for a one-dimensional chain, and continue in the continuous limit to find that charge density and current oscillations follow the spreading of the charge pulse. We show that these oscillations spread diffusively. We perform additional numerical simulations using the one-dimensional edge states of the quantum Hall regime as shown in Fig. 1.6. Specifically we show that the spreading of the envelope of the charge density $\Delta X(t)$ spreads linearly in time. More precisely we identify two contribu-

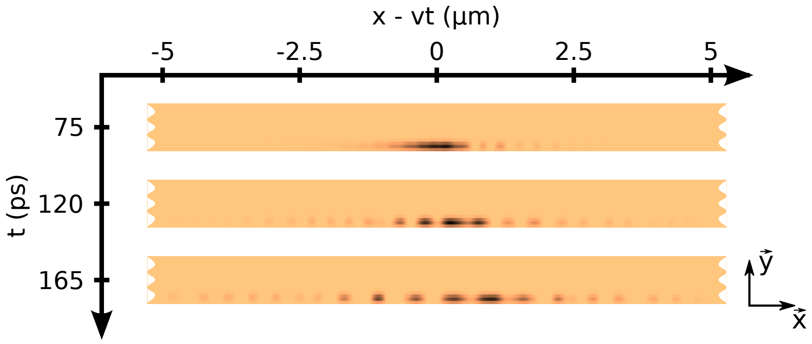

Figure 1.6 – Carte de la densité de charge liée à l'étalement d'un pulse de charge créé par un pulse de tension Lorentzien, $V(t) = V_p/(1+(t/\tau_p)^2)$, avec amplitude $V_p = 0.5i$ mV et durée $\tau_p = 5$ ps.

tions to the spreading. On the one hand, the calculations in the continuous limit gives,

$$\Delta X\Big|_{qu} = \frac{t}{m^* \Delta X_0}, \tag{1.9}$$

with ΔX_0 the initial spatial extension of the pulse, and m^* the electron effective mass. On the other hand, a more classical picture based on a "hydrodynamic" reasoning leads to

$$\Delta X\Big|_{cl} = \frac{\bar{n} t}{m^* \Delta X_0}, \tag{1.10}$$

where $\bar{n}$ is the number of particles injected by the voltage pulse. The transport properties of a voltage pulse applied to an Ohmic contact are then related to its quantum nature that is bounded by $\bar{n} \approx 1$.

1.3.5 *Chapter 7: Dynamical control of interference using voltage pulses in the quantum regime*

We start to study the time-dependent transport beyond the adiabatic limit in chapter 7. To this end we first consider a Fabry-Perot cavity as it is the simplest system to exhibit a characteristic time scale (the time of flight inside the cavity). Such a cavity is made out of a quantum wire and two barriers as sketched in Fig. 1.7. We find that on applying voltage pulses faster than the time of flight of the cavity, we can dynamically control the relative phases of the paths taken by the electrons. This regime of fast pulses allows for the restoration of the interferences in presence of large bias voltages, negative currents with respect to the direction of propagation of the voltage pulse, oscillations of the total transmitted charge with the total number of injected electrons. All our numerical findings are supported by analytical

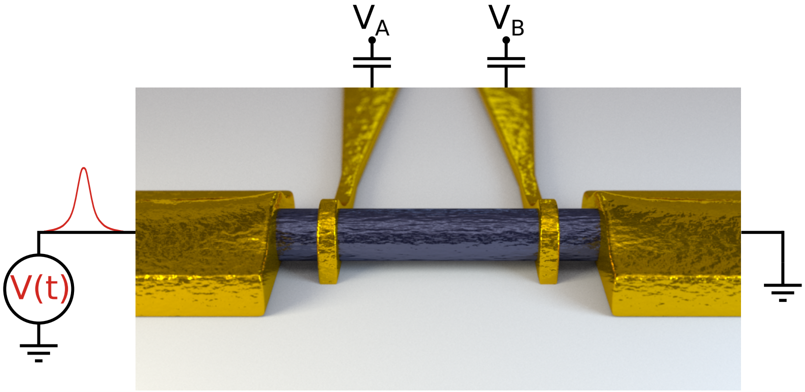

Figure 1.7 – Schematic of our setup, a quantum wire connected to two electrodes. Two barriers A and B separated by a distance L are placed along the wire and a Gaussian voltage pulse $V(t)$ is sent from the left. The barriers are characterized by the barrier heights (V_A and V_B).

derivations based on the formalism for voltage pulses developed in chapter 4. We also validate our analysis further with the full scale simulation of an electronic Mach-Zehnder interferometer in the quantum Hall regime.

We generalize the concept of dynamical control of interference to the case of raising a DC bias voltage in the interferometers discussed above. We show that on applying a DC voltage V_b to an electronic interferometer, there exists a universal transient regime where the current oscillates at frequency eV_b/h. This effect is analogous to the AC Josephson effect.

1.3.6 *Chapter 8: Numerical simulations of time-resolved quantum transport in the quantum Hall effect regime*

In chapter 8 we first present the procedure that should be followed to perform numerical simulations in the quantum Hall regime, and continue with the requirements specific to time-dependent transport. In particular we come back to the integration over energy necessary to compute observables (see Eq. (1.6)). We find that the filtering potential engineered in chapter 5 needs to be adapted to the peculiar density of states of a system in the quantum Hall regime. In the last section of the chapter we discuss the interplay between the modification of the path followed by the electrons and the quantum dynamics of the electronic flow in a quantum circuit. Specifically, we study the propagation of charge pulses through the edge states of a two-dimensional electron gas in the quantum Hall regime. By sending radio-frequency (RF) excitations on a top gate capacitively coupled to the electron gas, we manipulate these edge states dynamically. We find that a fast RF change of the gate voltage can stop the propagation of the charge pulse inside the sample. This effect is intimately linked to the vanishing velocity of bulk states in the quantum Hall regime and the peculiar connection between momentum and transverse confinement of Landau levels. We propose new possibilities for stopping, releasing and switching the trajectory of charge pulses in quantum Hall systems.

2

INTRODUCTION (FRANÇAIS)

Nous étudions dans cette thèse les expériences de nanoélectronique à basse température dans la gamme de fréquences du GHz et au-delà. En ayant à l'esprit que 1 K correspond à 20 GHz, on comprend que plus les fréquences des signaux s'accroissent, plus elles surpassent le bruit thermique, et finalement atteignent les fréquences caractéristiques des systèmes. Des expériences conceptuellment nouvelles deviennent possibles, où l'on sonde directement la dynamique quantique interne des systèmes. Commençons par discuter d'un exemple simple. Le système est un interféromètre électronique de Mach-Zehnder, comme schématisé en Fig. 2.1(a), réalisé dans un gaz bi-dimensionnel d'électrons sous fort champ magnétique (nous y reviendrons plus tard). Dans le régime d'effet Hall quantique l'intérieur du gaz d'électrons est isolant et les électrons se propagent uniquement sur les bords du système. Les points de contact quantique (A et B) jouent le rôle de lame semi-réfléchissante et font de ce système un interféromètre à deux chemins. Le bras supérieur est beaucoup plus long que le bras inférieur, ce qui implique un temps de vol additionnel $\tau_F = L/v_g$ (avec L la longueur supplémentaire du bras supérieur par rapport au bras inférieur, et v_g la vitesse de groupe de l'état de bord). À $t = 0$ on monte la tension appliquée au contact 0 et on enregistre le courant $I_1(t)$ en fonction du temps. Le point notoire de la figure Fig. 1.1(b) réside dans le régime transitoire. Le courant oscille à la fréquence eV_b/h autour d'une composante DC (V_b valeur finale de la tension DC). Le rasionnement menant à ce comportement est plutôt direct. Lorsque l'on monte la tension, la fonction d'onde du contact 0 accu-

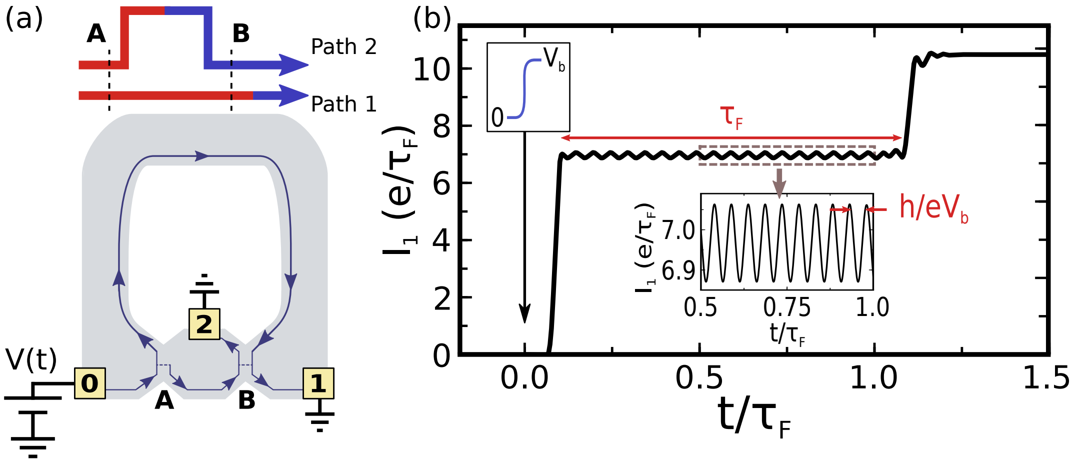

Figure 2.1 – (a) Un interféromètre Mach-Zehnder à 3 terminaux dans le régime d'effet Hall quantique. Les points de contacts quantiques A et B jouent le rôle de miroir semi-réfléchissant. Insert: schéma des deux chemins qui interfèrent. (b) Courant transmis au contact 1.

mule une différence de phase $e^{ieV_b t/\hbar}$ entre l'avant et l'arrière. Le système utilise le retard τ_F entre les deux bras pour créer une interférence, générant le comportement oscillant. Ce que l'on a fait ici consiste à sonder le temps de vol de l'interféromètre en montant une tension DC plus vite que τ_F. Plus tard, nous appellerons cet effet *modification dynamique du motif d'interférence.*

L'objectif de ce travail de thèse est double. D'une part, nous développons les outils analytiques et numériques pour traiter l'exemple ci-dessus. Cela requiert de simuler des systèmes dont la résolution spatiale est appropriée (trois contacts et du champ magnétique dans ce cas), pendant des temps suffisamment longs pour sonder les temps caractéristiques des systèmes (ici le temps de vol τ_F). Alors qu'il existe déjà des méthodes standards pour étudier le transport quantique dépendent du temps, l'implémentation numérique a manqué d'efficacité jusqu'à maintenant. D'autre part, le genre d'effet présenté avec notre exemple fait appel à de nouveaux concepts. Tout au long des pages qui suivent, nous allons donner de nouvelles façons de penser le transport quantique au-delà de la limite adiabatique.

Cette introduction est organisée comme suit. Nous commençons par une vue d'ensemble de la physique mésoscopique, à laquelle ce travail appartient, en section 2.1, où l'on portera l'accent sur les interféromètres électroniques. Nous poursuivons en section 2.2 avec une revue des développements théoriques du transport quantique AC et résolu en temps, et nous finirons par un résumé des chapitres en section 2.3.

2.1 INTERFÉROMÈTRES ÉLECTRONIQUES EN PHYSIQUE MÉSOSCOPIQUE

Le domaine de la physique mésoscopique se situe entre la physique des particules et la physique des systèmes massifs. Dans le premier cas, la taille caractéristique d'un système est suffisamment petite pour exhiber un comportement quantique. Dans le second cas, le système est suffisamment large pour avoir les caractéristiques d'un comportement à N corps. Les tailles caractéristiques délimitant le cadre de la physique mésoscopique sont donc l'échelle atomique (l'angstrom) et la longueur de cohérence de phase L_ϕ. Cette dernière longueur représente la distance sur laquelle la phase d'une fonction d'onde électronique reste inchangée. Au-delà de cette longueur, tous les effets résultant de la nature ondulatoire des électrons disparaissent et leur comportement quantique est perdu [1, 2]. C'est pourquoi la longueur de cohérence de phase peut être considérée comme la marque principale de la physique mésoscopique. L'essor de ce domaine dans les années 90 est lié à la capacité croissante de réduire la dimensionnalité des systèmes, ce qui renforce les effets quantiques. On définit la dimensionnalité d'un système en comparant ses dimensions caractéristiques à la longueur d'onde de Fermi λ_F [3]:

$$\begin{aligned} 3D&: \quad \lambda_F \ll L_x \sim L_y \sim L_z \\ 2D&: \quad L_x < \lambda_F \ll L_y \sim L_z \\ 1D&: \quad L_x \sim L_y < \lambda_F \ll L_z \\ 0D&: \quad L_x \sim L_y \sim L_z < \lambda_F \end{aligned}$$

Dans les premières années de la physique mésoscopique, des métaux ordinaires comme l'or étaient utilisés pour les expériences. Cependant, la haute densité de porteurs de charge des métaux (de l'ordre de 10^{22} cm^{-3}) a deux inconvénients majeurs. D'abord cela implique une longueur d'onde de Fermi très petite (de l'ordre de l'angstrom), ce qui rend difficile le confinement des électrons même en deux dimensions. Le second désavantage est qu'il est impossible d'utiliser des tensions de grille pour faire varier cette densité (cela coûterait une énergie électrostatique considérable). De plus la longueur de cohérence de phase dans les métaux est seulement de l'ordre du micromètre [4]. Un aspect intéressant émerge cependant en ce que certains métaux sont supraconducteurs à basse température (par exemple l'aluminium en-dessous de 1.2 K) [5]. La phase du supraconducteur est alors un nouveau bouton avec lequel on peut jouer. Dans les années 90 on a commencé à utiliser des structures à base de semiconducteurs. Le grand avantage des semiconducteurs sur les métaux est leur plus faible densité de porteurs de charge (entre 10^{14} cm^{-3} et 10^{19} cm^{-3}) que l'on peut contrôler par des grilles métalliques. Ceci permet de résuire la di-

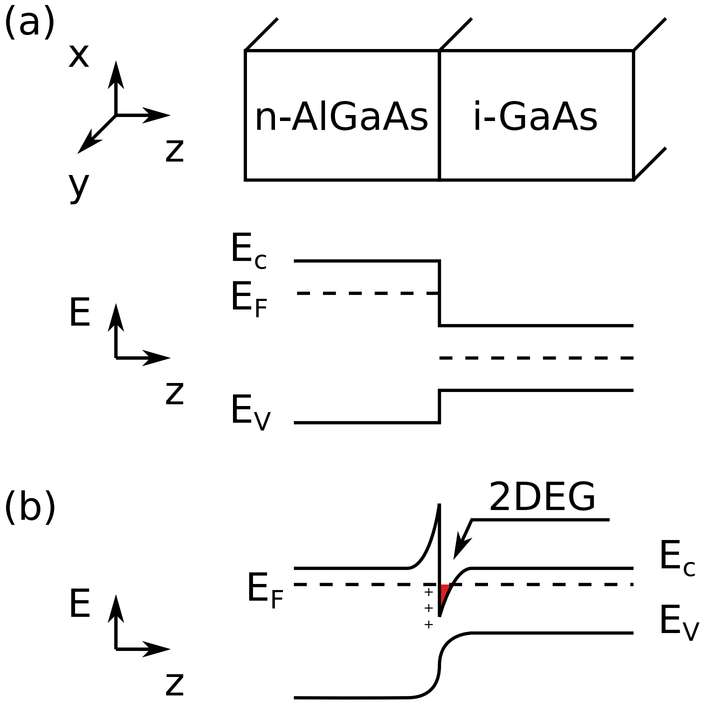

Figure 2.2 – Alignement des bandes de conduction et de valence dans une hétérojonction formée de AlGaAs dopé n et de GaAs intrinsèque, (a) avant et (bC après le transfert de charges. Les symboles "plus" indiquent les donneurs ionisés, et la zone rouge est le gaz bi-dimensionnel d'électrons.

mensionnalité des systèmes à $1D$ ou même jusqu'à $0D$ pour former des boîtes quantiques [6]. Un exemple typique de telles structures semiconductrices est le gaz bi-dimensionnel d'électrons qui se forme à l'interface de l'hétérostructure GaAs/AlGaAs. La formation de ce gaz d'électrons est décrite en Fig. 2.2. Avant l'alignement des niveaux d'énergie, l'énergie de Fermi dans la couche d'AlGaAs dopé n est plus haute que celle de la couche de GaAs intrinsèque. En conséquence, les électrons se déversent dans GaAs à partir de AlGaAs, laissant derrière eux les donneurs ionisés (symboles plus dans Fig.2.2(b)). Ce phénomène crée un champ électrique qui plie les bandes. À l'équilibre les niveaux de Fermi sont alignés et un gaz d'électrons bi-dimensionnel se trouve à l'interface GaAs/AlGaAs.

Bien que la phase de la fonction d'onde électronique soit un objet central pour le physicien mésoscopiste, on ne peut pas la mesurer directement et l'on doit recourir à des processus d'interférence pour la sonder. Les effets de tels processus sont naturellement présents dans les systèmes étudiés—on peut penser par exemple aux fluctuations universelles de conductances [7]—mais peuvent aussi être construits par des interféromètres bien définis. Un ingrédient important des expériences est le champ magnétique et l'effet Aharonov-Bohm associé [8]. Contrairement aux photons, les électrons sont des particules chargées et se couplent au potentiel vecteur $\vec{A}$ du champ électromagnétique, même lorsque le champ magnétique local $\vec{B}$ est nul (réalisé quand $\vec{B} = \vec{\nabla} \times \vec{A} = \vec{0}$). Lorsqu'un électron se propage suivant un chemin p, sa fonction d'onde aquiert une phase donnée par $\int_p d\vec{r} \cdot (\vec{k}(\vec{r}) + e\vec{A}(\vec{r}))$ avec $\vec{k}$ le vecteur d'onde. Le premier terme vient du chemin géométrique parcouru par l'électron, et le second provient du couplage avec le potentiel vecteur. En 1985 Webb *et al.* ont observé pour la première fois les oscillations de

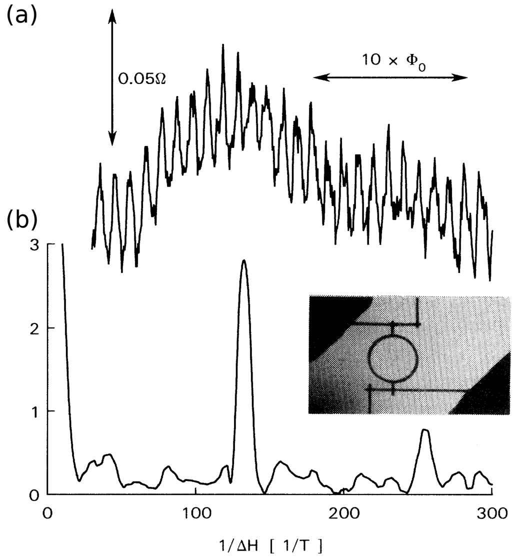

Figure 2.3 – (a) Magnétorésistance d'un anneau d'or mesurée à $T = 0.01$ K. (b) Densité spectrale de puissance de la magnétorésistance contenant des pics à h/e et $h/(2e)$. Insert: photographie de l'anneau dont le diamètre interne est 784 nm la largeur du fil est 41 nm [9].

magnétorésistance avec le nombre de quanta de flux (h/e) traversant un anneau d'or [9] (voir Fig. 2.3). Alors qu'un tel système pourrait être vu comme un interféromètre à deux chemins, l'existence de multiples chemins autour de l'anneau complexifie la situation. Ce problème peut être résolu en utilisant, par exemple, une configuration de qubit volant [10]. D'autres types d'interféromètres proviennent de montages que l'on trouve usuellement en optique. Par exemple, les cavités Fabry-Perot (deux surfaces réfléchissantes face-à-face) sont présentes dans de nombreux systèmes. De tels résonateurs peuvent être créés en utilisant des nanotubes de carbone [11, 12], où les barrières Shottky se formant à l'interface nanotube–contact jouent le rôle de barrières réfléchissantes (les miroirs en optique). Lorsqu'on réduit la transparence des "miroirs", les modes de la cavité deviennent de véritables états liés. Une telle situation est alors très proche des états liés d'Andreev qui apparaissent dans les jonctions Josephson [13]. Les cavités Fabry-Perot sont aussi présentes dans les nanofils semiconducteurs [14] de façon similaire, mais peuvent aussi être créées dans un gaz bi-dimensionnel d'électrons en régime d'effet Hall quantique [15]. Un système un peu plus complexe est l'analogue électronique de l'interféromètre de Mach-Zehnder (vu rapidement au début de cette introduction) [16, 17, 18]. La Fig. 2.4 montre le système à trois terminaux utilisé dans [17], réalisant une interférence entre deux canaux de bord de l'effet Hall. Ces canaux de bord sont séparés puis recombinés par les deux points de contact quantique G_1 et G_2. Une grille latérale (LG) permet de modifier la longueur du chemin inférieur. Cet interféromètre expérimentalement complexe à réaliser (le contact central est complexe à obtenir, un fort champ magnétique est nécessaire), est cependant très simple du point de vue théorique. En effet il n'y a vraiment que deux chemins qui interfèrent , comme le montrent les lignes blanches en Fig. 2.4.

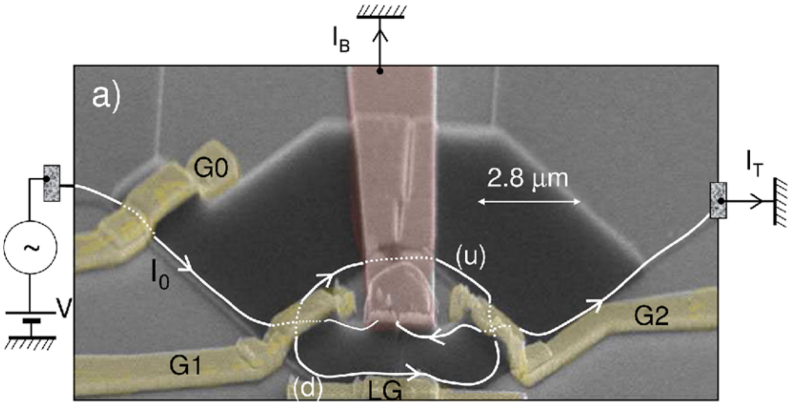

Figure 2.4 – Vue au microscope électronique à balayage d'un interféromètre de Mach-Zehnder. G0, G1, et G2 sont les points de contact quantiques jouant le rôle de lame séparatrice. Les lignes blanches représentent les canaux de bord qui interfèrent [17].

Dans ce contexte nous nous intéressons à la physique du transport résolu en temps dans les structures à basses dimensions. Le terme "résolu en temps" signifie que l'extension temporelle des perturbations peut être considérée comme finie. Nous présentons ce domaine dans la prochaine section.

2.2 DU TRANSPORT QUANTIQUE AC À RÉSOLU EN TEMPS

L'histoire du transport quantique AC commence probablement dans les années 1960 avec la prédiction et la mesure de l'effet tunnel photo-assisté [19]. Tien et Gordon ont décrit le transport quantique dans des nanostructures à deux terminaux soumises à des tensions DC et AC d'une façon simple. Ils ont relié le courant DC en présence d'une tension AC à la fréquence ω aux courbes I-V de la nanostructure en l'absence de tension AC [20],

$$I_{dc}(V) = \sum_n p_n I(V + n\hbar\omega/e), \tag{2.1}$$

où les coefficients p_n dépendent de l'amplitude et de la forme de la perturbation AC. Cet effet, aussi connu sous le nom d'effet Tien-Gordon, a attiré de nouveau l'attention récemment dans le contexte des mesures de bruit [21]. Une motivation pour de telles expériences réside dans la possibilité que l'on a aujourd'hui de travailler à des fréquences dépassant le bruit thermique ($\hbar\omega > k_B T$). Cela permet d'observer les effets des fluctuations quantiques sur l'appareillage de mesure (amplificateurs, détecteurs) [22]. Au même moment l'effet Josephson AC était découvert [23, 24]. L'application d'une tension continue V sur une jonction supraconductrice fournit un courant oscillant à la fréquence $2eV/h$. D'autres expériences ont montré que l'on pouvait générer un courant DC par le biais d'une tension AC en l'absence de tension continue. On apelle cela le pompage [25, 26]. La tension AC peut être un signal radio-fréquence appliqué sur des grilles en utilisant le blocage de Coulomb [27] ou bien, la modulation de la phase du paramètre d'ordre d'électrodes supraconductrices en usant de l'effet Josephson AC [28]. Plus récemment des expériences ont été réalisées sur un circuit LC quantique [29], sur la statistique des photons émis par une jonction tunnel [30, 31] et sur la minimisation du bruit de grenaille en mélengeant plusieurs harmonique [32].

Büttiker et ses collaborateurs ont remarqué très tôt qu'un bon traitement de l'électrostatique d'une nanostructure était crucial dans l'étude du transport quantique à fréquence finie [33, 34, 35, 36, 37]. Résoudre naivement l'équation de Schrödinger dépendente du temps en incorporant une perturbation AC ne suffit pas pour calculer la réponse en courant d'un système. À fréquence finie, deux difficultés principales surgissent. D'une part, dans la théorie AC sans interaction la densité électronique fluctue dans l'espace et le temps. Il en résulte que le courant n'est plus une grandeur conservée. D'autre part, le courant de particule (maintenant différent du courant électrique contrairement au cas DC) dépend de la distribution de la tension à travers la nanostructure. Ces deux problèmes ont été résolus en considérant que des grilles couplées capacitivement au système permettent d'écranter la charge qui s'y est accumulée. Ceci permet de restaurer la neutralité globale du système, ainsi que la conservation du courant une fois que l'on a pris en compte les courants de déplacement (courants circulant à travers les grilles). On remarque alors qu'il est difficile d'observer les échelles de temps caractéristiques d'un système parce qu'elles sont souvent plus petites que le temps RC classique des capacités mentionnées. La théorie du transport quantique AC a évolué pour devenir un domaine bien défini. Nous reportons le lecteur à [38] pour une introduction à la théorie de la diffusion (Floquet), et à [39] pour les aspects numériques. Ce domaine n'est cependant pas l'objet de ce travail comme nous allons le voir maintenant.

Le transport quantique résolu en temps n'est, *a priori*, pas très différent du transport quantique AC. Cependant, une série de travaux fondateurs portant sur l'électronique résolue en temps a montré que le bruit en courant associé à des pulses de tension dépend précisément de leur forme (c'est-à-dire de leur contenu en harmoniques et des phases entre celles-ci) [40, 41]. Plus précisément, Levitov et ses collaborateurs ont trouvé que des pulses de forme Lorentzienne peuvent être non bruités, alors que d'autres formes impliquent l'excitation de paires électron–trou qui augmentent le bruit du signal. Ces prédictions font l'objet d'une intense activité expérimentale [42, 43]. Pendant ce temps, d'autres expériences cherchent des moyens de construire des sources d'électrons uniques cohérents et reproduisent, avec des électrons, des expériences connues d'optique quantique. Ce domaine naissant est parfois dénommé "optique électronique quantique". Ref. [44] utilise une boîte quantique pour réaliser une telle source [45, 46, 47, 48] qui sera plus tard utilisée dans un montage Hanbury-Brown and Twiss [49], ainsi que dans [50] pour faire une expérience de Hong-Ou-Mandel. Une source similaire, mais fonctionnant à plus grande énergie, a récemment été réalisée [51]. Une autre voie prise dans [52, 53] consiste à utiliser des ondes acoustiques de surface pour générer un potentiel de confinement permettant de transport les électrons uniques à travers l'échantillon. Ces expériences sont principalement réalisées dans les gaz bi-dimensionnels d'électrons présentés plus tôt. La motivation pour de tels travaux repose principalement sur le fait que le contrôle des degrés de liberté de l'électron (spin et orbital) est au coeur des problématiques de calcul quantique [55], d'information quantique [56, 57] et de téléportation [58, 59].

2.3 RÉSUMÉ DES CHAPITRES

Dans cette thèse, on reformule l'approche standard du transport dépendent du temps à l'aide d'une fonction d'onde dans une représentation énergie–temps. Ce travail nous permet de simuler des systèmes contenant 10^5 sites durant 10^6 pas de temps. On peut alors aller au-delà de la limite adiabatique et de l'optique. Nous proposons aussi de nouveaux concepts. On a déjà évoqué le contrôle dynamique du motif d'interférence en introduction, on donne aussi des moyens de l'obsever expérimentalement. On propose aussi d'arrêter et de relâcher un électron dans un gaz bi-dimensionnel d'électrons en régime d'éffet Hall quantique. Nous présentons ici une vue d'ensemble de ces résultats.

2.3.1 *Chapitre 3: Différentes approches du transport quantique résolu en temps*

Le chapitre 3 contient la théorie du transport dépendent du temps développée dans cette thèse. Nous considérons un système arbitraire infini constitué de plusieurs électrodes semi-infinies et d'une région centrale, comme décrit en Fig. 2.5. Le Hamiltonien de liaisons fortes d'un tel système est

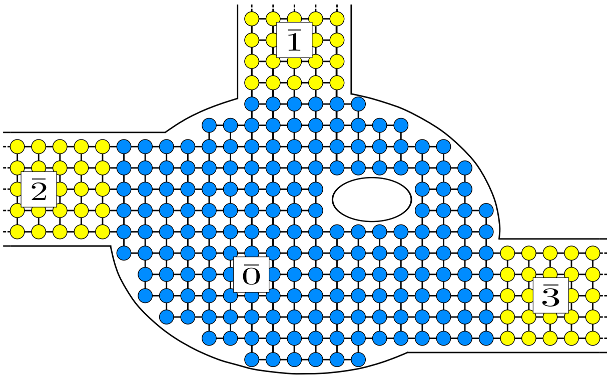

Figure 2.5 – Schéma d'un système multiterminaux où la région central $\bar{0}$ (cercles bleus) est connectée à trois contacts semi-infinis $\bar{1}$, $\bar{2}$, $\bar{3}$ (cercles jaunes). Les électrodes sont à l'équilibre à la température $T_{\bar{m}}$ et le potentiel chimique $\mu_{\bar{m}}$.

$$\hat{\mathbf{H}}(t) = \sum_{i,j} \mathbf{H}_{ij}(t) c_i^\dagger c_j, \tag{2.2}$$

où $c_i^\dagger$ (c_j) sont les opérateurs Fermioniques de création (annihilation) d'un état à une particule au site i. Les objets de base du formalisme Keldysh, où des Fonctions de Green hors Equilibre (NEGF), sont la fonction de Green Retardée (G^R) et Lesser ($G^<$) définies sur la région centrale $\bar{0}$. Après intégration des degrés de liberté des électrodes dans des termes de self-energie, on obtient les équations de mouvement suivantes pour G^R et $G^<$ [60, 61],

$$i\partial_t G^R(t,t') = \mathbf{H}_{\bar{0}\bar{0}}(t) G^R(t,t') + \int du\, \Sigma^R(t,u) G^R(u,t') \tag{2.3}$$

$$G^<(t,t') = \int du \int dv\, G^R(t,u) \Sigma^<(u,v) [G^R(t',v)]^\dagger \tag{2.4}$$

Nous introduisons la fonction d'onde $\Psi_{\alpha E}(\vec{r},t)$ qui dépend de l'espace $\vec{r}$ et du temps t, ainsi que de l'énergie d'injection E et du mode α. Cette fonction d'onde obéit à l'équation de Shcrödinger avec un terme de source additionnel

$$i\hbar \frac{\partial}{\partial t} \Psi_{\alpha E}(\vec{r},t) = \mathbf{H}_{\bar{0}\bar{0}}(t) \Psi_{\alpha E}(\vec{r},t) + \int du\, \Sigma^R(t-u) \Psi_{\alpha E}(u) + \sqrt{v_\alpha} \xi_{\alpha E}(\vec{r}) e^{-iEt/\hbar}, \tag{2.5}$$

où $\xi_{\alpha E}(\vec{r})$ correspond à la fonction d'onde transverse du mode α à l'interface électrode–système central et v_α est la vitesse du mode. La fonction de Green $G^<$, et donc les observables physiques (densité, courant, ...), sont simplement exprimées en termes de ces fonctions d'onde:

$$G^<(t,t') = \sum_\alpha \int \frac{dE}{2\pi}\, i f_\alpha(E) \Psi_{\alpha E}(t) \Psi_{\alpha E}(t')^\dagger, \tag{2.6}$$

où $f_\alpha(E)$ est la fonction de Fermi dans l'électrode du canal α. Le terme de source et les vitesses des modes dans Eq. (2.5) sont des objets standards de la théorie du transport quantique stationnaire, tandis que Eq. (2.5) peut être (et sera) intégrée numériquement.

En plus de cette reformulation du formalisme NEGF, nous faisons des connexions avec deux autres approches du transport dépendent du temps. D'abord on montre l'équivalence entre notre fonction d'onde et la méthode dite de "scattering". En construisant les états de diffusion, nous trouvons qu'ils coïncident avec la fonoction d'onde $\Psi_{\alpha E}(t)$ à l'intérieur de la région centrale du système. On rapporche aussi notre méthode de l'approche dite sans partition ("partition-free"). Nous montrons que les fonctions d'onde obtenues dans les deux cas sont les mêmes.

2.3.2 *Chapitre 4: Une formule de Landauer pour pulses de tensions*

Dans ce chapitre nous dérivons une généralisation de la formule de Landauer au cas des pulses de tension dans des systèmes multiterminaux. Nous trouvons que la quantité du nombre de particules est tout à fait pertinente dans le cadre du transport résolu en temps. En effet nous montrons qu'elle est conservée et invariante de jauge. Nous supposons un système initialement à l'équilibre thermodynamique sans courant net, et que les électrons ne subissent aucune réflexion à l'emplacement du pulse de tension. Nous trouvons alors que suite à l'application d'un pulse de tension $V_{\bar{m}}$ sur le contact $\bar{m}$, le nombre de particules reçues dans le contact $\bar{p}$ s'écrit,

$$\begin{aligned} n_{\bar{p}} &= \sum_{\bar{m}} N_{\bar{p}\bar{m}} \\ N_{\bar{p}\bar{m}} &= \sum_{\beta\in\bar{p}} \sum_{\alpha\in\bar{m}} \int \frac{d\epsilon}{2\pi} |S^0_{\bar{p}\beta,\bar{m}\alpha}(\epsilon)|^2 \int \frac{dE}{2\pi} |K_{\bar{m}}(E-\epsilon)|^2 \left[f(E) - f(\epsilon)\right], \end{aligned} \tag{2.7}$$

où $S^0_{\bar{p}\beta,\bar{m}\alpha}(\epsilon)$ est la matrice de scattering DC du système en l'abscence de pulse de tension, et $K_{\bar{m}}(E)$ est le contenu en harmoniques du pulse de tension:

$$K_{\bar{m}}(E) = \int dt\ e^{i\phi_{\bar{m}}(t) + iEt}, \tag{2.8}$$

avec $\phi_{\bar{m}}(t) = \int_{-\infty}^t du\ V_{\bar{m}}(u)$.

2.3.3 *Chapitre 5: Stratégies de simulations numériques*

Le chapitre 5 traite des aspects numériques des approches NEGF et fonction d'onde (WF) discutées au chapitre 3. Nous proposons ici plusieurs schémas numériques (trois pour NEGF et quatre pour la fonction d'onde) illustrés par la propagation d'un pulse de tension le long d'une chaine 1D. Une comparaison des implémentations les plus notables est donnée dans le Tableau 2.1. On note N le nombre total de sites dans la région centrale, et S le nombre de sites connectés aux électrodes. WF-D est notre meilleur algorithme et est celui que l'on utilise dans le reste de ce travail. Alors que la résolution numérique de Eq. (2.5) ne pose pas de difficulté, l'intégration en énergie est souvent source de complications. Nous montrons que des contributions ayant une vitesse très faible rendent difficile l'obtention de la conservation du nombre de particules. On montre que cela est normal de par les phénomènes physiques en jeu et que l'on retrouve la conservation du nombre de particules si l'on intègre Eq. (2.5) sur un intervalle de temps suffisamment long. Nous proposons de filtrer ces contributions de basse énergie afin de retrouver la physique du niveau de Fermi attendue dans la limite des longs temps. Enfin nous discutons de notre choix de conditions aux bords dans les électrodes et justifions le modèle de chute de tension abrupte (localisée dans l'espace) utilisé ici.

Algorithme	CPU (1D)	CPU estimé(2D)	Evolution CPU
WF-D	1	10^4	$(t/h_t)N_E[N+\gamma tS]$
WF-B	40	4.10^7	$(t/h_t)N_E[N+(t/h_t)S^2]$
GF-C	10^4	10^{12}	$(t/h_t)^2S^3$ (*)
GF-A	10^5	10^{14}	$(t/h_t)^2S^2N$ (*)

Table 2.1 – Temps en secondes d'un calcul réalisé sur un seul processeur. Cas 1D: 20 sites (pour GF-A le calcul a été fait en parallèle sur 48 processeurs afin d'obtenir le résultat en quelques heures).Cas 2D: 100×100 sites. Le temps CPU est estimé à partir de la loi d'échelle sauf pour WF-D où le calcul avec des tailles de systèmes comparables a pu être effectué. Troisième colonne: loi d'échelle du temps de calcul. Une différence notoire entre les méthodes WF et GF est que les méthodes GF (*) ne fournissent les observables qu'à un temps donné par calcul, tandis que les méthodes WF fournissent une courbe somplète en une seule simulation. Le nombre de valeurs d'énergie typique N_E est de 100 dans cet exemple.

2.3.4 *Chapitre 6: Propagation et étalement d'un pulse de charges*

Dans le chapitre 6 nous étudions la propagation et l'étalement d'un pulse de charges créé par un pulse de tension appliqué à un contact Ohmique.

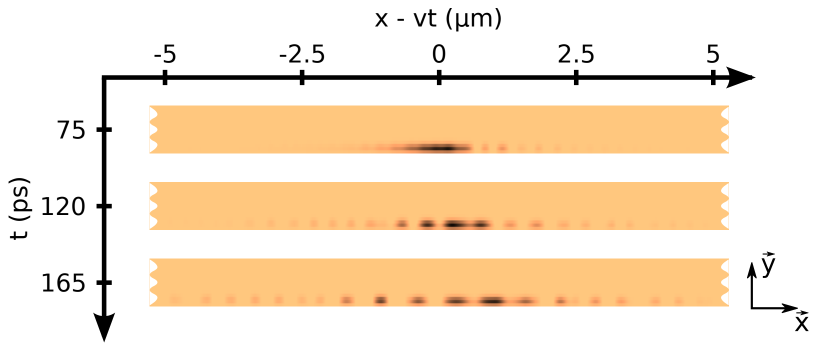

Figure 2.6 – Carte de la densité de charge liée à l'étalement d'un pulse de charge créé par un pulse de tension Lorentzien, $V(t) = V_p/(1 + (t/\tau_p)^2)$, avec amplitude $V_p = 0.5$ mV et durée $\tau_p = 5$ ps.

Nous commençons par calculer la matrice de scattering d'une chaine 1D, puis nous passons à la limite continue pour trouver que des oscillations de densité de charge et de courant suivent l'étalement du pulse de charges. Nous montrons alors que ces oscillations s'étalent de façon diffusive.

Nous visualisons ensuite l'étalement du pulse de charge dans un gaz bi-dimensionnel d'électrons dans le régime d'effet Hall quantique, comme décrit en Fig. 2.6. De façon plus spécifique nous montrons que l'étalement de l'enveloppe de la densité de charge $\Delta X(t)$ s'étale linéairement avec le temps. On identifie deux contributions à cet étalement. D'une part, le calcul de la fonction d'onde électronique après l'application du pulse donne

$$\Delta X\Big|_{qu} = \frac{t}{m^* \Delta X_0}, \tag{2.9}$$

où ΔX_0 est l'étalement spatial initial du pulse, et m^* est la masse effective des électrons. D'autre part, une vison plus classique basée sur un raisonnement "d'hydrodynamique" amène

$$\Delta X\Big|_{cl} = \frac{\bar{n} t}{m^* \Delta X_0}, \tag{2.10}$$

où $\bar{n}$ est le nombre de particules injectées par le pulse de tension. Les propriétés de transport du pulse de tension appliqué à un contact Ohmique sont alors reliées étroitement à sa nature quantique dont la frontière est déterminée par $\bar{n} \approx 1$.

2.3.5 *Chapitre 7: Contrôle dynamique d'interférence utilisant des pulses de tension dans le régime quantique*

On commence à véritablement étudier le transport dépendent du temps au-delà de la limite adiabatique dans le chapitre 7. On considère dans un premier temps une cavité Fabry-Perot ; c'est le système le plus simple possédant un temps caractéristique (le temps de vol à l'intérieur de la cavité). Un tel système est constitué d'un fil quantique et de deux barrières comme représenté en Fig. 2.7. On trouve que l'application d'un pulse de tension

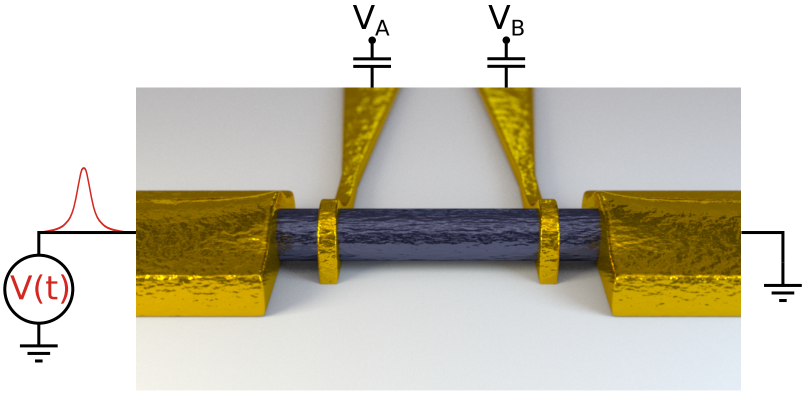

Figure 2.7 – Schéma de notre système, un fil quantique connecté à deux électrodes. Deux barrières A et B séparées d'une distance L sont placées le long du fil et un pulse de tension Gaussien $V(t)$ est envoyé du contact de gauche. Les barrières sont caractérisées par leur hauteur V_A et V_B.

plus court que le temps de vol à l'intérieur de la cavité permet de contrôler les phases relatives entre les différents chemins pris par les électrons. Ce régime de pulses courts permet de restaurer les interférences même avec une amplitude de pulse grande devant l'acart moyen entre niveaux de la cavité, de faire apparaître un courant négatif par rapport à la direction de propagation du pulse, et de faire osciller le nombre de particules transmises avec le nombre de particules injectées. Ce travail combine des dérivations analytiques basées sur le chapitre 4 et des calculs numériques. Nous validons notre analyse sur une simulation à grande échelle d'un interféromètre de Mach-Zehnder dans le régime d'effet Hall quantique.

On généralise enfin le concept de contrôle dynamique d'interférence au cas de la montée d'une tension continue dans les interféromètres discutés ci-dessus (cas présenté au tout début de cette introduction). On montre que l'application d'une tension DC V_b aux interféromètres précédents donne lieu à un régime transitoire universel où le courant oscille à la fréquence eV_b/h. Cet effet est analogue à l'effet Josephson AC observé dans les jonctions supraconductrices.

2.3.6 *Chapitre 8: Simulations numériques du transport quantique résolu en temps dans le régime d'effet Hall quantique.*

Dans le chapitre 8 nous présentons dans un premier temps la procédure à suivre pour réaliser des simulations numériques dans le régime d'effet Hall quantique. On spécifie ensuite l'étude au transport dépendent du temps. En particulier nous revenons sur l'intégration sur l'énergie d'injection nécessaire au calcul des observables (voir Eq. (2.6)). En effet le filtrage mis en place au chapitre 5 n'est plus adapté du fait de la grande densité d'états ne se propageant pas (cas très spécial de l'effet Hall quantique)

Dans la dernière section du chapitre on dicute de l'interaction entre la modification dynamique du chemin emprunté par les électrons et la dy-

namique du flux d’électrons dans un circuit quantique. Précisément, on étudie la propagation d’un pulse de charges via les états de bord d’un gaz bi-dimensionnel d’électrons sous régime d’effet Hall quantique. L’envoi d’excitations radio-fréquences (RF) sur des grilles couplées capacitivement au gaz d’électrons nous permet de manipuler dynamiquement ces états de bord. On trouve qu’un changement RF rapide de la tension de grille peut arrêter la propagation d’un pulse de charge à l’intérieur du système. Cet effet est intimement lié à la vitesse nulle des états se trouvant au milieu du système dans le régime d’effet Hall quantique, ainsi qu’à la connexion particulière entre vecteur d’onde et confinement transverse des niveaux de Landau. Nous proposons une nouvelle possibilité de stopper, relâcher et modifier la trajectoire de pulses de charges dans l’effet Hall.

Part II

FORMALISM AND NUMERICAL ALGORITHMS FOR TIME-DEPENDENT QUANTUM TRANSPORT

3

VARIOUS APPROACHES TO TIME-RESOLVED QUANTUM TRANSPORT

We construct the theory of time-dependent transport with an emphasis on drawing connections between various possible approaches. We begin with a short review on the theoretical and numerical aspects of the time-resolved quantum transport in section 3.1. We introduce our general model in section 3.2 and the basic equations of the non-equilibrium Green's function formalism in section 3.3, and then proceed in section 3.4 with the introduction of the time-dependent wave function as a mathematical artifact to reformulate the NEGF formalism. Section 3.5 is devoted to a constructive presentation of the scattering approach. We show that it is strictly identical to the wave function of section 3.4. We also find that the NEGF approach is equivalent to the partition-free approach introduced in [62] and further developed in [63]. Finally, in section 4 we apply the formalism that has been introduced to voltage pulses in multiterminal systems. We generalize the Landauer-Büttiker formula to the number of transmitted particles, and find that this quantity is relevant in time-dependent transport (conserved and gauge invariant). Sections 3.1, 3.2 and 3.3 contain known material, while sections 3.4, 3.5 are original results.

3.1 THEORY AND NUMERICAL SIMULATIONS OF TIME-RESOLVED QUANTUM TRANSPORT

While simulations of the time-dependent Schrödinger equation are almost as old as quantum mechanics itself [64], time-resolved quantum transport requires that two additional difficulties to be dealt with: the statistical physics of the many-body problem (the minimum level being the inclusion of the Pauli principle and the thermal equilibrium of the leads) and the fact that quantum transport takes place in *infinite* systems. Early numerical simulations of time-resolved quantum transport were based on a seminal paper by Caroli, Combescot, Nozières, and Saint-James [65] which sets the basis of the Non-Equilibrium Green's Function (NEGF) formalism. This work, itself based on the Keldysh formalism [66] in a one-dimensional situation, was used in [67] to study resonant tunneling of a single level. Caroli *et al.* originally presented their theory with a DC problem. They considered a two-lead system where the central region is initially not coupled to the leads (in which perturbations are applied). The electrical connection between the leads and the central region is switched on adiabatically, leading to the flow of a time-independent current. Although the partition of the infinite system can be placed anywhere, it is usually placed at the central region–lead interface. The theory was later completed with the addition of electron–phonon interactions [68, 69]. The formalism for a generic mesoscopic system was established by Jauho, Wingreen and Meir [70, 71] extending the stationary formalism put forward by Wingreen and Meir [72] which itself extends the original work of [65]. The time-dependent NEGF approach described in these papers is still the basis of most numerical works today. In a complementary approach, namely the scattering matrix theory [73], one focuses on the incoming and outgoing states originating from the leads and propagating through the central region (instead of focusing on the central region and using the leads as boundary conditions). The latter approach, more involved from a numerical point of view, is more favored for analytical calculations. Considering that the NEGF formalism is 25 years old, the number of publications on the subject is rather small. This is due in part to the fact that it only recently became possible to perform experiments in the relevant regimes (i.e. GHz frequencies at dilution fridge temperatures), and also to the extreme computational cost of a direct integration of the NEGF equations. Many recent works describe various strategies for integrating the integro-differential equation of the NEGF formalism, including direct approaches [74, 75, 76], a semi analytical approach [77], a parametrization of the analytical structure of the equations [78] and a recursive approach [79]. The important issue of properly dealing with electron-electron interactions has been discussed in [80, 81, 82, 83]. Alternative approaches to NEGF include a direct treatment of quantum master equations for the single-electron density matrix [84, 85], or the use of a "stroboscopic" wave packet basis [86, 87]. Perhaps the most advanced alternative to NEGF is the partition-free approach introduced by Cini [62] in the early 80s. In this approach, instead of "integrating out" the electrodes' degrees of freedom, as it is done in NEGF, the central region and the leads are treated on the same footing. One starts at $t = 0$ with the exact density matrix at equilibrium, and follows the states of the system as they are driven out of equilibrium by the time-dependent perturbation. This approach can be followed with Green's functions [88, 89] or more conveniently directly at the wave function level [63, 90, 91].

To the best of our knowledge, the best performance so far has been obtained with the partition-free approach where around 100 sites could be studied (the direct NEGF simulations are usually confined to 10 sites or fewer). The wave function approach leverages the fact that calculations of the electric current do not require all of the information contained within Green's functions. Nevertheless, all these techniques suffer from the fact that the systems are intrinsically infinite which brings non local (in time) terms into the dynamical equations. An interesting approach followed in [89] consists of ignoring these non local terms and considering a large finite system instead.

We consider a quadratic discrete Hamiltonian for an open system

$$\hat{\mathbf{H}}(t) = \sum_{i,j} \mathbf{H}_{ij}(t) c_i^\dagger c_j \tag{3.1}$$

where $c_i^\dagger$ (c_j) are the usual Fermionic creation (annihilation) operators of a one-particle state on site i. The site index i includes all the degrees of freedom present in the system, i.e. space but also spin, orbital (s,p,d,f) and/or electron/hole (superconductivity), so that a large number of situations can be modeled within the same framework. The system consists of a central region, referred to as $\bar{0}$ connected to M semi-infinite leads labeled $\bar{1}...\bar{M}$ as depicted in Fig. 3.1. $\mathbf{H}(t)$ is formally an infinite matrix and can be viewed as consisting of sub-blocks $\mathbf{H}_{\bar{m}\bar{n}}$,

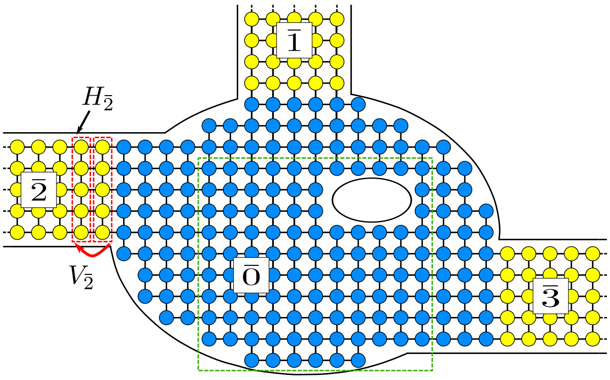

Figure 3.1 – Sketch of a generic multiterminal system where the central part $\bar{0}$ (blue circles) is connected to three semi-infinite leads $\bar{1}$, $\bar{2}$, $\bar{3}$ (yellow circles). The leads are kept at equilibrium with temperature $T_{\bar{m}}$ and chemical potential $\mu_{\bar{m}}$. The dashed green line indicates a region that will be integrated out in Fig. 5.1.

$$\mathbf{H} = \begin{pmatrix} \mathbf{H}_{\bar{0}\bar{0}} & \mathbf{H}_{\bar{0}\bar{1}} & \mathbf{H}_{\bar{0}\bar{2}} & \dots \\ \mathbf{H}_{\bar{1}\bar{0}} & \mathbf{H}_{\bar{1}\bar{1}} & 0 & \dots \\ \mathbf{H}_{\bar{2}\bar{0}} & 0 & \mathbf{H}_{\bar{2}\bar{2}} & \dots \\ \dots & \dots & \dots & \dots \end{pmatrix} \tag{3.2}$$

A semi-infinite lead $\bar{m}$ is itself a periodic system where a unit cell is described by a Hamiltonian matrix $H_{\bar{m}}$ which is coupled to the neighboring cells by the coupling matrix $V_{\bar{m}}$,

$$\mathbf{H}_{\bar{m}\bar{m}} = \begin{pmatrix} H_{\bar{m}} & V_{\bar{m}} & 0 & 0 & \dots \\ V_{\bar{m}}^\dagger & H_{\bar{m}} & V_{\bar{m}} & 0 & \dots \\ 0 & V_{\bar{m}}^\dagger & H_{\bar{m}} & V_{\bar{m}} & \dots \\ \dots & \dots & \dots & \dots & \dots \end{pmatrix} \tag{3.3}$$

While the time dependence of the device region $\mathbf{H}_{\bar{0}\bar{0}}(t)$ can (and will) be arbitrary, the leads are only subject to homogeneous time-dependent voltages so that $\mathbf{H}_{\bar{m}\bar{m}}(t) = w_{\bar{m}}(t)1_{\bar{m}} + \mathbf{H}_{\bar{m}\bar{m}}(t=0)$ ($1_{\bar{m}}$ is the identity matrix in lead m). Following standard practice, we perform a unitary gauge transformation,

$$\hat{W} = \exp\Big(-i \sum_{i \in \bar{m}} \phi_{\bar{m}}(t) c_i^\dagger c_i \Big), \tag{3.4}$$

on the Hamiltonian with $\phi_{\bar{m}}(t) = \int_{-\infty}^{t} du\ w_{\bar{m}}(u)$ being the integral of the time-dependent voltage. After the gauge transformation, we recover time-independent Hamiltonians for the leads while the matrix elements that connect the lead to the central part now acquire a time-varying phase:

$$\mathbf{H}_{\bar{m}\bar{0}} \to e^{i\phi_{\bar{m}}(t)} \mathbf{H}_{\bar{m}\bar{0}}. \tag{3.5}$$

The quantum mechanical aspects being properly defined, we are left to specify the statistical physics; each lead is supposed to remain at thermal equilibrium with a chemical potential $\mu_{\bar{m}}$ and a temperature $T_{\bar{m}}$. Note that the thermal equilibrium condition is most simply expressed for time-independent leads, i.e. after the gauge transformation. This particular choice of boundary condition is significant and its physical meaning will be discussed in more depth in section 5.5.

3.3 KELDYSH FORMALISM AND NON-EQUILIBRIUM GREEN'S FUNCTIONS

Here we summarize the basic equations of the time-dependent NEGF formalism [72, 70] that constitutes the starting point of our approach. We refer to the original [60] or more recent references [39, 61] for a derivation of these equations.

3.3.1 *Equations of motion for the Retarded (G^R) and Lesser ($G^<$) Green's functions*

The basic objects under consideration are the Lesser $\mathcal{G}^<(t,t')$ and Retarded $\mathcal{G}^R(t,t')$ Green's functions of the system,

$$\mathcal{G}^R_{ij}(t,t') = -i\theta(t-t')\langle\{c_i(t), c_j^\dagger(t')\}\rangle\,, \tag{3.6}$$

$$\mathcal{G}^<_{ij}(t,t') = i\langle c_j^\dagger(t') c_i(t)\rangle\,, \tag{3.7}$$

where the operator $c_i(t)$ corresponds to c_i in the Heisenberg representation and $\theta(t)$ is the Heaviside function. For a quadratic Hamiltonian, the Retarded Green's function takes a simple form in terms of the "first quantization" evolution operator of the system,

$$\mathcal{G}^R(t,t') = -i\theta(t-t')U(t,t') \tag{3.8}$$

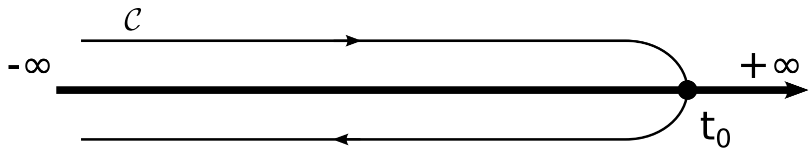

Figure 3.2 – Closed time contour $\mathcal{C}$ due to Schwinger. The system evolves forward on the upper branch from $t = -\infty$ to $t = t_0$, and backward on the lower branch until $t = +\infty$.

where the unitary evolution operator $U(t, t')$ verifies $i\partial_t U(t, t') = \mathbf{H}(t)U(t, t')$ and $U(t, t) = 1$. The physical observables can be written simply in terms of the Lesser Green's function. For instance the particle current between sites i and j reads,

$$I_{ij}(t) = \mathbf{H}_{ij}(t)\mathcal{G}^{<}_{ji}(t, t) - \mathbf{H}_{ji}(t)\mathcal{G}^{<}_{ij}(t, t), \tag{3.9}$$

while local electron density is $\rho_i(t) = -i\mathcal{G}^{<}_{ii}(t, t)$. Suppose that one is interested in the quantum propagation of a wave packet $\Psi(t)$ according to the Schrödinger equation $i\partial_t \Psi(t) = \mathbf{H}\Psi(t)$ with an initial condition given by $\Psi(t = t_0) = \Psi_0$. Then one finds that $\Psi(t)$ is simply given by $\Psi(t) = i\mathcal{G}^R(t, t_0)\Psi_0$. In other words, the Retarded Green's function encodes the quantum propagation of a wave packet. The Lesser Green's function, on the other hand, captures the remaining many-body / statistical physics aspects: the Pauli principle, the finite temperature properties of the leads and the fact that the "initial conditions", say an electric voltage pulse, are given in terms of macroscopic quantities (as opposed to an initial microscopic wave packet) and spread over a finite time window.

The significant difference between (thermodynamic) equilibrium and non-equilibrium theories is the assumption made in the former that the system comes back to its ground state long after the switching on and off of interactions. In the latter the final state depends on the specifics of the switching procedure. Since one needs to know the final state in order to compute statistical averages, Schwinger initially proposed to take it the same as the initial one [92]. In other words, we let the system evolve from $t = -\infty$ to some time of interest, t_0 in Fig. 3.2, and then rewind the evolution back to $t = -\infty$. This construction makes the time evolve on a contour $\mathcal{C}$ that distinguishes between forward and backward evolution as depicted in Fig. 3.2. The concept of the time contour was later used by Kadanoff and Baym [93], and Keldysh [66]. The doubling of the degrees of freedom is the price to pay to use this trick. As a result the typical object of interest of the theory is the 2×2 Green's function matrix,

$$\hat{G}(t, t') = \begin{pmatrix} \mathcal{G}^{T}(t, t') & \mathcal{G}^{<}(t, t') \\ \mathcal{G}^{>}(t, t') & \mathcal{G}^{\tilde{T}}(t, t') \end{pmatrix} \tag{3.10}$$

The submatrices $\hat{G}_{ij}(t, t')$ refer to the position of t and t' on the contour $\mathcal{C}$. These positions are labeled respectively by i and j: $i, j = 1$ for a time argument on the forward branch, $i, j = 2$ on the backward branch. The diagonal elements of $\hat{G}$ are related to the real-time Green's functions by the relations

$$\mathcal{G}^{T}(t,t') = \mathcal{G}^{<}(t,t') + \mathcal{G}^{R}(t,t') \tag{3.11}$$

$$\mathcal{G}^{\tilde{T}}(t,t') = \mathcal{G}^{<}(t,t') - [\mathcal{G}^{R}(t',t)]^{\dagger}, \tag{3.12}$$

and $\mathcal{G}^{>}_{ij}(t,t') = -i\langle c_i(t)c_j^{\dagger}(t')\rangle$ is the Greater Green's function. The perturbation theory is then constructed by splitting the Hamiltonian in a simple (solvable) part $\hat{\mathbf{H}}^0$, and a perturbation part studied order by order $\hat{\mathbf{H}}^{'}(t)$. The formal matrix representation of this decomposition reads,

$$\mathbf{H}(t) = \mathbf{H}^0 + \mathbf{H}^{'}(t) \tag{3.13}$$

$$\mathbf{H}^0 = \mathbf{H}^0_{\bar{0}\bar{0}} + \sum_{\bar{m}=1}^{\bar{M}} \mathbf{H}^0_{\bar{m}\bar{m}} \tag{3.14}$$

$$\mathbf{H}^{'}(t) = \mathbf{H}^{'}_{\bar{0}\bar{0}}(t) + \sum_{\bar{m}=1}^{\bar{M}} \left[\mathbf{H}^{'}_{\bar{m}\bar{0}}(t) + \mathbf{H}^{'}_{\bar{0}\bar{m}}(t)\right] \tag{3.15}$$

using the same notations for the subscripts as introduced in the previous section. In order to obtain a perturbative expansion of the Green's function matrix it appears convenient to work in the interaction picture with respect to $\hat{\mathbf{H}}^0$ as it is the solvable part of the Hamiltonian. In the case where $\mathbf{H}^{'}(t)$ is quadratic in the fields, the re-summation of the Green's function matrix expansion yields the Dyson equation [60, 61],

$$\hat{G}(t,t') = \hat{g}(t,t') + \int du\, \hat{g}(t,u)\mathbf{H}^{'}(u)\sigma_z\hat{G}(u,t'), \tag{3.16}$$

where σ_z is the Pauli matrix. $\hat{g}$ is the Green's function matrix of the uncoupled (isolated) system described by $\mathbf{H}^0$. Equation (3.16) is key for a numerical treatment of the formalism as it allows for the integration of subparts of the initial infinite open system.

Introducing the projections of Green's functions on the central region $G^R(t,t') = \mathcal{G}^R_{\bar{0}\bar{0}}(t,t')$ and $G^<(t,t') = \mathcal{G}^<_{\bar{0}\bar{0}}(t,t')$, one can obtain from Eq. (3.16) effective Dyson equations where the leads' degrees of freedom have been integrated out. The Dyson equation for G^R is derived from the diagonal part of Eq. (3.16) (see Appendix A) and reads

$$G^R(t,t') = g^R(t,t') + \int\int du\, dv\, g^R(t,u)\left[\mathbf{H}^{'}_{\bar{0}\bar{0}}(u)\delta(u-v) + \Sigma^R(u,v)\right]G^R(v,t'), \tag{3.17}$$

where self-energies encapsulate the effect of the leads,

$$\Sigma^R(t,t') = \sum_{\bar{m}=1}^{\bar{M}} \Sigma^R_{\bar{m}}(t,t'), \tag{3.18}$$

with

$$\Sigma^R_{\bar m}(t,t') = \mathbf{H}'_{\bar 0\bar m}(t) g^R_{\bar m}(t,t') \mathbf{H}'_{\bar m\bar 0}(t'). \tag{3.19}$$

Applying the operator $[i\partial_t - \mathbf{H}_{\bar 0\bar 0}(t)]$ on the left of Eq. (3.17) yields the equation of motion for the Retarded Green's function,

$$\boxed{i\partial_t G^R(t,t') = \mathbf{H}'_{\bar 0\bar 0}(t) G^R(t,t') + \int du\ \Sigma^R(t,u) G^R(u,t')} \tag{3.20}$$

or its symmetric counterpart

$$i\partial_{t'} G^R(t,t') = -G^R(t,t')\mathbf{H}'_{\bar 0\bar 0}(t') - \int du\ G^R(t,u)\Sigma^R(u,t') \tag{3.21}$$

with the initial condition $\lim_{\tau\to 0} G^R(t+\tau,t) = -i$. Similarly, the equation of motion for the Lesser Green's function can be integrated formally from the off-diagonal part of Eq. (3.16) (see Appendix A) and reads,

$$\boxed{G^<(t,t') = \int du\ dv\ G^R(t,u)\Sigma^<(u,v)[G^R(t',v)]^\dagger} \tag{3.22}$$

with $\Sigma^<(t,t') = \sum_{\bar m} \Sigma^<_{\bar m}(t,t')$ and $\Sigma^<_{\bar m}(t,t') = \mathbf{H}'_{\bar 0\bar m}(t) g^<_{\bar m}(t,t') \mathbf{H}'_{\bar m\bar 0}(t')$. Equations (3.20) and (3.22) form the starting point of the formalism detailed in this chapter.

3.3.2 *Equations of motion for the leads self-energies*

To get a complete set of equations, we need to relate the self-energies of the leads to the lead Hamiltonian matrices. While the corresponding calculation in the energy domain is well developed, self-energies as a function of time have been seldom calculated. Here we use the following equation of motion,

$$i\partial_t g^R_{\bar m}(t,t') - H_{\bar m}(t) g^R_{\bar m}(t,t') = \int du\ V_{\bar m}(t) g^R_{\bar m}(t,u) V^\dagger_{\bar m}(u) g^R_{\bar m}(u,t'). \tag{3.23}$$

This equation only provides the *surface* Green's function of the lead, i.e. Green's function matrix elements for the last layer of the semi-infinite periodic structure. For time-independent leads (the case studied in this thesis after the gauge transformation), $g^R_{\bar m}(t-t')$ is a function of the time difference $t-t'$ only. It is related by a simple Fourier transform to the surface Green's function in energy,

$$g^R_{\bar m}(t-t') = \int \frac{dE}{2\pi} e^{-iE(t-t')} g^R_{\bar m}(E). \tag{3.24}$$

There are many techniques to calculate $g^R_{\bar m}(E)$ but, the presence of a cusp at $t=t'$ in the time domain and $1/\sqrt{E}$ singularities in the energy domain (whenever a new conducting channel opens) renders a Fourier transform impractical and a direct use of Eq. (3.23) much more convenient. The analogue of Eq. (3.23) in the energy domain is a self-consistent equation for $g^R_{\bar{m}}(E)$,

$$g^R_{\bar{m}}(E) = 1/[E - H_{\bar{m}} - V_{\bar{m}} g^R_{\bar{m}}(E) V^\dagger_{\bar{m}}], \tag{3.25}$$

which is far less interesting than its time-dependent counterpart. Indeed, the corresponding iterative solution converges poorly (each iteration corresponds to adding one layer to the lead while other schemes allow to double its size at each iteration) and it requires the use of a small imaginary part in the self-energy. As each lead is at thermal equilibrium, the Lesser surface Green's function for the lead is obtained from the Retarded one through the use of the fluctuation-dissipation theorem [94, 61],

$$g^<_{\bar{m}}(E) = -f_{\bar{m}}(E) \left(g^R_{\bar{m}}(E) - [g^R_{\bar{m}}(E)]^\dagger \right) \tag{3.26}$$

where $f_{\bar{m}}(E) = 1/[1 + e^{(E-\mu_{\bar{m}})/k_B T_{\bar{m}}}]$ is the Fermi function of the lead.

3.4 WAVE-FUNCTION (WF) APPROACH

We now turn to the construction of our wave function approach. We seek to explicitly construct the wave function in terms of Green's functions, relate the physical observables to the wave function and derive the equations that this wave function satisfies. Eventually, we arrive at a closed set of equations where the original Green's function formalism has disappeared entirely. The central object of the resulting theory lies halfway between NEGF and the time-dependent scattering approach. Both Green's functions and the (time-dependent) scattering matrix can be obtained directly from the wave function.

In what follows we suppose that the voltage drop actually takes place *inside* the central region $\bar{0}$. This can be done without loss of generality; if it is not the case then we simply change our definition of the central region to include a few layers of the leads. We always include at least the first layer of each lead in our definition of the central region $\bar{0}$. This step is not necessary but somewhat simplifies the resulting expressions.

3.4.1 *Construction of the wave function*

We start with a representation of the lead Lesser self-energy in the energy domain,

$$\Sigma^<(t - t') = \sum_{\bar{m}} \int \frac{dE}{2\pi} i f_{\bar{m}}(E) e^{-iE(t-t')} \Gamma_{\bar{m}}(E) \tag{3.27}$$

where $\Gamma_{\bar{m}}(E) = i\mathbf{H}_{\bar{0}\bar{m}}\left(g^R_{\bar{m}}(E) - [g^R_{\bar{m}}(E)]^\dagger\right)\mathbf{H}_{\bar{m}\bar{0}}$ is the coupling matrix to the electrodes (also known as the tunneling rate matrix in the context of weak coupling). $\Gamma_{\bar{m}}(E)$ can be diagonalized into

$$\Gamma_{\bar{m}}(E) = \sum_\alpha v_{\bar{m}\alpha}\xi_{\alpha E}\xi^\dagger_{\alpha E} \tag{3.28}$$

where the $\xi_{\alpha E}$ are the so-called dual transverse wave functions and $v_\alpha(E)$ is the corresponding mode velocity [95]. Note that the $\xi_{\alpha E}$ are normalized but not necessarily orthogonal. They are related to the transverse incoming modes $\xi^{in}_{\alpha E}$ to be introduced in the next section by $\xi_{\alpha E} = \Gamma_{\bar{m}}\xi^{in}_{\alpha E}/v_{\bar{m}\alpha}$. Note that alternatively we could have used the fact that $\Gamma_{\bar{m}}$ is a Hermitian matrix to justify its diagonalization into a set of *orthonormal* vectors. However, by doing so we would have mixed outgoing and incoming states and lost the connection with the scattering theory described in the next section. We also note that all modes are in principle included but the evanescent ones have vanishing velocities and will therefore automatically drop out of the problem.

Eq. (3.22) for the Lesser Green's function, hence the observables, can be recast using the two above equations into,

$$\boxed{G^<(t,t') = \sum_\alpha \int \frac{dE}{2\pi}\, i f_\alpha(E)\Psi_{\alpha E}(t)\Psi_{\alpha E}(t')^\dagger} \tag{3.29}$$

where we have used a unique index α to denote both the leads and the channels inside the leads and introduced the wave function,

$$\Psi_{\alpha E}(t) = \sqrt{v_\alpha}\int du\; G^R(t,u)e^{-iEu}\xi_{\alpha E}. \tag{3.30}$$

$\Psi_{\alpha E}(t)$ is the projection inside the device region of $\psi_{\alpha E}(t)$ which is defined in the infinite system, $\Psi_{\alpha E} = [\psi_{\alpha E}]_{\bar{0}}$, with

$$\psi_{\alpha E}(t) = \sqrt{v_\alpha}\int du\; \mathcal{G}^R(t,u)e^{-iEu}\xi_{\alpha E}. \tag{3.31}$$

$\Psi_{\alpha E}(t)$ and $\psi_{\alpha E}(t)$ are the basic objects that will be discussed from now on. We note the Retarded Green's function, $G^R(t,t') = \theta(t-t')[G^>(t,t') - G^<(t,t')]$, can also be obtained from the wave function,

$$\boxed{G^R(t,t') = -i\theta(t-t')\int \frac{dE}{2\pi}\sum_\alpha \Psi_{\alpha,E}(t)\Psi^\dagger_{\alpha,E}(t')} \tag{3.32}$$

from which we get the normalization condition,

$$\boxed{\forall\, t\; \int \frac{dE}{2\pi}\sum_\alpha \Psi_{\alpha,E}(t)\Psi^\dagger_{\alpha,E}(t) = \mathbb{1}_{\bar{0}}.} \tag{3.33}$$

3.4.2 *Effective Schrödinger equation*

The equations satisfied by the wave function derive directly from the equation of motion for the Retarded Green's function. They read,

$$i\partial_t \Psi_{\alpha E}(t) = \mathbf{H}_{\bar{0}\bar{0}}(t)\Psi_{\alpha E}(t) + \int du\, \Sigma^R(t-u)\Psi_{\alpha E}(u) + \sqrt{v_\alpha} e^{-iEt}\xi_{\alpha E}, \tag{3.34}$$

and

$$i\partial_t \psi_{\alpha E}(t) = \mathbf{H}(t)\psi_{\alpha E}(t) + \sqrt{v_\alpha} e^{-iEt}\xi_{\alpha E}. \tag{3.35}$$

Remarkably, Eq. (3.35) is almost the Schrödinger equation, up to the source term $\sqrt{v_\alpha} e^{-iEt}\xi_{\alpha E}$. Together, Eqs. (3.29) and (3.34) (or alternatively Eq. (3.35)) form a closed set of equations that permits the calculation of the observables of the system. In particular, the Retarded Green's function does not appear explicitly anymore. Note that the initial conditions for the wave functions are not well defined. We shall find, however, that they are essentially irrelevant and that after some relaxation time they are forgotten; the source term controls the results (see Fig. 5.5). To understand the origin of this term we consider a one-dimensional chain with just one electrode and no time-dependent perturbations. The Schrödinger equation for the 1D chain in the energy domain reads,

$$\Psi_{x-1} + \Psi_{x+1} = E\Psi_x. \tag{3.36}$$

We suppose that the "system" corresponds to $x \geq 1$ and the "electrode" corresponds to $x \leq 0$. As a boundary condition in the electrode, we impose the incoming part of the wave, for $x \leq 0$,

$$\Psi_x = e^{ikx} + re^{-ikx} \tag{3.37}$$

which in turn implies that $E = 2\cos k$. Now we look for an effective equation where r has disappeared, which amounts to finding the effective boundary condition imposed on the system due to the presence of the electrode. Writing the Schrödinger equation for $x = 0$ and $x = 1$ we get,

$$1 + r + \Psi_2 = E\Psi_1 \tag{3.38}$$

$$e^{-ik} + re^{ik} + \Psi_1 = E(1+r) \tag{3.39}$$

Using $E = e^{ik} + e^{-ik}$ we find,

$$[\Sigma^R \Psi_1 + i\Sigma^R v] + \Psi_2 = E\Psi_1, \tag{3.40}$$

where we have introduced the self-energy $\Sigma^R = e^{ik}$ and the velocity $v = \partial E/\partial k$. Eq. (3.40) is reminiscent of the original equation $\Psi_0 + \Psi_2 = E\Psi_1$. The value of the wave function in the electrode, Ψ_0, has been replaced by an effective boundary condition (first two terms in Eq. (3.40)) and the electrode effectively drop out of the problem. This effective boundary condition contains a self-energy term (proportional to Ψ_1) and a source term. This is a generic consequence of our boundary conditions where we impose the incoming waves, as opposed to more conventional Dirichlet or Neumann boundary conditions. Upon transforming into the time domain, the self-energy term transforms into a convolution which gives rise to the memory kernel present in Eq. (3.34).

At this stage, several routes could be followed. If we suppose the time-dependent perturbations to be periodic, we can make use of the Floquet theorem to obtain a Floquet based wave function approach. Here, however, we concentrate on the physics of pulses (perturbations of any sort but localized in time). We suppose that the system is in a stationary state up to a time $t = 0$ and that the time-dependent perturbations (voltage pulses, microwaves, etc.) are switched on at time $t > 0$. We separate the problem into a stationary part and a time-dependent perturbation $\mathbf{H}_{\bar{0}\bar{0}}(t) = \mathbf{H}_{\bar{0}st} + \mathbf{H}_{\bar{0}w}(t)$. The solution of the stationary problem takes the form $e^{-iEt}\Psi^{st}_{\alpha E}$, where the stationary solution can be obtained by solving the linear (sparse) equation,

$$[E - \mathbf{H}_{\bar{0}st} - \Sigma^R(E)]\Psi^{st}_{\alpha E} = \sqrt{v_\alpha}\xi_{\alpha E}. \tag{3.41}$$

$\Psi^{st}_{\alpha E}$ is a typical output of wave function based algorithms for DC transport [96]. We now introduce a wave function measuring the *deviation* with respect to the stationary solution,

$$\Psi_{\alpha E}(t) = \bar{\Psi}_{\alpha E}(t) + e^{-iEt}\Psi^{st}_{\alpha E}. \tag{3.42}$$

$\bar{\Psi}_{\alpha E}(t)$ satisfies,

$$i\partial_t \bar{\Psi}_{\alpha E}(t) = \mathbf{H}_{\bar{0}\bar{0}}(t)\bar{\Psi}_{\alpha E}(t) + \int_0^t du\, \Sigma^R(t-u)\bar{\Psi}_{\alpha E}(u) + \mathbf{H}_{\bar{0}w}(t)e^{-iEt}\Psi^{st}_{\alpha E} \tag{3.43}$$

with the initial condition $\bar{\Psi}_{\alpha E}(t = 0) = 0$. Eq. (3.43) is very similar to Eq. (3.34) but it has the advantage that the equilibrium physics has been removed so that the memory kernel starts at $t = 0$ (instead of $t = -\infty$). Also, the source term does not take place at the system-leads interface anymore, but rather at the sites where a time-dependent perturbation is applied. A similar treatment can be done for $\psi_{\alpha E}(t)$ and we obtain

$$i\partial_t \bar{\psi}_{\alpha E}(t) = \mathbf{H}(t)\bar{\psi}_{\alpha E}(t) + \mathbf{H}_w(t)e^{-iEt}\psi^{st}_{\alpha E}, \tag{3.44}$$

where $\psi^{st}_{\alpha E}$ satisfies $[E - \mathbf{H}_{st}]\psi^{st}_{\alpha E} = \sqrt{v_\alpha}\xi_{\alpha E}$ and $\mathbf{H}(t) = \mathbf{H}_{st} + \mathbf{H}_w(t)$. We shall find that Eq. (3.43) or Eq. (3.44) are much more well suited for numerical simulations than the original NEGF equations.

Finally, a common case of interest involves metallic electrodes coupled to mesoscopic systems whose characteristic energy scales are much smaller than the Fermi energy of the electrodes. In this limit (known as the wide band limit), one can neglect the energy dependence of the electrode self-energy $\Sigma^R(E + \epsilon) \approx \Sigma^R(E)$ and the self-energy memory kernel becomes local in time resulting in

$$\boxed{i\partial_t \bar{\Psi}_{\alpha E}(t) = [\mathbf{H}_{\bar{0}\bar{0}}(t) + \Sigma^R(E)]\bar{\Psi}_{\alpha E}(t) + \mathbf{H}_{\bar{0}w}(t)e^{-iEt}\Psi^{st}_{\alpha E}.} \tag{3.45}$$

So far our starting point has been the NEGF formalism from which we have constructed the wave function $\Psi_{\alpha E}(t)$. We now turn to a "Landauer-Büttiker" scattering approach of time-dependent quantum transport in a mixed time-energy representation. We construct the time-dependent scattering states of the system and find that their projection inside the central region is in fact the wave function $\Psi_{\alpha E}(t)$. Hence, we shall establish (as it is the case for DC transport) that the corresponding scattering approach is rigorously equivalent to the NEGF formalism. Last, we shall make the connection with the partition free approach thereby completing the formalism part of this thesis.

3.5.1 *Conducting modes in the leads*

We start by introducing the plane waves α inside a lead $\bar{p}$ which take the form $\xi^{in}_{\bar{p}\alpha}(E)e^{-iEt-ik^{in}_{\alpha}(E)x}$ for the incoming states and $\xi^{out}_{\bar{p}\alpha}(E)e^{-iEt+ik^{out}_{\alpha}(E)x}$ for the outgoing ones. The integer x labels the different layers of the lead ($x \in \{1, 2, 3 \cdots\}$) counted from the central system. The normalized vectors $\xi^{out}_{\bar{p}\beta}$ ($\xi^{in}_{\bar{p}\beta}$) are the transverse part of the mode for the outgoing (incoming) states, including the evanescent modes (although those will eventually drop out for the incoming part). As the plane waves satisfy the Schrödinger equation, we obtain

$$[H_{\bar{p}} - E + V_{\bar{p}}\lambda_{\alpha} + V^{\dagger}_{\bar{p}}\lambda^{-1}_{\alpha}]\xi^{out}_{\bar{p}\alpha}(E) = 0, \tag{3.46}$$

with $\lambda_{\alpha} = e^{+ik^{out}_{\alpha}(E)}$. $\xi^{in}_{\bar{p}\alpha}(E)$ obeys the same equation with negative momenta. This (2$^{\text{nd}}$ order) equation can be recast in the form of a generalized eigenvalue problem,

$$\begin{pmatrix} H_{\bar{p}} - E & V^{\dagger}_{\bar{p}} \\ 1 & 0 \end{pmatrix} \begin{pmatrix} \xi_{\bar{p}\alpha}(E) \\ \chi_{\bar{p}\alpha}(E) \end{pmatrix} = \lambda_{\alpha} \begin{pmatrix} -V_{\bar{p}} & 0 \\ 0 & 1 \end{pmatrix} \begin{pmatrix} \xi_{\bar{p}\alpha}(E) \\ \chi_{\bar{p}\alpha}(E) \end{pmatrix} \tag{3.47}$$

for which efficient techniques have now been developed [95, 97] ($\chi_{\bar{p}\alpha}(E)$ is defined by the second line of Eq. (3.47)). We note that solving Eq. (3.46) can be non trivial when V is not invertible, a common case when the lattice has more than one atom per unit cell (e.g. graphene). The corresponding mode velocity is given by $v^{out}_{\bar{p}\alpha} = i(\xi^{out}_{\bar{p}\alpha})^{\dagger}[Ve^{+ik^{out}_{\alpha}(E)} - V^{\dagger}e^{-ik^{out}_{\alpha}(E)}]\xi^{out}_{\bar{p}\alpha}$. An interesting relation is obtained by observing that $\xi^{out}_{\bar{p}\alpha}(E)$ ($\xi^{in}_{\bar{p}\alpha}(E)$) are the eigenvectors of the Retarded (Advanced) Green's function of the lead,

$$g^{R}_{\bar{p}}(E)V^{\dagger}_{\bar{p}}\xi^{out}_{\bar{p}\alpha}(E) = e^{+ik^{out}_{\alpha}(E)}\xi^{out}_{\bar{p}\alpha}(E) \tag{3.48}$$

$$[g^{R}_{\bar{p}}(E)]^{\dagger}V^{\dagger}_{\bar{p}}\xi^{in}_{\bar{p}\alpha}(E) = e^{-ik^{in}_{\alpha}(E)}\xi^{in}_{\bar{p}\alpha}(E) \tag{3.49}$$

as can be shown using Eq. (3.25) and Eq. (3.46), see [95]. Eq. (3.46) implies that for any two modes (incoming or outgoing) [95],

$$(\lambda_{\alpha} - [\lambda^{*}_{\beta}]^{-1})\xi^{in/out}_{\bar{p}\beta}(E)[V_{\bar{p}}\lambda_{\alpha} - V^{\dagger}_{\bar{p}}\lambda^{*}_{\beta}]\xi^{in/out}_{\bar{p}\alpha}(E) = 0. \tag{3.50}$$

It follows that, while in general different modes are not orthogonal, they satisfy

$$[\xi^{out}_{\bar{p}\alpha}(E)]^\dagger \Gamma_{\bar{p}} \xi^{out}_{\bar{m}\beta}(E) = \delta_{\alpha\beta}\delta_{\bar{m}\bar{p}} v^{out}_{\bar{p}\alpha} \tag{3.51}$$

with a similar expression for the incoming modes.

3.5.2 *Construction of the scattering states*

Our aim is to construct a wave function $\psi^{scat}_{\alpha E}(t)$ which (i) is a solution of the Schrödinger equation and (ii) corresponds to an incoming plane wave in mode α (belonging to lead $\bar{m}$) with energy E. This boundary condition amounts to imposing the incoming part of the wave function, and leaving the outgoing part free. In particular, the system being time-dependent, the outgoing part can contain many different energies. In the rest of this section, we often drop the indices E and α when there is no risk of confusion. The value of $\psi^{scat}_{\alpha E}(t)$ is noted $\psi^{scat}_{0}(t)$ in the central region and $\psi^{scat}_{\bar{p}x}(t)$ in the x^{th} layer of lead $\bar{p}$. In the leads, the wave function is formed by a superposition of plane waves,

$$\psi^{scat}_{\bar{p}x}(t) \equiv \psi^{in}_{\bar{p}x}(t) + \psi^{out}_{\bar{p}x}(t) \tag{3.52}$$

with

$$\psi^{in}_{\bar{p}x}(t) = \delta_{\bar{p}\bar{m}} \frac{\xi^{in}_{\bar{p}\alpha}(E)}{\sqrt{|v^{in}_{\bar{m}\alpha}|}} e^{-iEt - ik^{in}_{\alpha}(E)x} \tag{3.53}$$

$$\psi^{out}_{\bar{p}x}(t) = \int \frac{dE'}{2\pi} \sum_{\beta} \frac{\xi^{out}_{\bar{p}\beta}(E')}{\sqrt{|v^{out}_{\bar{p}\beta}|}} e^{-iE't + ik^{out}_{\beta}(E')x} S_{\bar{p}\beta,\bar{m}\alpha}(E', E) \tag{3.54}$$

$S_{\bar{p}\beta,\bar{m}\alpha}(E', E)$ is the central object of the scattering theory, namely the probability amplitude for a mode α with energy E to be transmitted ($\bar{p} \neq \bar{m}$) or reflected ($\bar{p} = \bar{m}$) into mode β with energy E'. The formalism only differs from its time-independent counterpart by the possibility to absorb or emit energy. The normalization has been chosen so that the waves carry a current (per energy unit) unity. As Eq. (3.52) is made of a superposition of the eigenstates of the leads, it satisfies the time-dependent Schrödinger equation in the lead by construction. Eq. (3.52) forms an "incoming" boundary condition. One proceeds by writing the Schrödinger equation in the central region and in the first layer of the leads (the "matching conditions"):

$$\begin{aligned} i\partial_t \psi^{scat}_{0}(t) &= \mathbf{H}_{\bar{0}\bar{0}} \psi^{scat}_{0}(t) + \sum_{\bar{p}} V_{\bar{p}} \psi^{scat}_{\bar{p}1}(t) && (3.55) \\ i\partial_t \psi^{scat}_{\bar{p}1} &= H_{\bar{p}} \psi^{scat}_{\bar{p}1}(t) + V^\dagger_{\bar{p}} P_{\bar{p}} \psi^{scat}_{0}(t) + V_{\bar{p}} \psi^{scat}_{\bar{p}2}(t), && (3.56) \end{aligned}$$

where the projector $P_{\bar{p}}$ projects the wave function of the central region on the sites which are attached to the reservoir $\bar{p}$. The set of the five above equations fully defines the scattering states as well as the scattering matrix $S_{\bar{p}\beta,\bar{m}\alpha}$ of the system.

3.5.3 *Connection to the wave function approach*

To proceed, we note that as $\psi^{scat}_{\bar{p}x}(t)$ satisfies,

$$i\partial_t \psi^{scat}_{\bar{p}1} = H_{\bar{p}} \psi^{scat}_{\bar{p}1}(t) + V^{\dagger}_{\bar{p}} \psi^{scat}_{\bar{p}0}(t) + V_{\bar{p}} \psi^{scat}_{\bar{p}2}(t), \tag{3.57}$$

and Eq. (3.56) results in,

$$V^{\dagger}_{\bar{p}} P_{\bar{p}} \psi^{scat}_{\bar{0}}(t) = V^{\dagger}_{\bar{p}} \psi^{scat}_{\bar{p}0}(t) \tag{3.58}$$

which relates the scattering matrix on the right (via $\psi^{scat}_{\bar{p}0}(t)$) to the wave function inside the system on the left. We now use the fact that $\xi^{out}_{\bar{p}\alpha}(E)$ and $\xi^{in}_{\bar{p}\alpha}(E)$ are the eigenvectors of the Retarded and Advanced surface Green's function of lead $\bar{p}$. Equations (3.48), (3.49) and (3.52) provide,

$$V_{\bar{p}} \psi^{out}_{\bar{p}1}(t) = \int du \Sigma^{R}_{\bar{p}}(t-u) \psi^{out}_{\bar{p}0}(u). \tag{3.59}$$

Finally, inserting the explicit decomposition Eq. (3.52) in terms of incoming and outgoing waves inside Eq. (3.55) and using Eq. (3.58) and Eq. (3.59), we obtain,

$$i\partial_t \psi^{scat}_{\bar{0}}(t) = \mathbf{H}_{\bar{0}\bar{0}} \psi^{scat}_{\bar{0}}(t) + \sum_{\bar{p}} \int_{-\infty}^{t} du \Sigma^{R}_{\bar{p}}(t-u) P_{\bar{p}} \psi^{scat}_{\bar{0}}(u) + i\Gamma_{\bar{m}}(E) \psi^{in}_{\bar{m}0}(t). \tag{3.60}$$

Eq. (3.60) is identical to our main wave equation Eq. (3.34) which completes the proof that

$$\boxed{\psi^{scat}_{\bar{0}}(t) = \Psi_{\alpha E}(t).} \tag{3.61}$$

Hence the equivalence between the scattering approach and the NEGF formalism can be extended to time-dependent transport. We note however that $\psi_{\alpha E}(t)$ and the scattering state $\psi^{scat}_{\alpha E}(t)$ do not match outside of the scattering region as the former only contains outgoing modes (and no incoming ones).

3.5.4 *Generalization of the Fisher-Lee Formula*

Besides proving the formal equivalence between the Scattering and NEGF approaches in this context, the above construction provides an explicit link between the wave function and the scattering matrix. Indeed, using the definition Eq. (3.52) of the scattering matrix, one obtains after integration over time,

$$S_{\bar{p}\beta,\bar{m}\alpha}(E', E) = \int dt'\, e^{iE't'} \frac{[\xi^{out}_{\bar{p}\beta}(E')]^{\dagger}}{\sqrt{|v^{out}_{\bar{m}\alpha}(E')|}} \Gamma_{\bar{p}}(E') [\psi^{scat}_{\bar{p}0,\alpha E}(t') - \psi^{in}_{\bar{p}0,\alpha E}(t')]. \tag{3.62}$$

Eq. (3.62) is a generalization of the Fisher-Lee relation [98] for time-dependent problems. As the numerical algorithms described in the later sections allow one to compute the wave function $\psi^{scat}_{\bar{p}0,\alpha E}(t')$ directly, they also provide means to evaluate the scattering matrix through the above relation. Equation (3.62) can be further simplified into,

$$S_{\bar{p}\beta,\bar{m}\alpha}(E',E) = \frac{[\xi^{out}_{\bar{p}\beta}(E')]^{\dagger}}{\sqrt{|v^{out}_{\bar{m}\alpha}(E')|}}\Gamma_{\bar{p}}(E')\left[\int dt'\ e^{iE't'}\psi^{scat}_{\bar{p}0,\alpha E}(t') - \frac{\xi^{in}_{\bar{m}\alpha}(E')}{\sqrt{|v^{in}_{\bar{m}\alpha}(E)|}}2\pi\delta(E'-E)\right] \tag{3.63}$$

Inserting the definition of the wave function in terms of the Retarded Green's function inside Eq. (3.63), one obtains another form, closer to the original one of [98],

$$S_{\bar{p}\beta,\bar{m}\alpha}(E',E) = \frac{[\xi^{out}_{\bar{p}\beta}(E')]^{\dagger}}{\sqrt{|v^{out}_{\bar{m}\alpha}(E')|}}\Gamma_{\bar{p}}(E')\left[\mathcal{G}^{R}(E',E)\Gamma_{\bar{m}}(E) - 2\pi\delta(E'-E)\delta_{\bar{m}\bar{p}}\right]\frac{\xi^{in}_{\bar{m}\alpha}(E)}{\sqrt{|v^{in}_{\bar{m}\alpha}(E)|}} \tag{3.64}$$

where we have introduced the (double) Fourier transform of the Retarded Green's function,

$$\mathcal{G}^{R}(E',E) = \int dtdt'\ \mathcal{G}^{R}(t',t)e^{iE't'-iEt}. \tag{3.65}$$

3.5.5 *Link with the partition-free initial condition approach*

In the construction of the scattering states given above, we impose a boundary condition where the form of the incoming modes is fixed for all times while the outgoing modes are free. Hence, this construction treats incoming modes and outgoing ones on different footings. This might seem correct based on physical arguments, yet we have seen in section 3.4.1 that the matrix Γ could be diagonalized in several different ways. In the rest of this section, we follow a very simple route taken by Cini [62] and further developed in Refs. [63, 90, 91, 99] where such a distinction does not appear explicitly. The approach is conceptually very simple. Let us suppose that the Hamiltonian is time-independent up to $t = 0$, then for $t < 0$ we assume that the system is in an incoherent superposition of all the eigenstates $e^{-iEt}\psi^{st}_{\alpha E}$ of the system with a filling factor $f_\alpha(E)$ (this may be thermal equilibrium as in [90] or more generally a non-equilibrium stationary state). At time $t > 0$ the corresponding states $\psi^{init}_{\alpha E}(t)$ simply evolve according to the Schrödinger equation $i\partial_t\psi^{init}_{\alpha E}(t) = \mathbf{H}(t)\psi^{init}_{\alpha E}(t)$ with the initial condition $\psi^{init}_{\alpha E}(t=0) = \psi^{st}_{\alpha E}$. Apparently, this is a different boundary condition from the one of the scattering state above. We now use the block structure of the Schrödinger equation (projected on lead $\bar{p}$) and obtain after integration between 0 and t (momentarily dropping the indices E and α),

$$\psi_{\bar{p}}^{init}(t) + i g_{\bar{p}}^{R}(t)\psi_{\bar{p}}^{init}(0) = \int_0^t du\, g_{\bar{p}}^{R}(t-u)\mathbf{H}_{\bar{p}\bar{0}}\psi_{\bar{0}}^{init}(u) \tag{3.66}$$

from which we get (after substitution inside the equation for $\psi_{\bar{0}}^{init}$),

$$i\partial_t \psi_{\bar{0}}^{init}(t) = \mathbf{H}_{\bar{0}\bar{0}}(t)\psi_{\bar{0}}^{init}(t) + \int_0^t du \Sigma^R(t-u)\psi_{\bar{0}}^{init}(u) - i\sum_{\bar{p}} \mathbf{H}_{\bar{0}\bar{p}} g_{\bar{p}}^{R}(t)\psi_{\bar{p}}^{init}(0). \tag{3.67}$$

Eq. (3.67) is essentially Eq. (4) of [63]. Eq. (3.67) is very similar to Eq. (3.43) with a crucial practical difference: in the latter, the source term is present only at the system's sites which are time-dependent while in the former it takes place at the system-lead interfaces. Introducing $\bar{\psi}_{\alpha E}^{init}(t) \equiv \psi_{\alpha E}^{init}(t) - e^{-iEt}\psi_{\alpha E}^{st}$, we find that $\bar{\psi}_{\bar{0}}^{init}(t)$ obeys Eq. (3.43) with $\bar{\psi}_{\bar{0}}^{init}(t=0) = 0$. Hence, we have proved one more equivalence, between the wave function $\bar{\Psi}_{\alpha E}(t)$ and $\bar{\psi}_{\bar{0}}^{init}(t)$,

$$\boxed{\psi_{\alpha E\bar{0}}^{init}(t) = \Psi_{\alpha E}(t).} \tag{3.68}$$

We note that the equivalence requires that the initial states at $t = 0$ are the scattering states $\psi_{\alpha E}^{st}$ of the stationary system. When the system contains more than one channel, one finds that any choice of the initial condition $\sum_\alpha U_{a\alpha}\psi_{\alpha E}^{st}$, where U is a unitary matrix, eventually gives the same total current and is therefore also equivalent to the NEGF theory. However, the matrix U must be unitary which fixes the normalization of the initial states; they must carry a current unity.

3.5.6 *"Floquet wave function" and link with the Floquet scattering theory*

Although this thesis focuses on time-resolved electronics (typically transient regimes or voltage pulses), the wave function formalism can also be used for perturbations periodic in time. We refer to [38] for an introduction and bibliography on the subject. Let us briefly consider the situation where $\mathbf{H}_{\bar{0}\bar{0}}(t+T) = \mathbf{H}_{\bar{0}\bar{0}}(t)$ and introduce its decomposition in terms of harmonics of $\omega = 2\pi/T$,

$$\mathbf{H}_{\bar{0}\bar{0}}(t) = \sum_{n=-\infty}^{\infty} H_n e^{-in\omega t}. \tag{3.69}$$

We also define the Fourier transform $\Psi_{\alpha E}(E')$ of $\Psi_{\alpha E}(t)$,

$$\Psi_{\alpha E}(E') = \int dt'\, e^{iE't'}\Psi_{\alpha E}(t') \tag{3.70}$$

from which we can express Eq. (3.34) as,

$$E'\Psi_{\alpha E}(E') = \sum_n H_n \Psi_{\alpha E}(E'-n\omega) + \Sigma^R(E')\Psi_{\alpha E}(E') + 2\pi\delta(E'-E)\sqrt{v_\alpha}\xi_{\alpha E}.$$

(3.71)

Introducing $\epsilon \in [-\omega/2, \omega/2]$ and m such that $E' = E + \epsilon + m\omega$, one defines $\Psi_m(\epsilon) \equiv \Psi_{\alpha E}(E + \epsilon + m\omega)$ which verifies,

$$\begin{aligned}\epsilon \Psi_m(\epsilon) = \sum_n H_n \Psi_{m-n}(\epsilon) + [\Sigma^R(E + \epsilon + m\omega) - m\omega - E]\Psi_m(\epsilon) \\ + 2\pi\delta(\epsilon)\delta_{m,0}\sqrt{v_\alpha}\xi_{\alpha E}.\end{aligned} \tag{3.72}$$

Last, we define

$$\psi_{\alpha E\epsilon}(t) = \sum_m e^{-im\omega t}\Psi_m(\epsilon) \tag{3.73}$$

and obtain,

$$\Psi_{\alpha E}(t) = \int_{-\omega/2}^{\omega/2} \frac{d\epsilon}{2\pi} e^{-iEt - i\epsilon t}\psi_{\alpha E\epsilon}(t). \tag{3.74}$$

$\psi_{\alpha E\epsilon}(t)$ verifies $\psi_{\alpha E\epsilon}(t + T) = \psi_{\alpha E\epsilon}(t)$ so that Eq. (3.74) corresponds in fact to the Floquet theorem. We also note that the source term in Eq. (3.72) is only present at $\epsilon = 0$ so that the other energies do not contribute to the scattering wave function. Taking this last point into account and computing (as an example) the current $I_{ij}(t)$ between site i and site j, we arrive at,

$$I_{ij}(t) = -2\,\mathrm{Im} \sum_\alpha \int \frac{dE}{2\pi} f_\alpha(E) \sum_{n,m,p} \Psi^*_{\alpha E,m}(i)[H_n]_{ij}\Psi_{\alpha E,p}(j)e^{-i(n-m+p)\omega t}, \tag{3.75}$$

where the wave function $\Psi_{\alpha E,n}(i)$ at site i satisfies,

$$[E + m\omega - \Sigma^R(E + m\omega)]\Psi_{\alpha E,m} - \sum_n H_n \Psi_{\alpha E,m-n} = \delta_{m,0}\sqrt{v_\alpha}\xi_{\alpha E}. \tag{3.76}$$

Eq. (3.75) and Eq. (3.76) provide a complete set of equations to compute the current of the system. The corresponding "Floquet wave function" can be put in direct relation to Floquet Scattering theory using the link with the Scattering matrix established at the beginning of this section. In practice, the infinite set of equations defined by Eq. (3.76) needs to be truncated somehow [100] and one is left with solving a large, yet finite, system of linear equations. Alternatively, a systematic perturbation theory can be constructed taking the AC Hamiltonian as a small perturbation [39].

We have thus made explicit connections between various theoretical frameworks: the NEGF, the scattering approach, the partition-free initial condition approach and, for perturbations that are periodic in time, the scattering Floquet approach. This concludes the formalism part of this thesis. We now turn to its application to voltage pulses.

4

LANDAUER FORMULA FOR VOLTAGE PULSES

So far, the formalism that has been presented is applicable to arbitrary time-dependent perturbations. We now proceed with the particular case where the perturbation is a voltage pulse of finite duration applied to one or several Ohmic contacts of a device. We introduce the number of injected particles as a relevant quantity for time-dependent transport in section 4.1, and proceed with the calculation of the scattering matrix of a voltage pulse in section 4.2. Finally we derive a generalization of the Landauer formula for the number of injected particles in section 4.3. All the results presented in this chapter are original.

4.1 TOTAL NUMBER OF INJECTED PARTICLES

We aim to define the generalization of the Landauer formula for pulse physics. A natural extension would be to compute the time-dependent current $I_{\bar{p}}(t)$ in lead $\bar{p}$. It is given by,

$$I_{\bar{p}}(t) = \int \frac{dE}{2\pi} \sum_{\alpha} f_{\alpha}(E) I_{\alpha E,\bar{p}}(t), \tag{4.1}$$

with

$$I_{\alpha E,\bar{p}}(t) = 2\ Im\ \Psi^{\dagger}_{\alpha E,\bar{p}x}(t) V^{\dagger}_{\bar{p}} \Psi_{\alpha E,\bar{p}x-1}(t). \tag{4.2}$$

The notation corresponds to the one introduced in the previous section. We can now insert Eq. (3.52) into the definition of $I_{\bar{p}}(t)$ and express it in terms of the scattering matrix. The general formula involves a triple integral over energy which is not very illuminating. It also lacks the basic properties of the Landauer-Büttiker approach which arise from current conservation (time-dependent current is not conserved) and gauge invariance. An important simplification occurs when one calculates the total number of particles, $n_{\bar{p}} = \int_0^{t_M} dt I_{\bar{p}}(t)$, received in lead p in the limit $t_M \to \infty$. Of course, at this level of generality, $n_{\bar{p}}$ can possibly diverge due to the presence of DC currents. Hence, the following expressions assume a finite (large) value of the cutoff t_M. Introducing $n_{\alpha E,\bar{p}} = \int_0^{t_M} dt\ I_{\alpha E,\bar{p}}(t)$ we obtain,

$$n_{\alpha E,\bar{p}} = \sum_{\beta \in \bar{p}} \int \frac{dE'}{2\pi} P_{\bar{p}\beta,\bar{m}\alpha}(E', E) - \int_0^{t_M} dt\ \delta_{\alpha\beta}\delta_{\bar{p}\bar{m}}, \tag{4.3}$$

with

$$\lim_{t_M \to \infty} P_{\bar{p}\beta,\bar{m}\alpha}(E', E) = |S_{\bar{p}\beta,\bar{m}\alpha}(E', E)|^2. \tag{4.4}$$

$P_{\bar{p}\beta,\bar{m}\alpha}(E',E)$ is thus interpreted as the probability density to be scattered from channel α and energy E to channel β and energy E'. Equivalently, introducing the Fourier transform $S_{\bar{p}\beta,\bar{m}\alpha}(t,E) = \int \frac{dE'}{2\pi} e^{-iE't} S_{\bar{p}\beta,\bar{m}\alpha}(E',E)$ and using Parseval theorem, one obtains,

$$n_{\alpha E,\bar{p}} = \sum_{\beta\in\bar{p}} \int_0^{t_M} dt\ [P_{\bar{p}\beta,\bar{m}\alpha}(t,E) - \delta_{\alpha\beta}], \tag{4.5}$$

with

$$\lim_{t_M\to\infty} P_{\bar{p}\beta,\bar{m}\alpha}(t,E) = |S_{\bar{p}\beta,\bar{m}\alpha}(t,E)|^2. \tag{4.6}$$

As the wave function $\Psi_{\alpha E}$ obeys the Schrödinger equation, one gets a current conservation equation $\partial_t Q_{\alpha E,\bar{0}} = \sum_{\bar{p}} I_{\alpha E,\bar{p}}(t)$ where $Q_{\alpha E,\bar{0}} = \Psi_{\alpha E}(t)^\dagger \Psi_{\alpha E}(t)$ is the total number of particles inside the system associated with mode α and energy E. Long after the pulse, the system is back to equilibrium so that $Q_{\alpha E,\bar{0}}(t_M) = Q_{\alpha E,\bar{0}}(0)$ and the current conservation implies,

$$\forall E\ ,\forall\alpha \sum_{\bar{p}} n_{\alpha E,\bar{p}} = 0. \tag{4.7}$$

Putting everything together, we obtain,

$$n_{\bar{p}} = \sum_{\bar{m}} \sum_{\alpha\in\bar{m}} \int \frac{dE}{2\pi} f_{\bar{m}}(E) n_{\alpha E,\bar{p}}. \tag{4.8}$$

To summarize, we find a formal analogy between the known rules of conventional (DC) scattering theory and those of time-dependent transport. Summations over channels are extended to a summation over channels *and* an integral over energy (or time) while the current is replaced by the total number of transmitted particles. In practice, the different terms contributing to $n_{\bar{p}}$ should be grouped in such a way that the limit $t_M \to \infty$ can be taken without divergences (in the absence of DC current).

4.2 SCATTERING MATRIX OF A VOLTAGE PULSE

The theory above is rather general. We proceed with the particular case where the perturbation is a voltage pulse applied to one electrode. We consider an abrupt voltage drop across an infinite wire described by the Hamiltonian matrix Eq. (3.3). The voltage drop takes place between layers $x = 0$ and $x = 1$. For this system, the Scattering matrix has a block structure in terms of the amplitudes of reflection r and transmission d,

$$S_{\beta\alpha}(E',E) = \begin{pmatrix} r_{\beta\alpha}(E',E) & d_{\beta\alpha}(E',E) \\ d'_{\beta\alpha}(E',E) & r'_{\beta\alpha}(E',E) \end{pmatrix} \tag{4.9}$$

which corresponds to the following form of the scattering wave function,

$$x > 0 :\ \psi_x^{scatt}(t) = \psi_x^d(t),\quad x \leq 0 :\ \psi_x^{scatt}(t) = \psi_x^r(t) \tag{4.10}$$

with

$$\psi^r_x(t) = \frac{\xi^+_{\bar{m}\alpha}(E)}{\sqrt{|v^+_{\bar{m}\alpha}|}} e^{-iEt+ik^+_\alpha(E)x} + \sum_\beta \int \frac{dE'}{2\pi} \frac{\xi^-_{\bar{m}\beta}(E')}{\sqrt{|v^-_{\bar{m}\beta}|}} e^{-iE't-ik^-_\beta(E')x} r_{\beta\alpha}(E',E) \tag{4.11}$$

$$\psi^d_x(t) = \sum_\beta \int \frac{dE'}{2\pi} \frac{\xi^+_{\bar{m}\beta}(E')}{\sqrt{|v^+_{\bar{m}\beta}|}} e^{-iE't+ik^+_\beta(E')x} d_{\beta\alpha}(E',E) \tag{4.12}$$

where the subscript $+$ ($-$) refers to right (left) going modes. $\psi^r_x(t)$ and $\psi^d_x(t)$ satisfy $i\partial_t \psi_x(t) = H_{\bar{m}}\psi_x(t) + V^\dagger_{\bar{m}}\psi_{x-1}(t) + V_{\bar{m}}\psi_{x+1}(t)$ for all values of x while $\psi^{scatt}_x(t)$ satisfies the "matching conditions",

$$i\partial_t \psi^{scatt}_0(t) = H_{\bar{m}}\psi^{scatt}_0(t) + V^\dagger_{\bar{m}}\psi^{scatt}_{-1}(t) + V_{\bar{m}} e^{i\phi_{\bar{m}}(t)}\psi^{scatt}_1(t) \tag{4.13}$$

$$i\partial_t \psi^{scatt}_1(t) = H_{\bar{m}}\psi^{scatt}_1(t) + V^\dagger_{\bar{m}} e^{-i\phi_{\bar{m}}(t)}\psi^{scatt}_0(t) + V_{\bar{m}}\psi^{scatt}_2(t) \tag{4.14}$$

from which we directly get

$$V_{\bar{m}}\psi^r_1(t) = V_{\bar{m}} e^{i\phi_{\bar{m}}(t)}\psi^d_1(t) \tag{4.15}$$

$$V^\dagger_{\bar{m}}\psi^r_0(t) = V^\dagger_{\bar{m}} e^{i\phi_{\bar{m}}(t)}\psi^d_0(t) \tag{4.16}$$

Inserting the explicit forms of $\psi^r_x(t)$ and $\psi^d_x(t)$ into Eq. (4.15) and Eq. (4.16) (and making use of Eq. (3.48) and Eq. (3.49)), we obtain the equation satisfied by the transmission matrix,

$$\begin{aligned}\sum_\beta \int \frac{dE'}{2\pi} K_{\bar{m}}(\epsilon - E') \left[\Sigma^R_{\bar{m}}(E') - \Sigma^R_{\bar{m}}(\epsilon)^\dagger\right] \frac{\xi^+_{\bar{m}\beta}(E')}{\sqrt{|v^+_{\bar{m}\beta}(E')|}} d_{\beta\alpha}(E',E) = \\ \left[\Sigma^R_{\bar{m}}(E) - \Sigma^R_{\bar{m}}(\epsilon)^\dagger\right] \frac{\xi^+_{\bar{m}\alpha}(E)}{\sqrt{|v^+_{\bar{m}\alpha}(E)|}} 2\pi\delta(\epsilon - E)\end{aligned} \tag{4.17}$$

and similarly

$$\begin{aligned}\sum_\beta \int \frac{dE'}{2\pi} K^*_{\bar{m}}(E' - \epsilon) \left[\Sigma^R_{\bar{m}}(E') - \Sigma^R_{\bar{m}}(\epsilon)^\dagger\right] \frac{\xi^-_{\bar{m}\beta}(E')}{\sqrt{|v^-_{\bar{m}\beta}(E')|}} d'_{\beta\alpha}(E',E) = \\ \left[\Sigma^R_{\bar{m}}(E) - \Sigma^R_{\bar{m}}(\epsilon)^\dagger\right] \frac{\xi^-_{\bar{m}\alpha}(E)}{\sqrt{|v^-_{\bar{m}\alpha}(E)|}} 2\pi\delta(\epsilon - E)\end{aligned} \tag{4.18}$$

where $K_{\bar{m}}(E)$ is the harmonic content of the transmitted voltage pulse,

$$K_{\bar{m}}(E) = \int dt\; e^{i\phi_{\bar{m}}(t)+iEt}. \tag{4.19}$$

In the situation where time-reversal symmetry is present $\mathbf{H}_{\bar{m}\bar{m}} = \mathbf{H}^{*}_{\bar{m}\bar{m}}$ (no spin), one finds that to each right-going mode $\xi^{+}_{\bar{m}\alpha}$ is associated a left-going one $(\xi^{+}_{\bar{m}\alpha})^{*}$ with equal velocity. It follows that,

$$d'_{\beta\alpha}(E', E) = d_{\beta\alpha}(E, E')^{*}. \tag{4.20}$$

The relation between left and right propagating modes is however more complex in presence of magnetic field. We continue with a physical assumption, namely that the typical pulse height (w_p) is small compared to the Fermi energy $w_p \ll E_F$. We also suppose that its duration τ_p is rather long, $\hbar/\tau_p \ll E_F$. This is in fact the typical situation in actual experiments where the Fermi level $E_F \approx 1eV$ (metal) or $E_F \approx 10meV$ (semi-conductor heterostructure) is much larger than the typical characteristic energies of the pulses ($w_p < 1\mu eV$, $\tau_p \approx 1ns \rightarrow \hbar/\tau_p \approx 1\mu eV$). As the kernel $K_{\bar{m}}(E)$ typically decays over $\max(w_p, \hbar/\tau_p)$, we can therefore neglect the energy dependence of the modes in Eq. (4.17) (the so called wide band limit) which are all taken to be at energy E. The terms $\Sigma^{R}_{\bar{m}}(E') - \Sigma^{R}_{\bar{m}}(\epsilon)^{\dagger}$ simplify into $\Sigma^{R}_{\bar{m}}(E) - \Sigma^{R}_{\bar{m}}(E)^{\dagger} = -i\Gamma_{\bar{m}}(E)$ and Eq. (3.51) leads to,

$$\boxed{d_{\beta\alpha}(E', E) = \delta_{\alpha\beta} K^{*}_{\bar{m}}(E - E')} \tag{4.21}$$

or,

$$\boxed{d_{\beta\alpha}(t, E) = \delta_{\alpha\beta} e^{-i\phi_{\bar{m}}(t) - iEt},} \tag{4.22}$$

while $d'_{\beta\alpha}(E, E') = \delta_{\alpha\beta} K_{\bar{m}}(E' - E)$. We note that in the wide band limit Eq. (4.20) holds even in the presence of magnetic field. Also, the reflection matrix $r_{\beta\alpha}(E', E)$ simply vanishes in this limit. The role of the voltage drop is therefore purely to redistribute the energy of the incoming electron into a larger energy window.

4.3 VOLTAGE PULSES IN MULTITERMINAL SYSTEMS

We now have all the ingredients to construct the theory of voltage pulses in general multi-terminal systems. We assume that before the pulse, the system is at equilibrium with no DC current flowing. We also assume the wide band limit of the above section, which implies that all the inelastic processes of the scattering matrix take place at the position of the voltage drop. The assumption that no reflection takes place at this place is important as each electron experiences at most two inelastic events (upon entering and leaving the sample) which considerably simplifies the theory. Introducing the DC scattering matrix $S^{0}_{\bar{p}\beta,\bar{m}\alpha}(\epsilon)$ of the device *in the absence of pulses*, we have,

$$S_{\bar{p}\beta,\bar{m}\alpha}(E', E) = \int \frac{d\epsilon}{2\pi} K_{\bar{p}}(\epsilon - E')\, S^{0}_{\bar{p}\beta,\bar{m}\alpha}(\epsilon)\, K^{*}_{\bar{m}}(E - \epsilon). \tag{4.23}$$

Using $\int dE'/(2\pi) K_{\bar p}(\epsilon - E')K^*_{\bar p}(\bar\epsilon - E') = 2\pi\delta(\bar\epsilon - \epsilon)$, we find upon performing the integral over E' in Eq. (4.3),

$$n_{\bar p} = \sum_{\bar m}\sum_{\beta\in\bar p}\sum_{\alpha\in\bar m}\int\frac{d\epsilon}{2\pi}\left[\int\frac{dE}{2\pi}f(E)|S^0_{\bar p\beta,\bar m\alpha}(\epsilon)|^2\,|K_{\bar m}(E-\epsilon)|^2 - f(\epsilon)\int_0^{t_M}dt\;\delta_{\alpha\beta}\delta_{\bar p\bar m}\right] \tag{4.24}$$

By using the unitarity of the device Scattering matrix $\sum_{\bar m\beta}|S^0_{\bar p\beta,\bar m\alpha}(\epsilon)|^2 = \delta_{\alpha\beta}\delta_{\bar p\bar m}$ in the second part of Eq. (4.24), it can be rewritten in a more compact form where the limit $t_M \to \infty$ can be taken formally. It reads,

$$\boxed{\begin{aligned} n_{\bar p} &= \sum_{\bar m} N_{\bar p\bar m} \\ N_{\bar p\bar m} &= \sum_{\beta\in\bar p}\sum_{\alpha\in\bar m}\int\frac{d\epsilon}{2\pi}|S^0_{\bar p\beta,\bar m\alpha}(\epsilon)|^2\int\frac{dE}{2\pi}|K_{\bar m}(E-\epsilon)|^2\,[f(E)-f(\epsilon)]\,. \end{aligned}} \tag{4.25}$$

Eq. (4.25) is the main result of this section. The "pulse conductance matrix" $N_{\bar p\bar m}$ can be seen as the formal generalization of the multiterminal DC conductance matrix [101] to voltage pulses. In particular it shares two important properties of the DC conductance matrix: charge conservation and gauge invariance. Equations (4.24) and (4.25) call for a number of comments. In particular they consist of the difference of two large terms so that some care is needed when performing practical calculations.

— First, Eq. (4.24) contains a diverging term on the right hand side which corresponds to the injected current from lead $\bar m$. Indeed, at equilibrium, although the net total currents coming from the different leads cancel, each lead injects a finite current, leading to a diverging number of injected particles. Therefore, to use Eq. (4.24) in practice, it is important to first sum the contribution from all leads before performing the integrals. Also, one must add those contributions at fixed energy ϵ (i.e. the energy inside the device region, not E the original energy of the injected particle) for those diverging terms to properly compensate.

— Second, although Eq. (4.24) apparently contains contributions from the whole spectrum, one can show that the only non-compensating terms arise from a small region around the Fermi energy. Indeed, let us consider an energy ϵ well below E_F. The kernel $K_{\bar m}(E-\epsilon)$ vanishes when $E-\epsilon$ becomes larger than $\max(w_p, \hbar/\tau_p)$ so that the values of E effectively contributing to the integral are also well below E_F, hence $f(E) = f(\epsilon) = 1$. The integral over the energy E can now be performed and, using Parseval theorem, we get $\int dE|K_{\bar m}(E-\epsilon)|^2 = \int_0^{t_M} dt$. We can now sum over the channel index α and lead index $\bar m$ using the unitarity condition $\sum_{\alpha\bar m}|S^0_{\bar p\beta,\bar m\alpha}(\epsilon)|^2 = 1$ and finally find that the first term of Eq. (4.24) compensates the second one for each energy ϵ. Again, to obtain this compensation it is important to *first* perform the integral over the injected energy E at fixed energy ϵ. The same point applies to Eq. (4.25), E and ϵ must be close for $K_{\bar m}(E-\epsilon)$ to be non zero hence the term $f(E) - f(\epsilon)$ vanishes away from the Fermi level. More discussion on this aspect and its numerical (technical) implications can be found in section 5.4.

- Current conservation is one of the main features of the Landauer approach which is usually lost in non-interacting AC transport, as the electronic density varies in time inside the system [33]. However the total number of particles is a conserved quantity and

$$\sum_{\bar{p}} N_{\bar{p}\bar{m}} = 0 \tag{4.26}$$

as can be seen directly on Eqs. (4.24), (4.25) or from the general argument at the beginning of this section.

- Another equally important feature of the scattering approach is the gauge invariance — raising the potential of all the leads simultaneously does not create any current — which is also usually lost in the non-interacting AC theory. However Eq. (4.24) does satisfy gauge invariance. Indeed, suppose we send an identical voltage pulse on all the leads simultaneously. Then the term $|K_{\bar{m}}(E-\epsilon)|^2$ does not depend on $\bar{m}$ and one can immediately perform the sum over α and $\bar{m}$ and use $\sum_{\alpha\bar{m}} |S^0_{\bar{p}\beta,\bar{m}\alpha}(\epsilon)|^2 = 1$. In a second step we perform the integral over E of the first term of Eq. (4.24) using Parseval theorem and find again that it exactly matches and compensates the second term and $n_{\bar{p}} = 0$. Note that while the above statement is non trivial, there is a weaker form of gauge invariance which is always verified. The physics is entirely unaffected by a global change of the potentials of all the leads *and* the internal potential of the device (as such a global variation of the potential can be absorbed by a simple global phase in the wave function). The combination of both forms of gauge invariance (weak and strong) implies that a uniform voltage pulse applied to the central region $\bar{0}$ (through a capacitive coupling to a gate) does not create any charge pumping, even in the non adiabatic limit.

- One of the appealing aspects of Eq. (4.25) is that it has a direct connection to the DC conductance matrix in the adiabatic limit. Indeed the DC Landauer formula reads,

$$I_{\bar{p}} = \frac{e^2}{h} \sum_{\bar{m}} T_{\bar{p}\bar{m}} V_{\bar{m}}, \tag{4.27}$$

where $T_{\bar{p}\bar{m}}$ is the total transmission probability from lead $\bar{m}$ to $\bar{p}$. When the voltage pulse is extremely slow (adiabatic limit) with respect to all the characteristic times of the device, one expects the current to follow the voltage adiabatically, $I_{\bar{p}}(t) = (e^2/h) \sum_{\bar{m}} T_{\bar{p}\bar{m}} V_{\bar{m}}(t)$ and

$$n_{\bar{p}} = \sum_{\bar{m}} T_{\bar{p}\bar{m}} \bar{n}_{\bar{m}}, \tag{4.28}$$

where $\bar{n}_{\bar{m}} = \int dte V_{\bar{m}}(t)/h$ is the total number of particles injected by the voltage pulse in lead $\bar{m}$. Hence, in the adiabatic limit, $N_{\bar{p}\bar{m}} =$

$T_{\bar{p}\bar{m}}\bar{n}_{\bar{m}}$ has a nice interpretation in terms of the total transmission probability from $\bar{m}$ to $\bar{p}$ and the interesting question is how the physics deviates from this limit when the pulses get faster than the internal characteristic time scales of the device. This point will be addressed in chapter 7.

5

STRATEGIES FOR NUMERICAL SIMULATIONS

We now turn to a discussion of various algorithms for simulating the formalism introduced in chapter 3. Here we provide a concrete example of an application to a simple one-dimensional chain, but the algorithms are general and apply to arbitrary dimensions and geometries as it will appear in the coming chapters. Our Hamiltonian reads,

$$\hat{\mathbf{H}}(t) = -\gamma \sum_{i=-\infty}^{+\infty} c^\dagger_{i+1} c_i - \gamma [e^{i\phi(t)} - 1] c^\dagger_2 c_1 + \sum_{i=1}^{N} \epsilon_i c^\dagger_i c_i + h.c. \tag{5.1}$$

where we inject a voltage pulse $w(t)$ with $\phi(t) = \int_{-\infty}^{t} du\, w(u)$ through the system, ϵ_i is the potential inside the central region $\bar{0} = \{1, 2, \ldots N\}$ and γ is the hopping between first neighbor sites. The ϵ_i can in principle be time-dependent but we restrict the examples to static cases; all the time dependence comes from the voltage drop between site 1 and site 2. During the development of the numerical techniques presented below, we used various analytical results to perform consistency checks of the validity of the numerics. They are summarized in Appendix B.

We denote N the total number of sites of the central region and S the number of sites connected to the electrodes (for a cubic system in d dimensions we have $N \sim L^d$ and $S \sim L^{d-1}$). Let us call $t_{\max}$ the maximum time of the simulations and h_t the typical discretization time step. In this chapter, we introduce various algorithms in the first two sections, and turn to the numerics in the third one. We emphasize that, although these algorithms have very different computing efficiencies, they are all mathematically equivalent and—as we have checked explicitly—give the same numerical results. The brute force implementations are known material, while the rest is an original work.

5.1 NON-EQUILIBRIUM GREEN'S FUNCTIONS APPROACH

We begin with three algorithms which implement the NEGF approach labeled GF-A, B and C. Our starting point is the set of equations of motion given by Eq. (3.20) and Eq. (3.22):

$$i\partial_t G^R(t,t') = \mathbf{H}_{\bar{0}\bar{0}}(t) G^R(t,t') + \int du\, \Sigma^R(t,u) G^R(u,t')$$

$$G^<(t,t') = \int du \int dv\, G^R(t,u) \Sigma^<(u,v) [G^R(t',v)]^\dagger$$

5.1.1 *GF-A: brute-force integration of the NEGF equations*

The first technique consists in directly integrating the equations of motion of the NEGF formalism treating the integro-differential equations as ordinary differential equations. However, the right hand sides of the equations contain the self-energy integrals that need to be re-evaluated every time step. This also means that some values of the Retarded Green's function in the past must be kept in memory. The algorithm consists of 3 steps. One starts with a calculation of the leads' self-energy by a direct integration of Eq. (3.23) for the $S \times S$ surface Green's function of the leads. In the second step, one proceeds and integrates Eq. (3.20) which has a rather similar structure. The last step is the calculation of the Lesser Green's function using the double integration of Eq. (3.22). This last step is quite problematic as the integration over times takes place over an infinite time window (as opposed to the calculation of the Retarded Green's function where the self-energy terms only span a finite window due to the causality of the Retarded Green's function). In practice, one has to resort to using a cutoff within a large time window Δ_t. We can already note that the CPU cost of all these three steps scale as the square of the total time, either $(t_{\max}/h_t)^2$ or $(\Delta_t/h_t)^2$ and that the calculations of various observables (for different times for instance) involve separate calculations for the last step. For implementation purposes, we note that the integrals containing the self-energy terms can be parallelized by dividing the integral range into smaller pieces, which can be used to speed up the calculations. For integrating the equations of motion, we use either an implicit linear multi-step scheme [102] or an explicit 3rd order Adams-Bashforth scheme (with slightly better performances for the latter). Overall, the GF-A approach quickly becomes prohibitively expensive in CPU time. This may explain why (to the best of our knowledge) the simulations performed so far within this approach have been restricted to very small systems and times.

5.1.2 *GF-B: Integrating out the time-independent subparts of the device*

A first strategy to improve on the direct (naive) GF-A approach described above is to integrate out the parts of the device region where we do not want to compute observables. A typical example is shown in Fig. 5.1. Suppose that a subset Ω of the sites in region $\bar{0}$ has a "sub" Hamiltonian matrix $\mathbf{H}_\Omega(t)$. The Green's function for the isolated region Ω (i.e. when the coupling to the rest of region $\bar{0}$ is zero) can be obtained by simply integrating the equation of motion of the finite region, $i\partial_t g^R_\Omega(t,t') = \mathbf{H}_\Omega(t) g^R_\Omega(t,t')$. This is particularly simple when the region Ω is time-independent: diagonalizing the finite matrix $\mathbf{H}_\Omega \chi_\alpha = \epsilon_\alpha \chi_\alpha$, the Retarded Green's function simply reads,

$$g^R_\Omega(t-t') = -i\theta(t-t') \sum_\alpha e^{-i\epsilon_\alpha (t-t')} \chi_\alpha \chi_\alpha^\dagger. \tag{5.2}$$

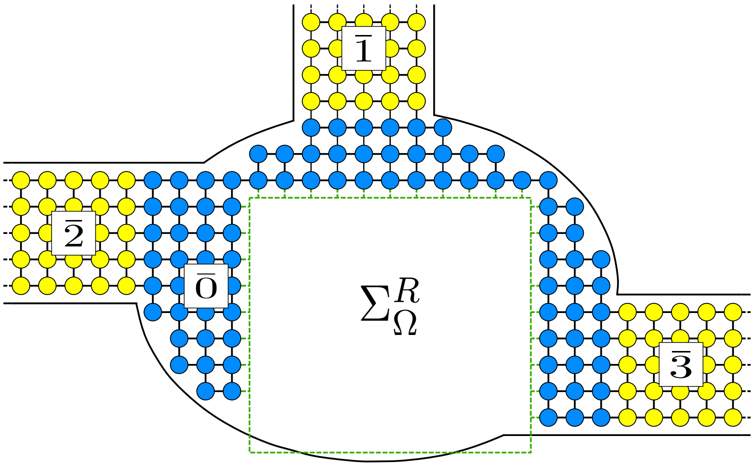

Figure 5.1 – Sketch of the GF-B scheme. The degrees of freedom of the region Ω inside the dashed green square are integrated out in a self-energy term denoted Σ^R_Ω. This integration leads to an effective system containing a reduced number of sites.

Note that Eq. (5.2) contrasts with its counterpart in the energy domain because the Retarded Green's function as a function of energy of a finite region is very ill defined numerically, as it is essentially a sum of Dirac distributions. Noting $\mathbf{H}_{\bar{0}\Omega}$ the matrix elements coupling the Ω region to the rest of the device region $\bar{0}$, we introduce the self-energy due to the Ω region,

$$\Sigma^R_\Omega(t,t') = \mathbf{H}_{\bar{0}\Omega}(t) g^R_\Omega(t,t') \mathbf{H}_{\Omega\bar{0}}(t'). \tag{5.3}$$

We can now proceed with solving Eq. (3.20) for the smaller region $\bar{0}\backslash\Omega$ with the added Σ^R_Ω in the self-energy,

$$\Sigma^R(t,t') \to \Sigma^R(t,t') + \Sigma^R_\Omega(t,t'). \tag{5.4}$$

Note however that the Lesser self-energy is unchanged as the Ω region is not a lead (i.e. is not at thermal equilibrium). Using this procedure, any region can be integrated out of the device region, effectively reducing the effective total size N of the simulation, but at the cost of increasing the number of surface sites S.

When the size of the Ω region becomes large, a direct calculation of $\Sigma^R_\Omega(t,t')$ becomes impractical. Fortunately, many schemes that have been developed in the energy domain can be transposed to the time domain: the original recursive Green's function algorithm, its variant the knitting algorithm [103] or the more involved nested dissection algorithm [104, 105]. These schemes can be discussed using the self-energy introduced above to "decimate" parts of the system, but they are perhaps more transparent when discussed in the context of the Dyson equation. Let $H_{ab}(t)$ be the Hamiltonian matrix of a system and let one decompose it into the sum of two terms $H_{ab} = H_a + H_b$ (typically H_a will be the Hamiltonian matrix for two disconnected regions and H_b connects these two regions together) and we note G^R_{ab} (G^R_a) the Retarded Green's function associated with H_{ab} (H_a). In this context, the Dyson equation reads,

$$G^R_{ab}(t,t') = G^R_a(t,t') + \int du\; G^R_a(t,u)H_b(u)G^R_{ab}(u,t'). \tag{5.5}$$

Eq. (5.5) allows the separated parts of the systems to be merged (note that the structure in time of this equation is "triangular", i.e. one can solve it for t close to t' and iteratively increase t). We refer to [103] for a detailed discussion of the procedure used for glueing isolated parts together. Applying Eq. (5.5) recursively in a (quasi) one-dimensional geometry, one can add one slice of the system at each iteration until the full system has been added (Recursive Green's function algorithm). Adding the sites one at a time, one obtains the knitting algorithm which allows one to handle systems of arbitrary geometries. Both algorithms have CPU times that scale as $S^2N(\Delta_t/h_t)^2$ but memory footprints much smaller than the direct method. In the last algorithm, nested dissection, one cuts the system recursively into 2 (or more) pieces until the pieces are small enough such that their individual Green's functions may be calculated directly. The gluing sequence is then applied backward to reconstruct the Retarded Green's function of the full system. Note that the nested dissection algorithm suffers from stability problems in the energy domain as some of the pieces are not in contact with the leads (and thus suffers from the problem discussed in the beginning of this subsection). In the time domain, however, no such limitation occurs.

5.1.3 *GF-C: integration scheme that preserves unitarity*

In GF-A and GF-B, we use simple discretization schemes to integrate the integro-differential equations for the Retarded Green's functions. However, these schemes (as well as others, such as the Runge-Kutta method) do not enforce unitarity of the evolution operator in Eq. (3.8). The scheme GF-C builds on GF-B but one replaces the discretization scheme by one that preserves this important property of quantum propagation.

Eq. (3.8) implies that for any intermediate time $u \in [t',t]$ we have,

$$\mathcal{G}^R(t,t') = i\mathcal{G}^R(t,u)\mathcal{G}^R(u,t'), \tag{5.6}$$

which has a simple interpretation in terms of path integral. The propagator between t' and t is a sum over all possible paths and this formula reflects the fact that we keep track of the site where the particle is at time u. The projection of Eq. (5.6) onto the central region $\bar{0}$ yields,

$$\forall\, u \in [t',t],\; \mathcal{G}^R_{\bar{0}\bar{0}}(t,t') = i\mathcal{G}^R_{\bar{0}\bar{0}}(t,u)\mathcal{G}^R_{\bar{0}\bar{0}}(u,t') + i\sum_{i=1}^{M}\mathcal{G}^R_{\bar{0}\bar{i}}(t,u)\mathcal{G}^R_{\bar{i}\bar{0}}(u,t'). \tag{5.7}$$

We use the Dyson equation to integrate over the degrees of freedom of the leads, therefore rewrite $\mathcal{G}^R_{\bar{0}\bar{i}}(t,u)$ and $\mathcal{G}^R_{\bar{i}\bar{0}}(u,t')$ as follows,

$$\mathcal{G}^R_{\bar{0}\bar{i}}(t,u) = \int_u^t dv\ \mathcal{G}^R_{\bar{0}\bar{0}}(t,v)\mathbf{H}_{\bar{0}\bar{i}}(v)g^R_{\bar{i}}(v,u) \tag{5.8}$$

$$\mathcal{G}^R_{\bar{i}\bar{0}}(u,t') = \int_{t'}^u dv\ g^R_{\bar{i}}(u,v)\mathbf{H}_{\bar{i}\bar{0}}(v)\mathcal{G}^R_{\bar{0}\bar{0}}(v,t') \tag{5.9}$$

After substituting these above relations into Eq.(5.7) we obtain,

$$\begin{aligned} \forall\ u\ \in [t',t],\ G^R(t,t') = iG^R(t,u)G^R(u,t') + \\ \sum_{i=1}^{M} \int_u^t dv\ G^R(t,v) \int_{t'}^u du\ \mathbf{H}_{\bar{0}\bar{i}}(v)g^R_{\bar{i}}(v,v')\mathbf{H}_{\bar{i}\bar{0}}(v')G^R(v',t'), \end{aligned} \tag{5.10}$$

where we recognize the Retarded self-energy which allows for a more condensed form,

$$G^R(t,t') = iG^R(t,u)G^R(u,t') + \int_u^t dv \int_{t'}^u dv'\ G^R(t,v)\Sigma^R(v,v')G^R(v',t'). \tag{5.11}$$

Eq. (5.11) is a sum of two terms which depend on the position of the particle at time u. The first term corresponds to a particle which is in the central region at time u while the second term accounts for the paths entering the leads at $v' < u$ and returning to the central region at a later time $v > u$ (i.e. the particle is in the lead at time u). Eq. (5.11) encapsulates the unitarity of the evolution operator by construction. It can be used to realize an efficient explicit integration scheme for the Retarded Green's function. Applying Eq. (5.11) with $t \to t + h_t$ and $u \to t$ we obtain,

$$\begin{aligned} G^R(t+h_t,t') = iA_{h_t}(t)G^R(t,t') \\ + \frac{h_t}{2}\int_{t'}^t dv[A_{h_t}(t)\Sigma^R(t,v) - i\Sigma^R(t+h_t,v)]G^R(v,t') \end{aligned} \tag{5.12}$$

where $A_{h_t}(t)$ is the short time propagator $A_{h_t}(t) = G^R(t+h_t,t)$. Eq. (5.12) provides an explicit scheme for integrating the equation of motion which proves to be more stable than the naive ones. Note that the Hamiltonian matrix has disappeared from Eq. (5.12). It is hidden in the short time propagator, $A_{h_t}(t)$, which can be obtained "exactly" from a direct integration of the equation of motion Eq. (3.20) using a very small time step (much smaller than h_t). The computing time to get this very precise estimate is $\propto h_t^2$ and, h_t being small, therefore negligible.

5.2 NUMERICAL IMPLEMENTATION OF THE WAVE FUNCTION APPROACH

We now turn to four numerical implementations of the wave function approach labeled WF-A, B, C and D. We shall see that they are much simpler and efficient than their NEGF counterparts. Our starting point is Eq. (3.34):

$$i\partial_t \Psi_{\alpha E}(t) = \mathbf{H}_{\bar{0}\bar{0}}(t)\Psi_{\alpha E}(t) + \int du\, \Sigma^R(t-u)\Psi_{\alpha E}(u) + \sqrt{v_\alpha} e^{-iEt}\xi_{\alpha E}$$

5.2.1 *WF-A: direct integration of Eq. (3.34)*

In the first algorithm, denoted WF-A, we integrate directly Eq. (3.34) using a 3rd order Adams-Bashforth scheme. The algorithm is intrinsically parallel as the calculations for different energies are totally independent. In a second step, we calculate the energy integral of Eq. (3.29) to obtain the various observables. Note that this calculation can be done on fly so that observables for all intermediate values of $t \leq t_{\text{max}}$ can be obtained in a single run (in contrast to the GFs algorithms). A second level of parallelism can be introduced with the calculation of the self-energy terms. Note that in principle, the strategies developed for GF-B and GF-C could be also used for the wave function approach. We shall take a somewhat different route however. A direct advantage of the WF approaches is that the equations involved are on vectors rather than on matrices. Sophisticated optimizations could be used in order *not* to calculate all the matrix elements in the GF approaches (but only the relevant ones). However in the WF approach, one naturally calculates the minimum information needed to recover the observables.

5.2.2 *WF-B: subtracting the stationary solution*

WF-B is very similar to WF-A except that we now use Eq. (3.43) and therefore study the deviation from the stationary case. Being able to subtract the stationary physics from the equations brings three distinct advantages compared to WF-A. First, self-energy memory integrals start from $t = 0$ (instead of $t = -\infty$) removing the need for the large time cutoff Δ_t introduced earlier. In addition, the initial condition is very well defined as the wave function simply vanishes. Second, for most practical physical systems, the characteristic energies involved are small compared to the Fermi energy. Subtracting the stationary physics allows one to take advantage of this feature to narrow down the integration of Eq. (3.29) to a region close to the Fermi energy. Finally, the source terms in Eq. (3.43) are present only at the sites where time-dependent perturbations are present.

5.2.3 *WF-C: from integro-differential to differential equation*

The scheme WF-B is already quite efficient and renders rather large problems ($N \sim 1000$) for rather long times ($t \sim 1000\gamma^{-1}$) tractable in a reasonable CPU time (say, 1 hour). Let us analyze its total CPU cost. We find, $CPU(WF-B) \propto (t/h_t)[N + S^2(t/h_t)]N_E$ where the first term comes from the (sparse) matrix vector multiplication with the Hamiltonian matrix and the second term accounts for the memory integral with the self-energy. The factor N_E accounts for the different energies and modes for which Eq. (3.44) must be integrated. In general this N_E is not an issue as all these calculations can be done in parallel and for relevant regimes the integral gets concentrated on a region close to the Fermi energy. The memory footprint is $MEM(WF-B) \propto [N + S(t/h_t)]$ as we need to keep in memory the wave function at time t in the system plus its history on the lead-system interfaces. The bottleneck of the calculation clearly comes from the self-energy integral which itself comes from the information corresponding to the wave function outside of the central region. The computational time is essentially the same as if one had studied the time evolution of a finite isolated system of $N + S^2(t/h_t)$ sites. For the typical values used here, $t = 1000\gamma^{-1}$ and $h_t = 0.01$, we find that WF-B's CPU is the same as if one was studying a finite system (i.e. no leads) of size $N = 100000$. On the other hand we know that signal propagation in the Schrödinger equation takes place at most at a speed $v = \partial E/\partial k$ with $E(k) = -2\gamma \cos k$ for a 1D chain. Hence at most $M \approx \gamma t$ layers of the lead can be probed by the propagation of the wave function. For $t = 1000\gamma^{-1}$ this means at most 1000 layers.

The scheme WF-C is therefore very simple. Instead of integrating the integro-differential equation Eq. (3.43), one integrates the much simpler differential equation Eq. (3.44). As this cannot be done for an infinite system, one simply truncates the system keeping the central region plus M layers of each leads (see Fig. 5.2). The expected correct value for M is $M \approx v_{mx} t/2$ with the maximum speed being $v_{mx} = \gamma \max_k |\partial E/\partial k| = \gamma z$. z is the coordinance of the system (number of neighbors per site) and the factor $1/2$ comes from the fact that the signal has to travel up to the effective boundary (yellow-red interface on Fig. 5.2) and come back in order to disturb the central region. Lower values of M can be used if the Fermi energy is close to the band edges and the system is therefore slower. According to the above analysis, only $M \sim 1000 \ll 100000$ layers should be necessary, which should lead to an important speed up compared to WF-B. It also considerably simplifies the implementation and allows for very aggressive optimizations. The expected gain is not a simple prefactor as $CPU(WF-C) \propto (t/h_t)[N + S\gamma t]N_E$ is parametrically smaller than WB-B for 2D and 3D systems.

5.2.4 *WF-D: faster convergence using the wide band limit*

The drawback of WF-C is that hardwall boundary conditions are employed at the yellow-red interface (see Fig. 5.2). If one does not take a large enough value of M, the particles will eventually bounce back toward the central region. WF-D is a simple generalization of WF-C where the remaining part of the leads (yellow sites in Fig. 5.2) are treated within the wide band limit Eq. (3.45). We effectively have absorbing boundary conditions and faster convergence properties with respect to M. Note that WF-D is an

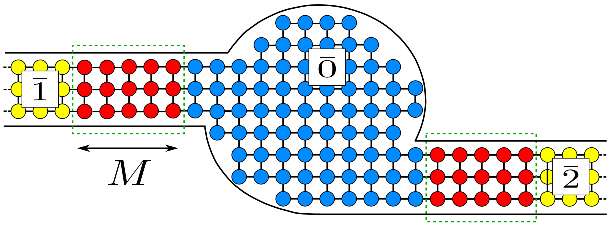

Figure 5.2 – Sketch of the WF-C and WF-D schemes: M layers of the leads (red) are added the central part $\bar{0}$ (blue circles) to constitute the effective central region. In WF-C the rest of the leads (yellow circles) are simply ignored while in WF-D, they are treated within the wide band approximation.

exact scheme, the (wide band limit) self-energy term is only used to accelerate the convergence with respect to M (as we shall see later in Fig. 5.6). We shall see that WF-D will be by far the fastest of all the methods described in this thesis. We gather below the various steps associated with its practical implementation (the equations that follow were given before and are repeated here for convenience).

1. One starts with defining the Hamiltonian of the model, i.e. the two matrices $H_{\bar{m}}$ and $V_{\bar{m}}$ that define the Hamiltonian of each lead as well as the time-independent matrix $\mathbf{H}_{\bar{0}st}$ for the central part and the time-dependent counterpart $\mathbf{H}_{\bar{0}w}(t)$. In many cases (for instance for the voltage pulses discussed next), the time-dependent part of the Hamiltonian only connects a few subparts of the central region.
2. a) One constructs the stationary modes of the leads, solving Eq. (3.47). (There is a large literature on this topic which we refer to, see [103] and references therein.)

   b) One also computes the self-energy of the leads, defined by $\Sigma^R(E) = \sum_{\bar{m}} V_{\bar{m}} g^R_{\bar{m}}(E) V^\dagger_{\bar{m}}$ and Eq. (3.25).
3. Once the leads properties are known, one computes the stationary wave function of the system solving the following linear set of equations,

$$[E - \mathbf{H}_{\bar{0}st} - \Sigma^R(E)]\Psi^{st}_{\alpha E} = \sqrt{v_\alpha}\,\xi_{\alpha E}.$$

   Note that steps (2a), (2b) and (3) are standard steps of quantum transport calculations in wave function based algorithms.
4. M layers of the leads are now concatenated to the central region Hamiltonian matrix $\mathbf{H}_{\bar{0}st}$. Everything is now ready to form the main Eq. (3.45) of the method,

$$i\partial_t \bar{\Psi}_{\alpha E}(t) = [\mathbf{H}_{\bar{0}st} + \mathbf{H}_{\bar{0}w}(t) + \Sigma^R(E)]\bar{\Psi}_{\alpha E}(t) + \mathbf{H}_{\bar{0}w}(t) e^{-iEt}\Psi^{st}_{\alpha E}$$

   which is integrated numerically using any standard integration scheme.
5. The full wave function of the system is then reconstructed,

$$\Psi_{\alpha E}(t) = \bar{\Psi}_{\alpha E}(t) + e^{-iEt}\Psi^{st}_{\alpha E}.$$

6. The various observables (time-dependent current, electronic density...), which can be expressed in terms of the Lesser Green's function, are obtained by the numerical integration (and sum over incoming modes) over energy of Eq. (3.29). For instance, the current between sites i and j reads,

$$I_{ij}(t) = -2\,\mathrm{Im} \sum_{\alpha} \int \frac{dE}{2\pi} f_{\alpha}(E) \Psi^{*}_{\alpha E}(i,t) \mathbf{H}_{ij}(t) \Psi_{\alpha E}(j,t). \tag{5.13}$$

It is worth noticing that after subtracting the equilibrium, only the outgoing modes remain present in the leads, and the out-of-equilibrium part of the wave function is zero except where the source term has propagated. This is a real change of paradigm. Instead of considering a perturbation coming from the leads and modifying the system, one computes the effect of a source term propagating in the system and the leads. As a result upon using perfectely absorbing boundary conditions, WF-D can scale linearly with the simulated time. The implementation of such boundary conditions is an ongoing effort in the lab.

5.3 NUMERICAL TESTS OF THE DIFFERENT APPROACHES

We illustrate the various implementations presented in the first two sections of this chapter with concrete numerical calculations and benchmarks. We shall then conclude on their relative computational performance.

5.3.1 *Green's function based algorithms*

Let us start the numerical applications by sending a square voltage pulse, $w(t) = w_0 \theta(t - t_0)\theta(t_1 - t)$, inside our quantum wire ($t_1 > t_0$). Fig. 5.3 shows the pulse (dashed line) together with the calculation of the current $I(t)$ using the GF-C technique (red line) and WF-B (black). Our first finding is that both methods agree, which, given the fact that the two methods are totally independent, is a strong check of the robustness of the approaches. After relaxation, we expect the current to saturate to its DC value given by the Landauer formula $I_{dc} = w_0$ (transmission is unity for a perfect 1D chain), and indeed, it does. Just after the abrupt rise of the potential, one observes rapid oscillations of frequency $2\gamma/\pi$. These oscillations, often observed in numerical simulations [71], come from the fact that the rise of the voltage is (infinitely) fast compared to the bandwidth of the system, hence the band serves as a low-pass filter for the signal. Other large energy oscillations of frequency $E_F/(2\pi)$ can also be observed. The bandwidth usually corresponds to optical frequencies. For nanoelectronics applications, therefore one should stay in a regime where the characteristic time scales of the time-dependent perturbations are large (say at least a factor 10) compared to γ^{-1}.

Before the pulse, the current is zero. In the WF-B scheme, this is automatically encoded as the system is in a stationary state. In the GF schemes

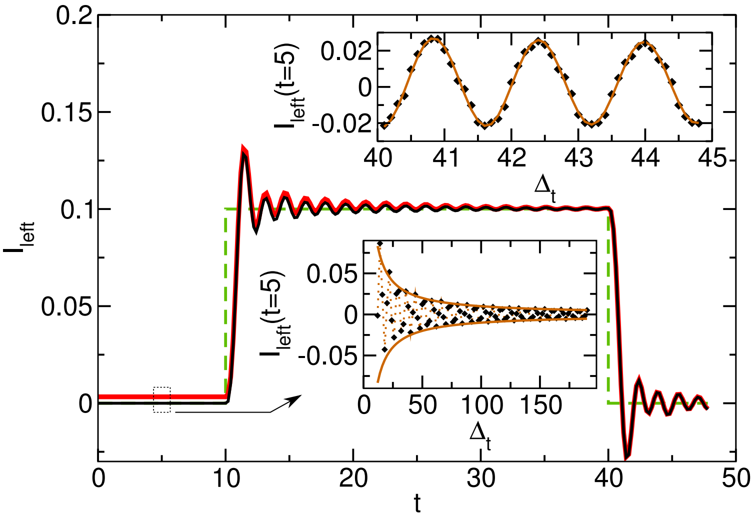

Figure 5.3 – Current as a function of time for a square voltage pulse $w(t) = w_0\theta(t - t_0)\theta(t_1 - t)$ with $w_0 = 0.1\gamma$, $t_0 = 10\gamma^{-1}$, $t_1 = 40\gamma^{-1}$ and $E_F = 0\gamma$. The lines show $w(t)$ (dashed), the GF-C result (red) and the WF-B result (black). Lower inset: current $I(t = 5\gamma^{-1})$ as a function of Δ_t for the GF-B scheme (symbols) together with the fit $1/\Delta_t$ (line). Upper inset: zoom of the lower inset with the fit $I = (0.1 + \cos(4\Delta_t))/\Delta_t$.

however, one needs a large value of the cut-off Δ_t to simply recover this elementary fact. The lower inset of Fig. 5.3 shows the current before the pulse as a function of the cut-off Δ_t together with a $1/\Delta_t$ fit. The data in the lower inset look noisy but upon closer inspection (upper inset), one finds that the convergence shows fast oscillations as $\cos(4\gamma\Delta_t)/\Delta_t$. The slow convergence of the GF schemes with respect to Δ_t is in itself a strong limitation.

As Fig. 5.3 considers a perfect lead, it is enough to keep a small ($N \geq 2$) number of sites in the central region. If one is interested in, say, the time it takes for a pulse to propagate, then a much larger system is necessary and GF-A becomes impractical. Fig. 5.4 shows a comparison between GF-B and GF-C for the calculation of the diagonal part of the Retarded Green's function for a system with $N = 100$ where the 96 central sites have been integrated out in order to reduce the effective size of the system. We find that the naive discretization scheme (linear multi-steps in this instance) used in GF-B fails and becomes unstable at large times while the unitarity preserving scheme of GF-C restores the stability of the algorithm. Further inspection showed that, indeed, extremely small values of h_t were needed in GF-B to enforce current conservation. GF-C is the best Green's function based algorithm we could come up with.

5.3.2 *Wave functions based algorithms*

We now turn to the wave function based algorithms. Fig. 5.5 shows the local density of particles on site 1 for a system of two sites, $N = 2$, using WF-A and various initial conditions. We find that the local density converges to

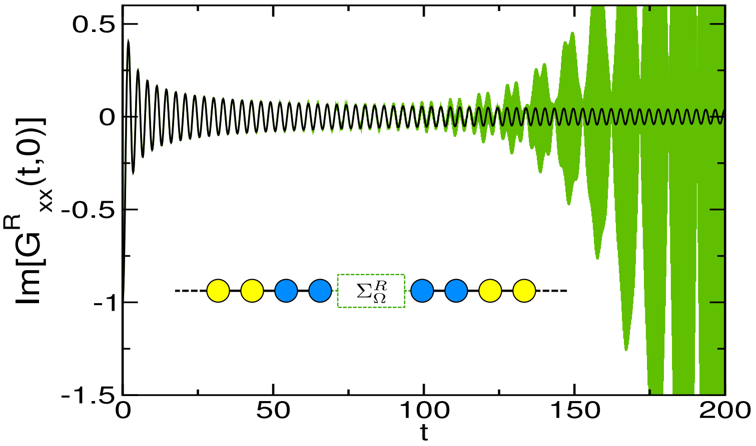

Figure 5.4 – Comparison of GF-B (green, divergent) and GF-C (black, stable). We plot the imaginary part of the diagonal part of the Retarded Green's function as a function of time for $N = 100$ (no time-dependent perturbation is applied). The 96 central sites have been integrated out and an effective system of four sites remains. $h_t = 0.1$.

its equilibrium value for any initial condition, and rather faster than within Green's function algorithms. More importantly, by calculating the DC scattering wave function (a standard object in computational DC transport), one can avoid the relaxation procedure (i. e. compute a quantity until one considers it has reached its equilibrium value) and automatically incorporate the equilibrium properties of the system (dashed line). WF-B which naturally captures the equilibrium conditions is a clear improvement over WF-A. According to the arguments developed above, WF-C and D should permit further improvements. Fig. 5.6(a) shows current versus time in presence of

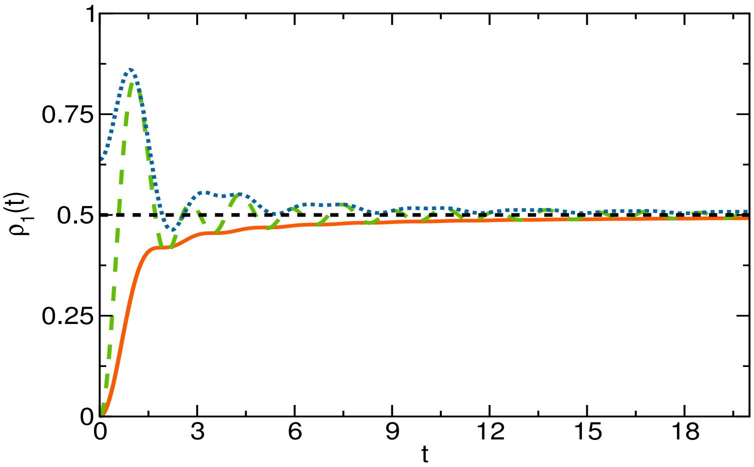

Figure 5.5 – Sensitivity of WF-A to initial conditions. Local density of particles on site 1 as a function of time within WF-A. The calculations are done for $\Psi_{E,x}(t = 0) = 0$ (orange full line), $\Psi_{E,x}(t = 0) = \delta_{x,1}$ (blue dotted line), $\Psi_{E,x}(t = 0) = \delta_{x,2}$ (long green dashed line) and $\Psi_{E,x}(t = 0) = \Psi^{st}_E$ (short black dashed line). Except in the last case, we ignore the memory integral for negative times.

a Gaussian pulse for the three methods WF-B, C and D (and various values of the number M of added sites for the latter two). In the case of WF-C, one observes a very accurate regime until a time $t_0 \propto M$ where the method abruptly becomes very inaccurate. This is due to the finiteness of the effective system in WF-C. t_0 corresponds to the time it takes for the signal to travel until the end of the sample and back again after being reflected at the end. The wide band limit approximation used in WF-D allows one to limit this abrupt failure and results in a much more robust (and slightly faster) method. Fig. 5.6b shows the (maximum) error made as a function of M. As surmised, very small values of M are needed for very accurate results. WF-D is the fastest and most robust method we developed.

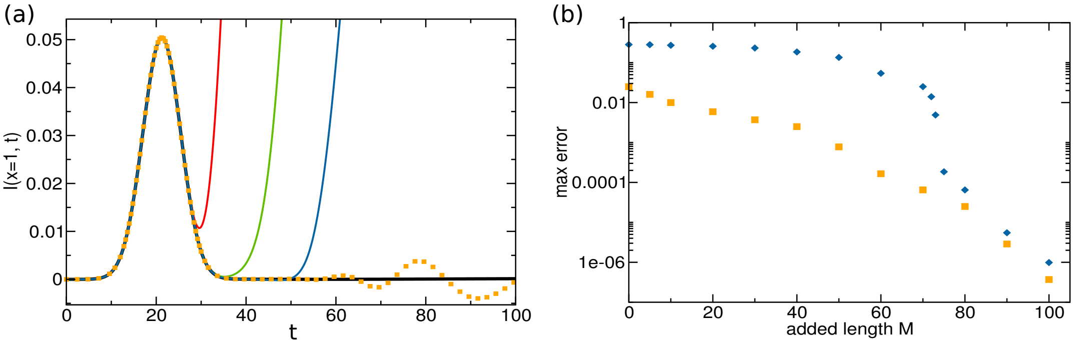

Figure 5.6 – Comparative study of WF-B, C and D for $N = 100$. $E_F = -1\gamma$ and we send a Gaussian voltage pulse $w(t) = V_p e^{-4\log(2)t^2/\tau_p^2}$ with $V_p = 0.05\gamma$ and $\tau_p = 10\gamma^{-1}$ through the system. (a) Current as a function of time just after the voltage drop for WF-B (black), WF-C with (from left to right) $M = 10$ (red), $M = 20$ (green), $M = 30$ (blue) and WF-D $M = 30$ (orange squares). (b) Maximum error between $t = 0\gamma^{-1}$ and $t = 100\gamma^{-1}$ as a function of M for WF-C (blue diamonds) and WF-D (orange squares).

5.3.3 *Relative performance of the different approaches*

We end this chapter with Table 5.1 that compares the relative performance of the various methods presented here. We find that WF-D is now fast enough to study two or three dimensional systems with tens of thousand of sites (work station) or millions of sites (supercomputers) with matching simulation times. More applications will be shown in the coming chapters and will show that WF-D essentially bridges the gap between our simulation capabilities for stationary problems and time-dependent ones.

Table 5.1 shows rather unambiguously the superiority of the WF-D approach over all the others, especially the GF approaches. GF-B (not stable for long times, otherwise similar to GF-C), WF-A (similar to WF-B but much less robust) and WF-C (similar to WF-D but less robust and slightly slower) are not shown. Note that the given times correspond to single core calculations. WF-D can be further accelerated using two levels of parallelism. A trivial one is the calculation of different energies on different cores (allowing to drop the factor N_E). The second one is the sparse matrix-dense vector multiplication in the evaluation of the product $\mathbf{H}_{\bar{0}\bar{0}}(t)\bar{\Psi}_{\alpha E}(t)$ in Eq. (3.45). There are also two avenues for optimization which were not yet explored in depth. The choice of the time integration scheme (e.g. an adaptive time step) and the choice of the scheme for the integration over energy (here again a combination of Gaussian quadrature scheme with an adaptive energy mesh might be more effective than a naive approach).

Algorithm	CPU (1D)	Estimated CPU (2D)	Scaling of CPU
WF-D	1	10^4	$(t/h_t)N_E[N+\gamma t S]$
WF-B	40	4.10^7	$(t/h_t)N_E[N+(t/h_t)S^2]$
GF-C	10^4	10^{12}	$(t/h_t)^2 S^3$ (*)
GF-A	10^5	10^{14}	$(t/h_t)^2 S^2 N$ (*)

Table 5.1 – Computation time in seconds for a calculation performed on a single computing core. 1D case: $N = 20$ and $t_{max} = 10\gamma^{-1}$ (for GF-A the calculation has been done in parallel using 48 cores in order to obtain the results within a few hours). 2D case: 100×100 sites hence, $S = 100$, $N = 10^4$ and $t_{max} = 100\gamma^{-1}$. The CPU time is estimated from the scaling laws except for WF-D where calculations of similar sizes could be performed. Third column: typical scaling of the computing time. A notable additional difference between the WF and GF methods is that the GF methods (*) only provide the observables at one given time per calculation while the WF methods give the full curve in one run. Typical values of N_E needed for the integrations over energy are $20 < N_E < 100$.

5.4 INTEGRAL OVER ENERGIES FOR THE WAVE FUNCTION APPROACH

We have seen in section 4 that only a small energy window around the Fermi level contributes to the transport properties and we would like now to understand how this fact manifests itself in the numerical calculations.

The central technical issue when performing the energy integral numerically is that within the WF method, one integrates over the injection energy E_{inj} (see Fig. 5.7 for a schematic). On the other hand, we have seen in section 4 that in order to understand the various compensations that take place between the currents coming from different leads, we must add the contributions at a given energy E_{sys} (energy of the electron inside the mesoscopic region, i.e. after the pulse). This is illustrated in Fig. 5.7(b). In case A the injected energy $E_{inj} < E_F$ is close enough to the Fermi energy that the voltage pulse can bring it to an energy $E_{sys} > E_F$ large enough for this contribution not to be compensated by electrons coming from the other side. In case B however, $E_{inj} \ll E_F$ so that $E_{sys} < E_F$ and all contributions are compensated by electrons injected from the right (at energy E_{sys}). Unfortunately, in the

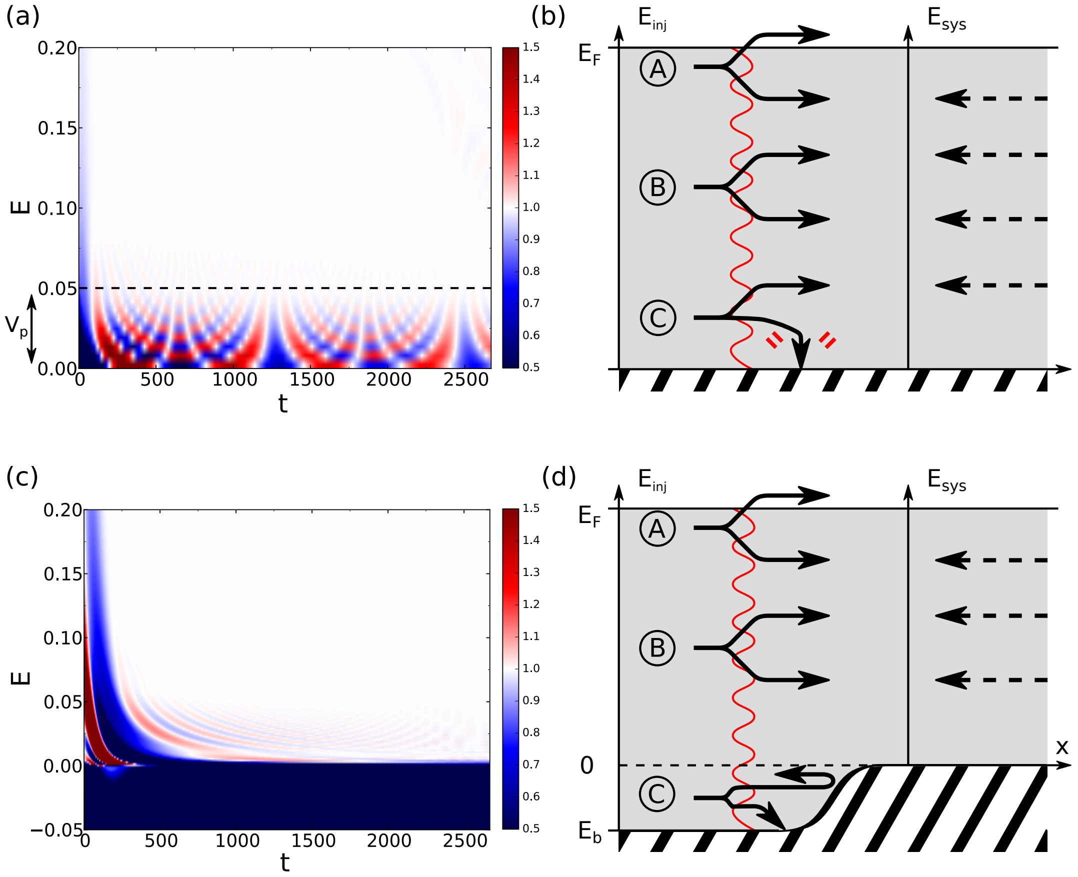

Figure 5.7 – (a,c) Contribution $I(E,t)$ of the left lead to the current $I(t)$ as a function of the injected energy E and time t. The system is the one-dimensional wire described in the introduction of this chapter where one sends a Gaussian pulse, $V(t) = V_p e^{-4log(2)t^2/\tau_p^2}$, with duration $\tau_p = 100\gamma^{-1}$ and amplitude $V_p = 0.05\gamma$. Red (blue) indicates values above (below) one. (b,d) Schematic of the various contributions coming from different energies: Case A: the injected energy E_{inj} is close to the Fermi energy E_F. Case B: the injected energy E_{inj} is well below E_F (these terms eventually give a vanishing contribution). Case C: the injected energy E_{inj} is close to the bottom of the band. These terms also give a vanishing contribution but they relax extremely slowly with time. Lower panels: same as the upper panels but including our energy filtering scheme which removes the contributions from case C.

numerics we only control E_{inj} so that we cannot differentiate between cases A and B and need to integrate over the whole energy range. This is not a real issue, as several tens of energy points are usually enough and these calculations can be performed in parallel. A real difficulty comes from case C where the injected energy E_{inj} is close to the bottom of the band so that after the pulse the electron can end up at a vanishing energy $E_{sys} = 0$ which results in a vanishing velocity. As a result these contributions get stuck at the place where the voltage drop takes place and cannot relax. This is illustrated on the left panel of Fig. 5.7 where we have plotted the current flowing through the device as a function of t and E_{inj}. We find indeed that contributions that are too close to the bottom of the band relax extremely slowly (by too close we mean closer than $\max(V_p, \hbar/\tau_p)$). This makes numerical convergence difficult as one needs very long simulation times to recover particle conservation.

Our strategy to remove the effect of those contributions is to improve our model of the electrodes. In actual experimental setups the electrodes are essentially metallic (high Fermi energy) so that the contributions corresponding to case C are essentially negligible. We therefore add an external potential which is vanishing in the mesoscopic system and negative in the electrode, as seen in Fig. 5.7(d). As the current is measured in the region where this potential vanishes (i.e. on the right in Fig. 5.7), the very low injected energies (case C) will not contribute to the current any more and one recovers particle conservation even for rather small simulation times.

5.5 A COMMENT ON THE ELECTROSTATICS

We end this chapter with a discussion of our choice of boundary conditions in the electrodes and our model for an abrupt voltage drop. Following the usual practice [71], we have assumed (i) that the voltage drops abruptly at the electrode – system interface and (ii) that the electrodes remain at thermal equilibrium (in the basis where the gauge transformation has been performed so that the electrode Hamiltonian is time-independent). Conditions (i) and (ii) correspond to case (a) in Fig. 5.8; an abrupt drop of the electrical potential at the lead – system interface. In an actual experiment, however, a voltage source does not impose a difference of electric potential but rather a difference of *electrochemical* potential. How the latter is split between electrical and chemical potentials is a matter of the balance between the electrostatic and chemical (i.e. kinetic) energies of the system and is therefore extrinsic to the model discussed so far. Fig. 5.8(b,c) illustrate two possible ways of splitting these contributions. In the former case the potential drop is of a purely chemical nature, whereas in the latter the potential drop is purely electrical and is not abrupt. Note that our model, Fig. 5.8(a), implies a small potential mismatch at the electrode – system interface which in turn induces a finite reflection amplitude, which is not the case in Fig. 5.8(b). For DC current with small bias both models coincide, but differences occur at large biases. Fig. 5.9 shows the stationary value of the current after a fast increase of the voltage. We use a pulse of form $w(t) = V\theta(t)$, wait for a long ($t = 100$) time after the voltage has been established and compute the corresponding stationary current (using any of the above equivalent methods, in this case GF-A). One can check from Fig. 5.3 that $t = 100$ is sufficient to achieve convergence toward the stationary value. This can be considered as a very elaborate (and ineffective) way to obtain the $I(V)$ characteristics of the device. We also calculated directly the DC $I(V)$ characteristics using the stationary equations [103] and checked that we obtained matching results. Fig. 5.9 shows two curves. The first curve, Fig. 5.9(a): red circles, corresponds to the natural condition in our formal-

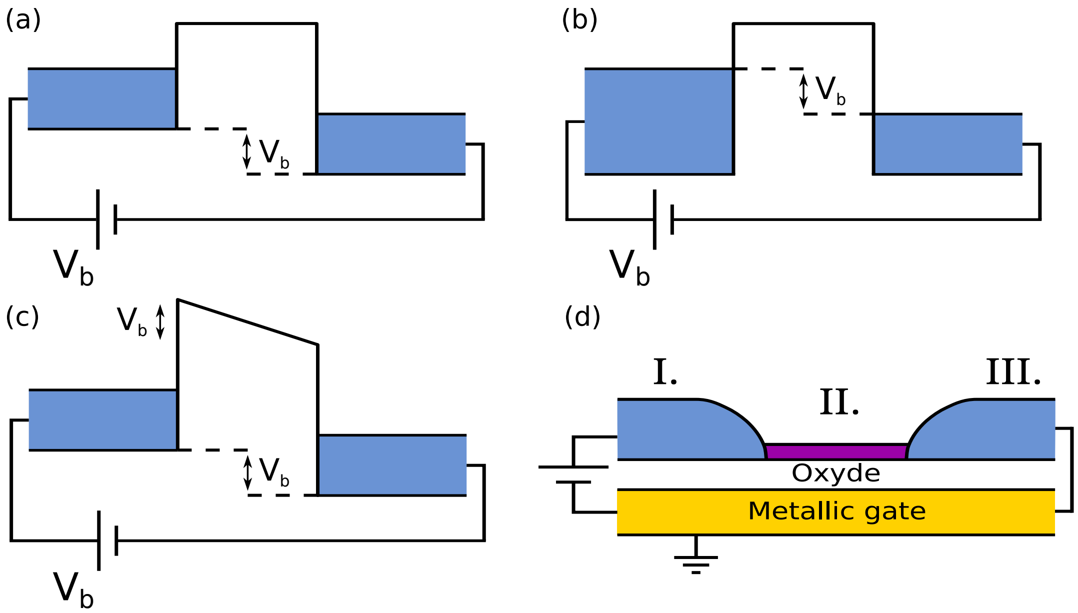

Figure 5.8 – Sketch of different repartitions between chemical and electrical potential upon applying a difference of electrochemical potential V_b between source and drain. (a) Abrupt drop of purely electrical nature. (b) The drop is purely of chemical nature. (c) The purely electric drop takes place linearly over the sample (tunnel junction situation). (d) Device corresponding to case a): the two electrodes I and III correspond to regions with high density of states while the central region II has a low density of states. A metallic gate, at a distance d below the sample, screens the charges present in the sample.

ism (case Fig. 5.8(a)). The voltage drop is a drop of electrical potential, hence there is a corresponding shift of the band of the left lead with respect to the right one. The second curve, Fig. 5.9(b): triangles, corresponds to a change of chemical potential (Fig. 5.8(b), the bottom of the right and left bands remain aligned). When V becomes large compared to the Fermi energy the two prescriptions differ; a drop of electric voltage implies backscattering while in (b) the transmission probability is always unity. Also, a current in (a) implies that the bands in the two leads overlap which does not happen when V is larger than the bandwidth of the system. At large V the current therefore saturates to $2e\gamma/h$ in (b) while it vanishes in (a).

Let us discuss a simple situation which clarifies which boundary condition is the most appropriate for a given situation. A sketch of the system is given in Fig. 5.8(d). It consists of two metallic electrodes I and III with a high electronic density of states (per unit area) ρ_I and ρ_{III} connected to a central device region with lower density of states ρ_{II} (typically a GaAs/AlGaAs heterostructure or a graphene sheet). Underneath the system, at a distance d, is a metallic gate which is grounded. In a typical measurement setup the electrode III is grounded while a voltage source V_b is placed between the electrode I and the metallic gate. Upon imposing the electrochemical potential eV_b in region I, a variation U_I (μ_I) of electrical (chemical) potential takes place with $eV_b = eU_I + \mu_I$. The variation of chemical potential corresponds

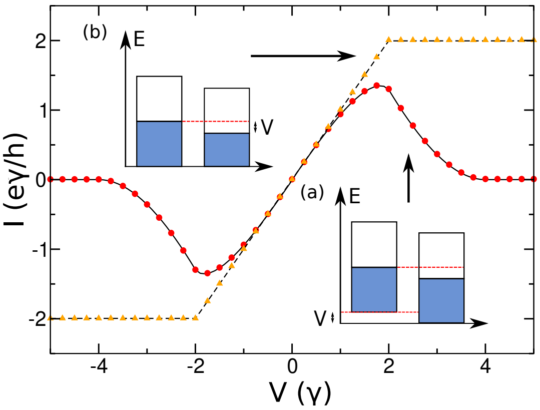

Figure 5.9 – $I(V)$ characteristics of the 1D chain. Symbols: results obtained with GF-A after a fast voltage rise $w(t) = V\theta(t)$ and letting the system equilibrate for $t = 100\gamma^{-1}$. Lines: corresponding pure DC calculation. We compare the case (a) where the drop of potential is purely electrical (triangles, choice made everywhere else in this thesis) and (b) where it is purely chemical (circles). Insets, schematics of the corresponding adjustments of the band positions and Fermi levels. The blue region corresponds to the filled states of the band.

to a variation of electronic density $n_I = \rho_I \mu_I$ (quantum capacitance). On the other hand, the presence of the underlying gate corresponds to an electric capacitance (per unit area) $C = \epsilon/d$ and the electrostatic condition reads $n_I = CU_I/e$. Putting everything together we arrive at,

$$U = \frac{V_b}{1 + C/(e^2\rho_I)}. \tag{5.14}$$

Turning to concrete examples, we find that for typical transition metals (very high density of states) $U \approx V_b$ as raising the chemical potential would imply a huge increase in the density which in turn would induce a correspondingly large increase in the electrostatic energy. Metallic electrodes are thus typically associated with the cases of Fig. 5.8(a) or Fig. 5.8(c). The behavior in region II depends acutely on ρ_{II}. If the density of states in region II is high enough (say a 2D gas with a screening gate at $d = 100$ nm) then the electric potential decays linearly from eV_b (region I) to 0 (region III), as shown in Fig. 5.8(c). If the density of states in region II is small, however, (e.g. one-dimensional systems such as edge states in the quantum Hall regime or a carbon nanotube) the ratio $C/(e^2\rho_I)$ becomes large and U_{II} vanishes [case Fig. 5.8(a)]. We conclude that while the situation depicted in Fig. 5.8(b) is fairly rare (although possible using for instance a graphene electrode coupled through a BN layer to an extremely close underlying graphene gate), the situation of Fig. 5.8(a), which is the focus of this thesis work, is typical of a mesoscopic system. In this case, the drop of the electrical potential will typically take place over a distance d. While the simulation of cases (a) and (c) is straightforward within our formalism, case (b) (fortunately often not realistic) would require additional extrinsic inputs. While the electrical potential adjusts itself instantaneously (i.e. at the speed of light) inside the sample, the chemical potential propagates at the group velocity of the electrons, and a proper model of the inelastic relaxation inside the electrodes would be necessary.

Part III

NEW CONCEPTS AND EXPERIMENTAL PROPOSALS

6

PROPAGATION AND SPREADING OF A CHARGE PULSE

While most elementary courses on quantum mechanics concentrate on the stationary limit, one aspect of the time-dependent theory stands out regarding the spreading of a (mostly Gaussian) wave packet. An initial wave packet with a certain spatial width and average momentum experiences a ballistic motion of its center of mass, while its width spreads diffusively. In this chapter, we study the propagation and spreading of an initial condition given in terms of a voltage pulse. This can be considered as the condensed matter analogue of the spreading of the wave packet. The voltage pulse shares some similarities with the usual "localized wave packet" (where an initial shape is assumed), yet there are also important differences. In particular, in an electronic system, there are stationary delocalized waves which exist before the pulse. Hence, a voltage pulse does not create a localized wave packet but a local deformation of (mostly the phase of) an existing one. We show in this chapter that the spreading of a voltage pulse is accompanied by density (and current) oscillations that follow the propagation of the pulse. While these oscillations spread diffusively, we shall see that the envelope of a voltage pulse spreads linearly with time.

We start with a pedestrian construction of the scattering matrix of a one-dimensional chain. We then leave the discrete model for the continuous limit which is more tractable analytically. We continue with an explicit calculation of the spreading of the wave packet and the above mentioned oscillations that follows the ballistic propagation of the pulse. Finally we leverage these calculations to investigate the spreading of a voltage pulse in the quantum Hall regime. We show that it exhibits a quantum and a "classical" regime we shall distinguish in between by comparing the amplitude and the duration of the pulse. All results presented here are original.

6.1 SCATTERING MATRIX OF A ONE-DIMENSIONAL CHAIN IN PRESENCE OF A VOLTAGE PULSE

Our starting point is the Schrödinger equation for the one-dimensional chain (i.e. the first quantization version of Hamiltonian (5.1) with a static potential $\epsilon_i = 2\gamma$ over the entire infinite chain),

$$i\partial_t \psi_x = -\gamma\psi_{x-1} - \gamma\psi_{x+1} + 2\gamma\psi_x, \ \forall x \neq 0,1 \tag{6.1}$$

$$i\partial_t \psi_0 = -\gamma\psi_{-1} - e^{i\phi(t)}\gamma^t\psi_1 + 2\gamma\psi_0, \tag{6.2}$$

$$i\partial_t \psi_1 = -\gamma\psi_2 - e^{-i\phi(t)}\gamma^t\psi_0 + 2\gamma\psi_1, \tag{6.3}$$

where the hopping element γ_t between sites 0 and 1 can be different from the hopping γ of the rest of the system. As the time-dependent part of the

Hamiltonian concentrates on a single hopping term between sites 0 and 1, we can build the states on either side with a linear combination of the plane waves of the system,

$$\psi_x = \frac{e^{-iEt+ik(E)x}}{\sqrt{|v(E)|}} + \int \frac{dE'}{2\pi}\frac{e^{-iE't-ik(E')x}}{\sqrt{|v(E')|}} r(E',E),\ \forall x \le 0 \tag{6.4}$$

$$\psi_x = \int \frac{dE'}{2\pi}\frac{e^{-iE't+ik(E')x}}{\sqrt{|v(E')|}} d(E',E),\ \forall x \ge 1 \tag{6.5}$$

with $E(k) = 2\gamma(1-\cos(k))$ and $v = \partial E/\partial k$. The wave-matching conditions Eqs. (6.2) and (6.3) translate, for our ansatz, into

$$\begin{aligned}\frac{e^{-ik(E')}}{\sqrt{|v(E')|}} r(E',E) + 2\pi \frac{e^{ik(E)}}{\sqrt{|v(E)|}}\delta(E'-E) = \\ (\gamma^t/\gamma)\int \frac{d\epsilon}{2\pi} K(E'-\epsilon)\frac{e^{ik(\epsilon)}}{\sqrt{|v(\epsilon)|}} d(\epsilon,E)\end{aligned} \tag{6.6}$$

$$\begin{aligned}\frac{1}{\sqrt{|v(E')|}} d(E',E) = (\gamma^t/\gamma)\left[\frac{1}{\sqrt{|v(E)|}} K^*(E-E')\right. \\ \left. + \int \frac{d\epsilon}{2\pi} K^*(\epsilon - E')\frac{1}{\sqrt{|v(\epsilon)|}} r(\epsilon,E)\right]\end{aligned} \tag{6.7}$$

Equations (6.6) and (6.7) can be solved systematically, order by order, in power of γ^t/γ. The first non vanishing term for the transmission reads,

$$d(E',E) = (\gamma^t/\gamma)\sqrt{\frac{v(E')}{v(E)}}\left[1 - e^{2ik(E)}\right] K^*(E-E') + O(\gamma^t/\gamma)^2. \tag{6.8}$$

Of course, Equations (6.6) and (6.7) can also be solved in the wide band limit, as in section 4.2. The wide band limit leads to,

$$r(t,E)e^{-ik(E)} + e^{ik(E)}e^{-iEt} = (\gamma^t/\gamma)e^{i\phi(t)}e^{ik(E)}d(t,E) \tag{6.9}$$

$$d(t,E) = (\gamma^t/\gamma)e^{-i\phi(t)}\left[e^{-iEt} + r(t,E)\right] \tag{6.10}$$

from which we get,

$$d(t,E) = (\gamma^t/\gamma)e^{-i\phi(t)}e^{-iEt}\frac{e^{ik(E)} - e^{-ik(E)}}{(\gamma^t/\gamma)e^{ik(E)} - e^{-ik(E)}} \tag{6.11}$$

which is a simple generalization (for $\gamma^t \neq \gamma$) of the result derived in section 4.2. For $\gamma^t = \gamma$ one obtains $d(E',E) = K^*(E-E')$.

Let us now look at the shape of the transmitted wave that can be reconstructed from the knowledge of $d(E', E)$ and Eq. (6.5). In the wide band limit $E(k') = E(k)$, it reads,

$$\psi(x,t) = \frac{1}{\sqrt{v}} e^{-iEt} e^{ikx} e^{i\phi(t)}. \tag{6.12}$$

We find that in this solution the pulse does not propagate, which is to be expected as the wide band limit neglects the system velocity. Using a linear dispersion relation, $E(k') = E(k) + v(k' - k)$, improves the situation as the corresponding wave function,

$$\psi(x,t) = \frac{1}{\sqrt{v}} e^{ikx - iEx/v} d(t - x/v), \tag{6.13}$$

shows the ballistic propagation of the pulse. In the limit where the velocity of the wave is slow (with respect to the typical scales of the voltage pulse) one can use $d(t, E) = e^{-i\phi(t) - iEt}$, and the wave function reads,

$$\psi(x,t) = \frac{1}{\sqrt{v}} e^{ikx - iEt} e^{-i\phi(t - x/v)} \tag{6.14}$$

At this level of approximation the voltage pulse can be considered as a "phase domain wall" which propagates ballistically inside the wire. The spreading of the voltage pulse is associated with the mass of the particle, i.e. with the curvature of the dispersion relation, and therefore is beyond the linear dispersion considered here. Also, the expression $d(t - x/v) = e^{-i\phi(t - x/v)}$ is slightly ill-defined as it does not fulfill particle conservation (it corresponds to a uniform density yet a non uniform current). This reflects the fact that the transmission matrix itself was calculated in the wide band limit, i.e. without taking the electronic propagation into account.

We continue by taking the continuum limit of the problem, i.e. we introduce a small discretization step a, set $\gamma = \hbar^2/(2ma^2)$ and $k \to ka$. The limit $a \to 0$ provides the usual quadratic dispersion of the Schrödinger equation, $E(k) = \hbar^2 k^2/(2m)$. In this limit, we can solve Eqs. (6.6) and (6.7) for a linear spectrum, beyond the wide band limit. We obtain,

$$\dot{r} - iEr + 2iEe^{-iEt} = (\gamma^t/\gamma) e^{i\phi(t)} [iEd - \dot{d}] \tag{6.15}$$

$$e^{i\phi(t)} d = (\gamma^t/\gamma) \left[e^{-iEt} + r \right] \tag{6.16}$$

where we have used the notation $\dot{r} = \partial_t r(t, E)$. This set of linear equations can be formally integrated and one obtains the correction to the wide band limit. For $\gamma_t = \gamma$, we get,

$$\dot{r} - i(E + w(t)/2) r = ie^{-iEt} w(t)/2. \tag{6.17}$$

Assuming that the voltage is small compared to E, we can neglect $w(t)$ in the left hand side of Eq. (6.17) and obtain,

$$r(E', E) = -\frac{w(E' - E)}{E' + E} + O[w(E)/E]^2 \tag{6.18}$$

where $w(E)$ is the Fourier transform of the voltage pulse $w(t)$, or equivalently,

$$r(t,E) = \frac{i}{2}\int_{-\infty}^{t} du\ e^{-i2Eu+iEt} w(u) \tag{6.19}$$

and

$$d(t,E) = e^{-i\phi(t)-iEt} + \frac{i}{2} e^{-i\phi(t)} \int_{-\infty}^{t} du\ e^{-i2Eu+iEt} w(u) \tag{6.20}$$

It is interesting to look at Eq. (6.20) for a time larger than the total duration of the pulse, so that the integral of the right hand side is simply $w(-2E)$. We get,

$$\boxed{d(t,E) = e^{-i\phi(t)-iEt}[1 + \frac{i}{2} w(-2E) e^{i2Et}] + O[w(E)/E]^2} \tag{6.21}$$

We find that the first correction to the wide band limit corresponds to a beating of frequency $2E$. The corresponding term is, however, very small as $w(\epsilon)$ vanishes when ϵ is larger than $\max(V_p, \hbar/\tau_p)$ which, under the assumptions of the wide band limit, is much smaller than E_F.

As a test of the consistency of our different approaches, Fig. 6.1 shows the transmission probability $d(E', E)$ of the one-dimensional chain as obtained from a numerical calculation [WF-D method followed by the generalized Fisher-Lee formula Eq. (3.62)] and the analytical result $d(E', E) = K^*(E - E')$ in the wide band limit [Eq. (4.21), the Fourier transform was performed numerically]. First, we find that the wide band limit gives excellent results; the analytics match the numerical results even for pulses that are quite large in energy (V_p up to 20% of the injected energy E). Second, we find that, as expected, the characteristic energy for the decay of $d(E', E)$ is indeed given by $\max(V_p, \hbar/\tau_p)$. Last, we find (inset) a large peak of width $\hbar/t_M$ and height $t_M/\hbar$ around $E' = E$. This peak, which converges to $\delta(E' - E)$ when $t_M \to \infty$ corresponds to the fact that for most of the time there is no time-varying voltage in the system which is therefore elastic. This can also be seen from the analytical expression of $K(E)$, which can be obtained in the case of a Lorentzian pulse [41]. Indeed for $w(t) = \frac{2\tau_p}{\tau_p^2 + t^2}$, one obtains,

$$e^{i\phi(t)} = \frac{t - i\tau_p}{t + i\tau_p} \quad \text{and} \quad K(E) = 2\pi\delta(E) - 4\pi\tau_p e^{E\tau_p}\theta(-E) \tag{6.22}$$

6.2 SPREADING OF A VOLTAGE PULSE INSIDE A ONE-DIMENSIONAL WIRE: ANALYTICS

Going beyond the linear dispersion to study the spreading of the voltage pulse is not straightforward using the above wave matching method; we now take a different approach. We consider a pulse with duration τ_p short

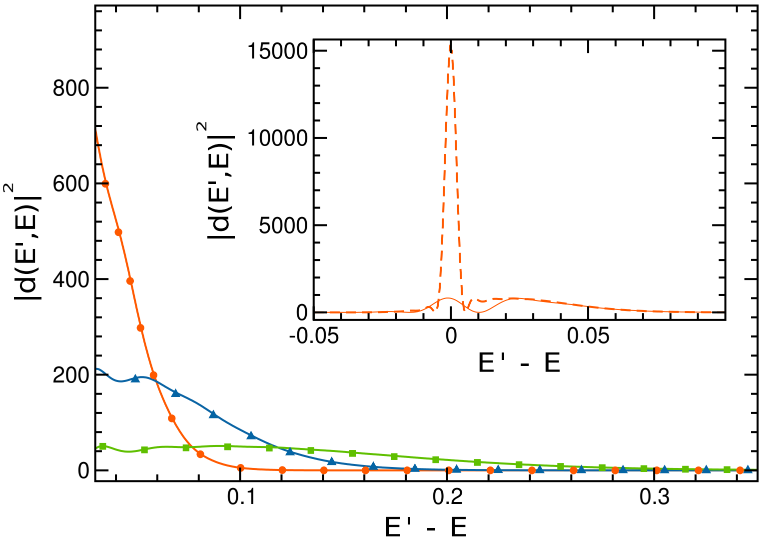

Figure 6.1 – Transmission probability of an incoming particle at energy $E = -1\gamma$ for a Gaussian voltage pulse $w(t) = V_p e^{-4\log(2)t^2/\tau_p^2}$ with amplitude V_p, width τ_p and fixed product $V_p\tau_p = 5.9$. Full lines corresponds to Eq. (4.21) while symbols are numerical results. Orange circles : $V_p = 0.059\gamma$, $\tau_p = 100\gamma^{-1}$, blue triangles: $V_p = 0.118\gamma$, $\tau_p = 50\gamma^{-1}$, green squares: $V_p = 0.236\gamma$, $\tau_p = 25\gamma^{-1}$. Inset: convergence of the discrete Fourier transform for two different values of t_M (same parameters as the orange circles).

compared with the total propagation time that will be considered, yet long with respect to $\hbar/E$. At a small time t_0 just after the pulse we can safely ignore the spreading of the pulse and the wave function is given by

$$\psi(x, t_0) = \frac{1}{\sqrt{v}} e^{-i\phi(-x/v)} e^{-iEt_0} e^{ikx}. \tag{6.23}$$

Eq. (6.23) will be used as our initial condition. As noticed before, the voltage pulse takes the form of a phase domain wall that modifies the existing plane wave, as the function $\phi(-x/v)$ is uniform except within a small window of size $v\tau_p$. We now introduce explicitly the modulation of the plane wave $Y(x, t)$,

$$\psi(x, t) = \frac{1}{\sqrt{v}} Y(x, t) e^{-iEt+ikx}, \tag{6.24}$$

where $Y(x, t)$ verifies $Y(x, t_0) = e^{-i\phi(-x/v)}$. To obtain the evolution of $Y(x, t)$ for times $t > t_0$, we inject the definition of the wave function Eq. (6.24) into the (free) Schrödinger equation and obtain,

$$i\partial_t Y(X, t) = -\frac{1}{2m^*} \Delta_X Y(X, t) \tag{6.25}$$

where the Laplacian $\Delta_X = \partial_{XX}$ acts on the coordinate $X = x - vt$ which follows the ballistic motion of the pulse. Solving this free Schrödinger equation is now straightforward and one proceeds as for a “regular” wave packet. In momentum space we have

$$\Upsilon(X,t) = \int \frac{dQ}{2\pi}\, e^{-iQX} e^{-iQ^2 t/(2m^*)} \Upsilon(Q,t=0), \tag{6.26}$$

with

$$\Upsilon(Q,t=0) = vK^*(Qv). \tag{6.27}$$

In a few cases one knows $K(E)$ explicitly and an explicit formula for the wave function can be obtained. In the case of a Lorentzian pulse, $K(E)$ is given by Eq. (6.22) and the integration in Eq. (6.26) provides an explicit expression,

$$\Upsilon(X,t) = 1 - v\tau_p \sqrt{\frac{2m^*\pi}{it}} \exp\left(\frac{m^*(iX - v\tau_p)^2}{2it}\right) \left[1 + \mathrm{Erf}\left(\frac{iX - v\tau_p}{2\sqrt{it/(2m^*)}}\right)\right] \tag{6.28}$$

with the usual definition of the error function $\mathrm{Erf}(x) = (2/\sqrt{\pi}) \int_0^x e^{-x^2} dx$.

6.3 NUMERICAL CALCULATIONS OF THE SPREADING OF A VOLTAGE PULSE INSIDE A ONE DIMENSIONAL WIRE

The previous form of $\Upsilon(x,t)$ is the voltage pulse analogue of the spreading of a wave packet. It can be recast as a function of the dimensionless position $\bar{X} = X/(v\tau_p)$ and time $\bar{t} = t/[m^*(v\tau_p)^2]$. The typical spreading of the energy components of the pulse takes place diffusively, i.e. $\Delta\bar{X} \propto \sqrt{\bar{t}}$, as for a regular wave packet. However, the peculiarity of the voltage pulse (i.e. it is merely a localized deformation of the phase of an existing stationary wave rather than the modulation of its amplitude) manifests itself in the presence of oscillations in the charge density. Fig. 6.2 shows the calculation of the local charge density,

$$\rho_E(x,t) = |\Psi_E(x,t)|^2 \tag{6.29}$$

obtained from numerical calculations (left panels) and from Eq. (6.28) (upper right panel). The two upper color plots provide the same quantity as calculated numerically (a) and analytically (b). We find that the analytical description is fairly accurate despite various possible sources of discrepancy. The numerics are performed with our tight-binding model which slightly deviates from the continuum and the analytics neglect the quadratic dispersion at small times. A more detailed comparison is shown in Fig. 6.2(d) where we have plotted a cut at fixed x of the local charge density. The lower left plot corresponds to a different (Gaussian) form of the pulse from which a close analytical expression could not be obtained. The most striking feature of the spreading of the voltage pulse is the appearance of density

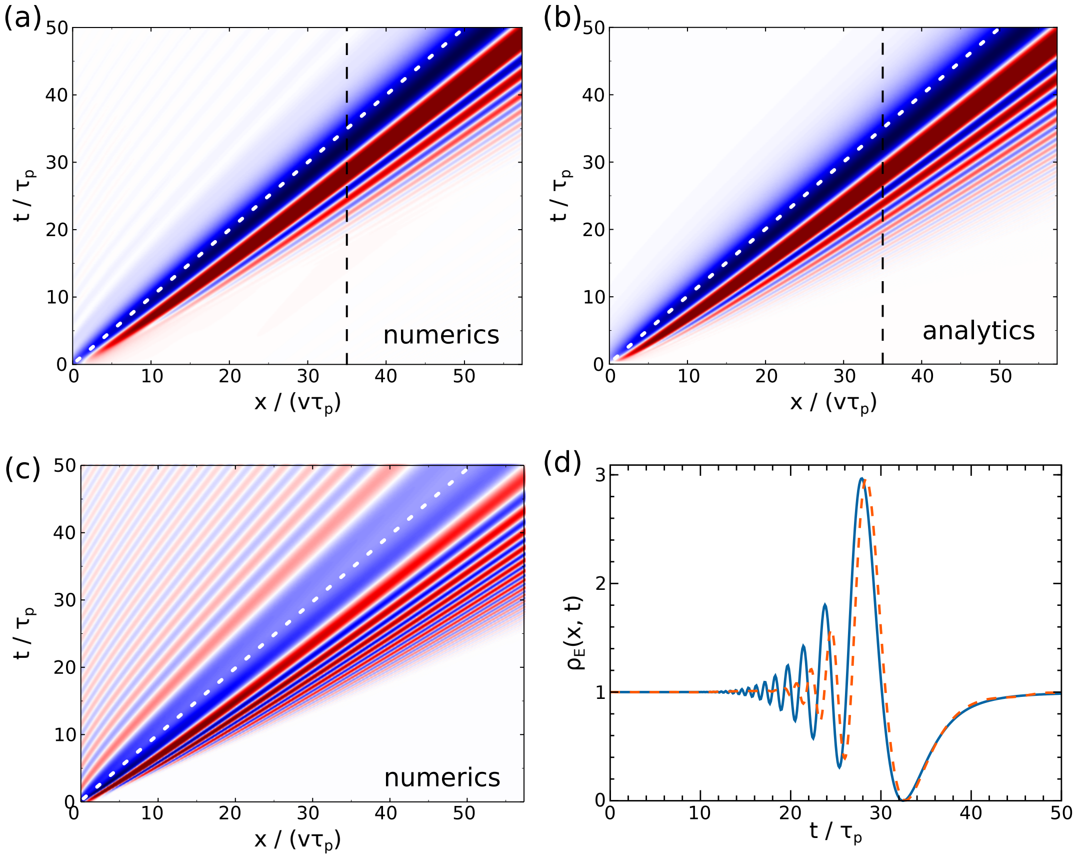

Figure 6.2 – Color plot of the local charge density $\rho_E(x,t)/\rho_E(x,t=0)$ as a function of space (in unit of $v\tau_p$) and time (in unit of τ_p) at energy $E=-1.8\gamma$ and $\tau_p=10\gamma^{-1}$. Levels of red (blue) correspond to local densities higher (lower) than one. The white dashed lines indicate the ballistic propagation $x=vt$. Panels (a) and (b) correspond to a Lorentzian pulse $w(t)=2\tau_p/(\tau_p^2+t^2)$ calculated analytically [right, Eq. (6.28)] and numerically [left]. Panel (c) shows the numerical result for a Gaussian pulse $w(t)=V_p e^{-4log(2)t^2/\tau_p^2}$ with $V_p=0.59\gamma$. Panel (d) shows a cut at $x=35v\tau_p$ of the results of panel (a) (orange dashed line) and panel (b) (full blue line).

oscillations which are reminiscent of a wake. Although we could only analyze these oscillations analytically for the Lorentzian pulse, we actually found them for other shapes, the specificity of the Lorentzian pulse being that these oscillations always travel faster than the Fermi group velocity (the electrons' energy can only increase with a Lorentzian pulse, see Eq. (6.22)). Indeed for a Gaussian pulse (Fig. 6.2(c)), the oscillations also take place *after* the passage of the pulse.

At large time, Eq. (6.28) indicates that the amplitude of $\rho_E(x,t)$ scales as $1/\sqrt{t}$ while the "period" of the oscillations increases as $\sqrt{t}$. More precisely the n^{th} extremum X_n of these oscillations obeys the relation,

$$X_n^2=\frac{2\pi}{m^*}\left(n+\frac{1}{4}\right)\,t+(v\tau_p)^2 \tag{6.30}$$

In other words the positions X_n of the extrema increase diffusively with the quantum diffusion constant $D = h/m^*$. Fig. 6.3 shows the values of X_n as obtained numerically for a Gaussian or a Lorentzian pulse. We first find that the positions of the peaks in front of the pulse is not affected by the shape of the pulse (Lorentzian or Gaussian). Also the peaks behind the pulse (negative n, not present in the Lorentzian case) are positioned symmetrically with respect to the peaks with positive n.

In order to be able to observe these oscillations, one would need Dt to be larger than the original size of the pulse $v\tau_p$ which unfortunately happens to be very difficult. Indeed, one finds $D \approx 10^{-4} - 10^{-2}$ m^2.s^{-1} which translates into $X_1 \approx 1$ nm for a large propagation time $t = 10$ ns that would require, assuming $v \approx 10^4$ m.s^{-1}, a 100 μm long coherent sample and $\tau_p < 100$ fs. This is clearly beyond available technology. In addition, the numerics and expressions obtained so far in this section refer to the contribution to the electronic density $\rho(x,t)$ at a given energy E. This contribution corresponds to the derivative of the corresponding density with respect to the Fermi energy $d\rho(x,t)/dE_F = \rho_{E_F}(x,t)$. It can therefore be, in principle, directly measured by modulating the system with a uniform electrostatic gate, but its main interest lies in the physical insights it conveys. Fig. 6.4 shows full current (integrated over energy) as a function of space and time corresponding to the Gaussian pulse of Fig. 6.2(c). Beside the ballistic propagation of the pulse (at the Fermi velocity), one indeed observes that the oscillating tail survives the integration over energies. Note that these oscillations are reminiscent of other oscillations, associated with shock waves, that were predicted in [106, 107, 108]. In the latter case, a quantum wire was perturbed with a local density perturbation (as opposed to the voltage pulse studied here). However, as those oscillations also appear for a non-interacting gas and a finite curvature is needed to obtain them, they might be related to the present case.

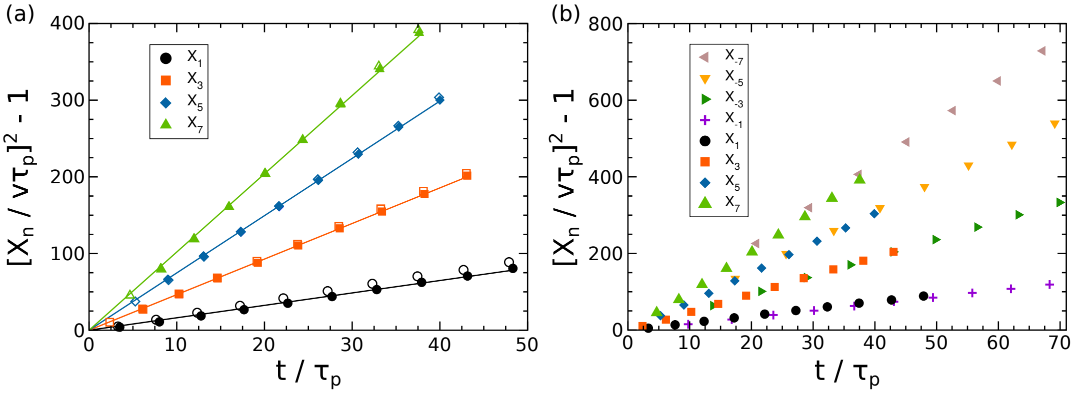

Figure 6.3 – Maxima of the oscillations appearing in Fig. 6.2(a) and Fig. 6.2(c) as a function of time. (a) Full (empty) symbols correspond to the Lorentzian (Gaussian) pulse. Both cases are hardly distinguishable. Lines are linear fits of the numerical data obtained for the Lorentzian case. (b) All symbols correspond to the Gaussian pulse, negative (positive) values of n refer to maxima appearing before (after) the pulse.

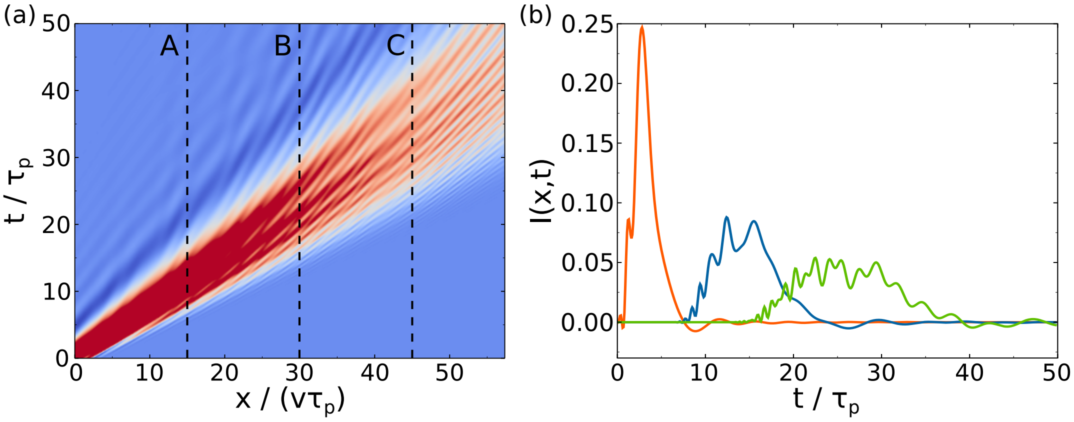

Figure 6.4 – Current density as a function of space (in unit of $v\tau_p$) and time (in unit of τ_p) for the Gaussian pulse of Fig. 6.2(c). Fermi level is set at $E_F = -1.8\gamma$. (a) The color map goes from zero values (blue) to 0.6 (red). (b) cut of the left panel at three positions in space A, B and C corresponding to the three dashed lines shown on the left panel. Orange: $x = 15v\tau_p$, blue: $x = 30v\tau_p$, green: $x = 45v\tau_p$.

6.4 SPREADING OF A CHARGE PULSE IN THE QUANTUM HALL REGIME

We now visualize the spreading of a charge pulse in the quantum Hall regime. We consider a two-dimensional electron gas (2DEG) under high magnetic field connected to two Ohmic contacts as depicted in Fig. 6.5. We work in a regime where the transport properties are fully determined by the lowest Landau levels (LLL). We send voltage pulses via the left contact while the right one is grounded. Fig. 6.5 is not a simple schematic of the system, but shows the electronic charge distribution $\partial\rho(x,y)/\partial V$ appearing in the 2DEG upon applying a DC bias voltage V at the left contact. The Hamiltonian for the system reads

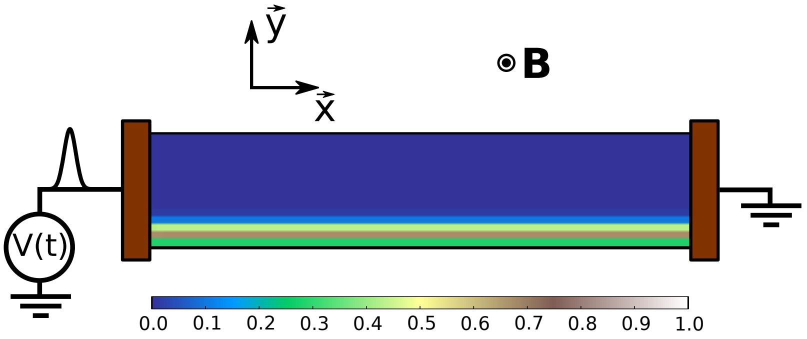

Figure 6.5 – Color map of $\partial\rho(x,y)/\partial V$ of the two-dimensional electron gas showing the position of the edge state at the Fermi energy.

$$\hat{\mathbf{H}} = \frac{(\vec{P} - e\vec{A})^2}{2m^*} + V(\vec{r}, t), \tag{6.31}$$

where $\vec{P} = -i\hbar\vec{\nabla}$, and $\vec{A} = -By\vec{x}$ is the vector potential in the Landau gauge. B is the magnetic field and m^* is the electron effective mass.

$V(\vec{r},t)$ contains the voltage pulse applied to the left Ohmic contact and the confining potential due to the mesa boundary. Equation (6.31) is discretized on a lattice following standard practice [103] with parameters corresponding to a GaAs/AlGaAs heterostructure. We use an electronic density $n_s = 10^{11}$ cm^{-2} which gives a Fermi energy $E_F = 3.47$ meV (or a Fermi wave length $\lambda_F = 79$ nm). We take a magnetic field $B = 1.8$ T that corresponds to a magnetic length $l_B = 19$ nm, and the width of the system is 150 nm.

Fig. 6.6 shows the propagation of a charge pulse generated by a Lorentzian voltage pulse $V(t) = V_p/(1+(t/\tau_p)^2)$, with amplitude $V_p = 0.5$ mV and duration $\tau_p = 5$ ps, applied to the left contact. We represented the deviation of the electronic charge from equilibrium in the center of mass of the pulse at three different times. The corresponding charge integrated along the y-direction is plotted in Fig. 6.7(a). One observes (i) a ballistic propagation at the Fermi group velocity, (ii) a global spreading of the charge pulse and (iii) oscillations of charge density inside its envelope. We already found these oscillations in the previous section, and not only for the Lorentzian pulse. We study the propagation of the pulse in the 2DEG within a Landauer-Büttiker approach using the concept of one-dimensional edge states [109]. The system is invariant by translation in the x-direction, hence in absence of voltage pulse the LLL are eigenstates of the Hamiltonian Eq. (6.31) with the plane waves

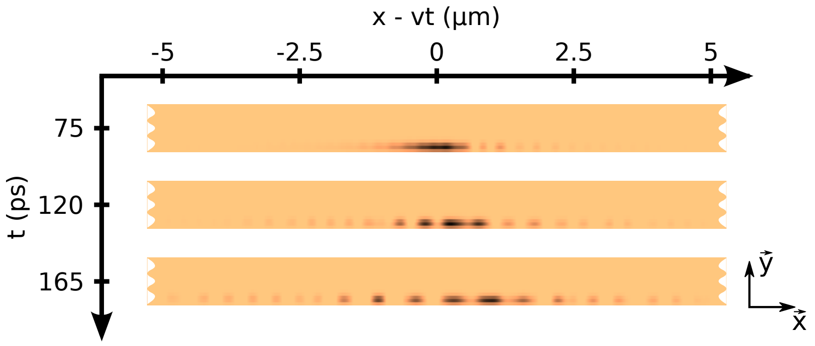

Figure 6.6 – Charge density color map of the spreading of a charge pulse generated by a Lorentzian voltage pulse, $V(t) = V_p/(1+(t/\tau_p)^2)$, with amplitude $V_p = 0.5$ mV and duration $\tau_p = 5$ ps.

$$\psi_k(x,y,t) = e^{-(y-kl_B^2)^2/4l_B^2}\, e^{ikx}. \tag{6.32}$$

Following the results obtained in the previous section, we see that in presence of the voltage pulse, ψ_k becomes $\psi = Y\psi_k$, where Y is given by Eq. (6.28). Here we let the oscillations aside and focus on the spreading of the envelope of the charge pulse $\Delta X(t)$. We will show that the width $\Delta X(t)$ spreads *linearly* in time. $\Delta X(t)$ can be obtained analytically from the exponential decay of $|Y|^2$ with X, or numerically by looking at the envelope of the electronic density $\rho(x,y,t)$. In practice, we calculate $Q(x,t) = \int dy \int_0^x d\bar{x}\rho(\bar{x},y,t)$ and define ΔX as the difference between the

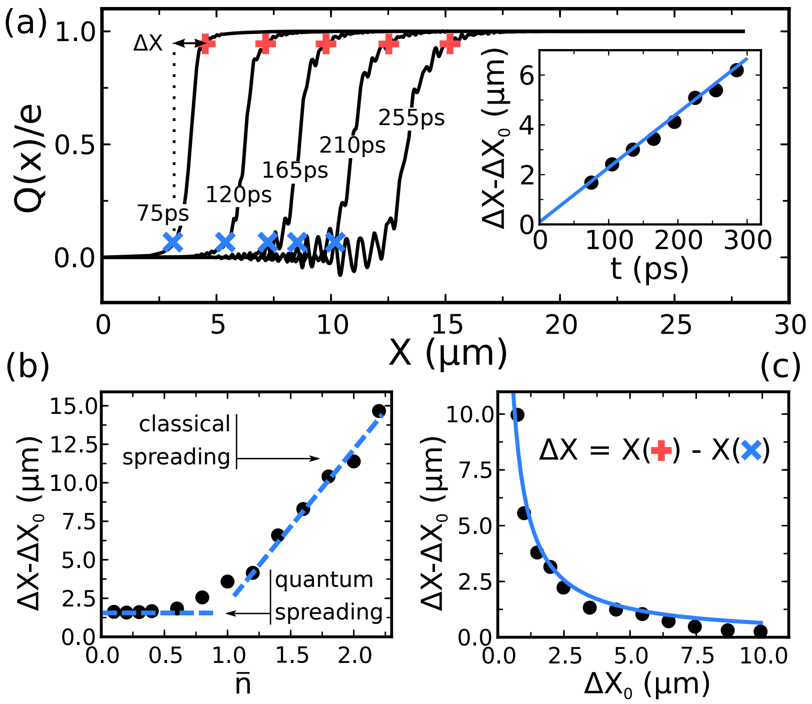

Figure 6.7 – (a) Number of particles as a function of space (integrated along the y-direction). Symbols correspond to 5% (blue cross) and 95% (red pluses) of the particles sent. Inset: spreading of the charge pulse as a function of time. The full line is a linear fit $\Delta X - \Delta X_0 = at$. (b) Spreading of the charge pulse as a function of the number of particles sent $\bar{n}$. The dots correspond to numerical data and the dashed blue lines guide the eye to distinguish between the quantum and the classical regime. (c) Spreading of the charge pulse as a function of its initial spatial extension. The dots are numerical data and the continuous line correspond to the fit $\Delta X - \Delta X_0 = a/\Delta X_0$. Parameters for the Lorentzian voltage pulse: (a) $\tau_p = 5$ ps, $\bar{n} = 1$, (b) $\tau_p = 5$ ps, (c) $\bar{n} = 1$, with $\bar{n} = (e/h)V_p\tau_p/4$. (b) and (c) are calculated at $t = 200$ ps.

blue and red crosses in Fig. 6.7(a). We identify two contributions to the spreading as can be seen in Fig. 6.7(b). First we expand the exponential argument in Eq. (6.28) and find that the spatial extension of the envelope of the charge pulse $\Delta X|_{qu}$ is typically given by

$$\boxed{\Delta X\Big|_{qu} = \frac{t}{m^*\Delta X_0},} \tag{6.33}$$

with $\Delta X_0 = v\tau_p$ the initial spatial extension of the pulse. Fig. 6.7(b) shows that Eq. (6.33) is valid only in the quantum regime that is bounded by $\bar{n} \approx 1$. We shall also consider a "hydrodynamic" aspect of the spreading. This second contribution arises when one considers how the various states ψ_k are filled (with Fermi statistics). Upon varying the potential on the left Ohmic contact between 0 and V_p, one injects particles with different energies and hence different velocities into the system. To first order in V_p, we find that the difference of speed between the fastest and the slowest particles is given by $V_p/(vm^*)$. We recast the amplitude of the voltage pulse in terms of the number of particles it contains $\bar{n} \sim V_p \tau_p$. This yields a "classical" component of the spreading of the charge pulse,

$$\boxed{\Delta X\Big|_{cl} = \frac{\bar{n}t}{m^* \Delta X_0}.} \tag{6.34}$$

The second part of Fig. 6.7(b) ($\bar{n} > 1$) confirms the scaling of Eq. (6.34) with the number of particles injected by the voltage pulse. Overall Fig. 6.7(c) confirms the scaling in $1/\Delta X_0$ of Eqs. (6.33) and (6.34).

We have shown that the transport properties of a voltage pulse applied to an Ohmic contact are closely related to its quantum nature, as we shall continue to see in the next chapter.

7

DYNAMICAL CONTROL OF INTERFERENCE IN MESOSCOPIC DEVICES

In this chapter we start investigating the deviation from the adiabatic limit. We present the new non-trivial physics that emerges when voltage pulses become faster than the characteristic time scales of the devices.

Two competing kinds of dynamical excitations have emerged to inject electrons in nanoelectronic devices. In the first, one fills up the state of a small quantum dot and then rapidly increases its energy to release the electron inside the system [44]. This setup allows the electrons to be injected one by one with a rather well defined energy, but badly defined releasing time. In the second—on which we shall focus here—one simply uses an Ohmic contact to apply a voltage pulse $V(t)$ to the device (well defined in time but ill defined in energy). In a single mode device, such a voltage creates a current $I(t) = (e^2/h)V(t)$ which injects

$$\bar{n} = \int dt \frac{eV(t)}{h} \tag{7.1}$$

electrons inside the system. A voltage pulse will be said to be in the quantum regime when roughly $\bar{n} \approx 1$ electron is injected and the electronic temperature is smaller than the energy scales associated with the height V_p and duration τ_p of the pulse ($\hbar/\tau_p$). In a series of seminal works, Levitov *et al.* studied the properties of pulses of Lorentzian shape [110, 40, 41, 111]. While they found a featureless time-dependent current, they predicted that, in contrast, the current noise could oscillate with the amplitude of the pulse, with the possibility to build noiseless quantum excitations for the particular Lorentzian shape. Recent experiments are beginning to address these proposals [32, 54, 42]. In particular, the quantum regime was reported recently [42].

Here we use voltage pulses to inject charge excitations in an electronic interferometer. We find that ultra fast pulses permit the *dynamical control* of the relative phases of the different paths taken by the electrons, therefore providing means to dynamically engineer the coherent superposition of the traveling waves. We first focus on a simple Fabry-Perot interferometer in one dimension followed by full scale simulations of a two-dimensional Mach-Zehnder interferometer in the quantum Hall regime. Finally, we generalize dynamical control of interference to the raising of a DC bias on the aforementioned interferometers. We find the analogous of the AC Josephson effect in the transient regime. All results presented here are original.

7.1 MODEL AND DC CHARACTERIZATION OF THE FABRY-PEROT CAVITY

Fig. 7.1(a) and Fig. 7.1(b) show our model Fabry-Perot system, it consists of a quantum wire connected to two metallic electrodes. The quantum wire is made into a Fabry-Perot interferometer by means of two barriers (A and B) which can be defects in the wire, gates (as in the sketch) or simply the Schottky barriers that naturally form at the wire-electrode interfaces. Such Fabry-Perot interferometers are standard devices of nanoelectronics and their DC properties have been extensively measured [112, 11, 12, 14].

We model the Fabry-Perot cavity with a one-dimensional Hamiltonian,

$$\hat{\mathbf{H}}(t) = \int dx - \frac{\hbar^2}{2m}\psi^\dagger(x)\Delta\psi(x) + \epsilon(x)\psi^\dagger(x)\psi(x) + \theta(-x)eV(t)\psi^\dagger(x)\psi(x), \tag{7.2}$$

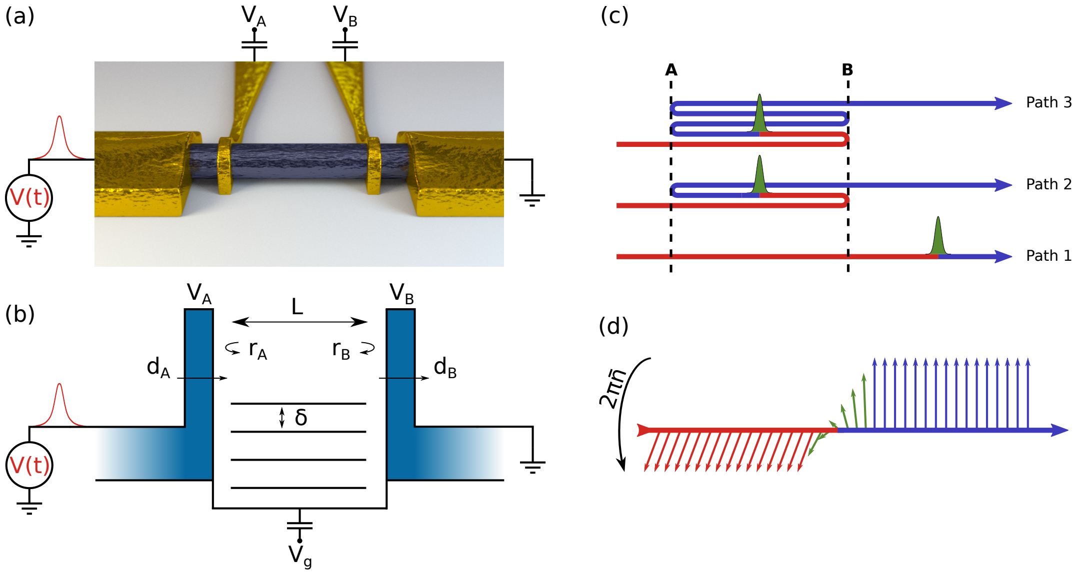

Figure 7.1 – (a,b) Schematic of our setup, a quantum wire connected to two electrodes. Two barriers A and B separated by a distance L are placed along the wire and a Gaussian voltage pulse $V(t)$ is sent from the left. The barriers are characterized by the barrier heights (V_A and V_B) or equivalently by their reflection and transmission amplitudes denoted respectively r_A, r_B and d_A, d_B. A gate voltage V_g allows one to shift the position of the resonant levels of the cavity. The mean level spacing between the discrete levels of the cavity is $\delta = h/(2\tau_F)$ where τ_F is the ballistic time of flight from A to B. (c) Schematic of the physical mechanism for the dynamical control of the interference: as the pulse propagates along the different trajectories, a phase difference $2\pi\bar{n}$ appears between the front (blue) and the rear (red) resulting in a modification of the interference pattern. (d) Graphical representation of Eq. (7.8) that gives the structure of a voltage pulse in terms of a "phase domain wall".

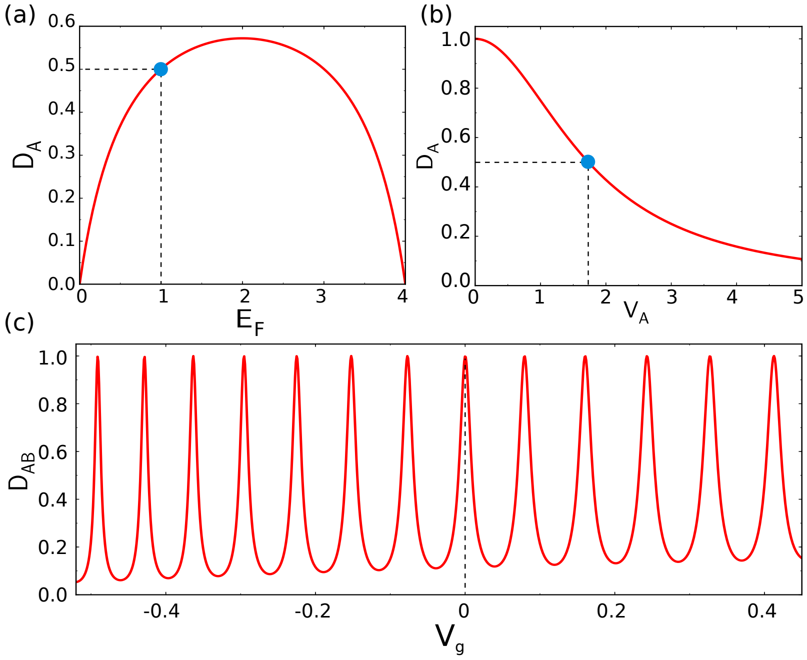

Figure 7.2 – DC characterization of the Fabry-Perot cavity. (a) Transmission of the barrier A against energy E_F with $V_A = 1.73\gamma$. (b) Transmission of barrier A as a function of V_A for $E_F = 1\gamma$. (c) Transmission probability D_{AB} of the entire system with two barriers as a function of V_g for $V_A = V_B = 1.73\gamma$ and $E_F = 1\gamma$ ($D_A = D_B = 0.5$). The parameters of panel (c) correspond to the blue circles of panels (a,b).

where the field operator $\psi(x)$ [$\psi^\dagger(x)$] destroys (creates) an electron at position x, $V(t)$ is the voltage pulse applied on the left electrode ($x < 0$) and $\epsilon(x)$ the static potential that defines the Fabry-Perot (for $x > 0$). We discretize the model on a lattice with lattice distance a and get,

$$\hat{\mathbf{H}}(t) = 2\gamma + \sum_{i=1}^{N+1} \epsilon_i c_i^\dagger c_i - \gamma \sum_{i=-\infty}^{+\infty} c_{i+1}^\dagger c_i - \gamma [e^{i\phi(t)} - 1] c_1^\dagger c_0 + h.c. \tag{7.3}$$

where $\gamma = \hbar^2/(2ma^2)$ and $\phi(t) = \int_{-\infty}^{t} dt'\ eV(t')/\hbar$ (same gauge transformation as in chapter 5 to transform the time-dependent potential for $i \leq 0$ into a time-dependent hopping between sites 0 and 1). The operator c_i ($c_i^\dagger$) destroys (creates) an electron on site i. ϵ_i defines the Fabry-Perot cavity of size $L = Na$: $\epsilon_1 = V_A$, $\epsilon_{N+1} = V_B$ and $\epsilon_i = -V_0 + V_g$ in the central region $i =\in \{2, 3, \dots N\}$.

The basic properties of this interferometer can be understood within an elementary theory. Each barrier A (and B) is described by the amplitude of probability d_A (r_A) for an incident electron to be transmitted (reflected). Summing up the probability amplitudes for all the trajectories (direct transmission: $d_B d_A$, one back and forth bouncing: $d_B r_A r_B d_A$...), the total amplitude of probability for an electron to be transmitted reads,

$$d_{AB}(E) = \frac{d_A d_B}{1 - r_A r_B z}. \tag{7.4}$$

The factor z corresponds to the phase $z = e^{i2kL}$ accumulated by the electron during the time between two collisions (L distance between the scatterers, k electron momentum). z can also be rewritten as $z = e^{i2\tau_F E/\hbar}$, where τ_F is the time of flight between A and B, and E is the incident energy (our analytical treatment ignores the small energy dependence of τ_F, d_A,d_B... but our numerics fully accounts for it). When E is at resonance with the eigenenergies $E_n = n\delta + eV_g$ of the cavity formed by A and B ($\delta = h/(2\tau_F)$: mean level spacing, eV_g: potential shift due to a nearby electrostatic gate), d_{AB} shows a sharp peak and reaches perfect transmission. Fig. 7.2 shows the DC characteristics which were used to calibrate our device with the additional parameter $V_0 = -1.068\gamma$. Fig. 7.2(a) and Fig. 7.2(b) show the transmission probability of a single barrier, say A, as a function of the Fermi energy (a) and V_A (b). Fig. 7.2(c) shows the transmission probability (conductance in unit of e^2/h) of the full Fabry-Perot cavity as a function of the gate voltage V_g for a cavity length set with $N = 70$ and Fermi energy $E_F = 1\gamma$. We can extract the peak to peak mean level spacing $\delta = 0.09\gamma$, and the associated time of flight $\tau_F \approx 35\gamma^{-1}$.

7.2 VOLTAGE PULSES IN THE QUANTUM REGIME

We now apply a (Gaussian) voltage pulse $V(t)$,

$$V(t) = V_p \exp\left(-4\log(2)\frac{t^2}{\tau_p^2}\right), \tag{7.5}$$

of width τ_p and maximum amplitude V_p to the left electrode. The pulse contains $\bar{n} = \kappa e V_p \tau_p/\hbar$ particles where $\kappa = 1/4\sqrt{\pi \log(2)} \approx 0.17$. Various durations of the pulses were used from $\tau_p = 5\gamma^{-1}$ to $\tau_p = 100\gamma^{-1}$. We found that $\tau_p \geq 5\gamma^{-1}$ is necessary to enforce $\hbar/\tau_p \ll E_F$ and get rid of spurious effects associated with the band width of the model. Note that contrary to the noise properties [40, 41, 111], the physics described in this chapter is to a wide extent insensitive to the precise shape of the pulse as will be shown later. Defining the transmitted current $I_t(t)$ just after the second barrier, the observable of interest to us will be the total number $n_t = \int I_t(t)dt/e$ of electrons transmitted through the system. n_t can be directly measured experimentally and requires much less effort than e.g. noise measurements. In an actual experiment, one would measure the DC current I_{dc} upon sending periodic trains of pulses through the system. Indeed, by periodically applying the above pulse with a period $\Theta \gg \tau_p$, one simply finds $I_{dc} = en_t/\Theta$.

The limit of long pulses $\tau_p \gg \tau_F$ is rather trivial. As $V(t)$ varies very slowly, at each instant the current follows the DC I-V characteristics of the system, $I_t(t) = I_{dc}[V(t)]$ (adiabatic limit) which can be obtained from the Landauer formula. In this limit, $V_p \ll \delta$ (linear regime) leads to $n_t = |d_{AB}(E_F)|^2\bar{n}$, while for large voltages $V_p \gg \delta$ (classical limit) the interference pattern is washed out and one obtains $n_t = D^{cl}_{AB}\bar{n}$, where the classical

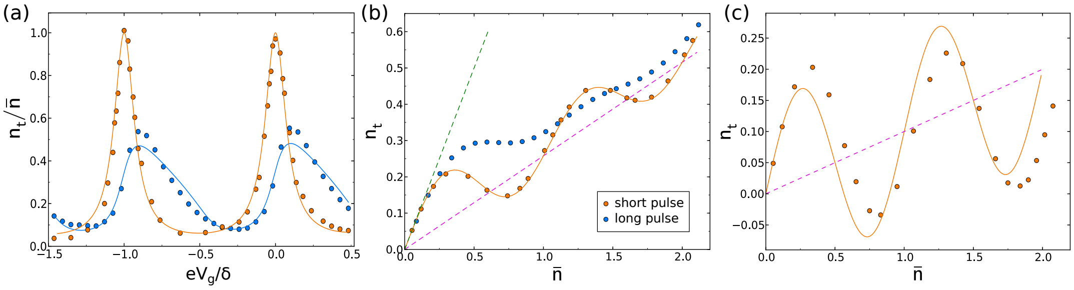

Figure 7.3 – Total charge transmitted n_t. (a) n_t as a function of gate voltage eV_g/δ. (b,c) n_t as a function of total injected charge $\bar{n}$. The symbols correspond to numerical data for short (red, $\tau_p = \tau_F/7$) and long (blue, $\tau_p = 3\tau_F$) pulses while the full lines correspond to the analytical results for $\tau_p \ll \tau_F$ (red) and $\tau_p \gg \tau_F$ (blue). (a) $V_p = 0.5\delta$ and $D_A = D_B = 0.5$. (b,c) System at resonance and V_p is varied with $D_A = D_B = 0.5$ (b), and $D_A = D_B = 0.1$ (c). Dashed lines: $n_t = D_{AB}\bar{n}$ (green) and $n_t = D_{AB}^{Cl}\bar{n}$ (magenta).

(or incoherent) probability D_{AB}^{cl} corresponds to the addition law of the probabilities associated with the different paths [94],

$$D_{AB}^{cl} = \frac{D_A D_B}{1 - R_A R_B}, \tag{7.6}$$

capital letters D or R correspond to the probabilities associated with the respective amplitudes so that $D_A = |d_A|^2$. Eq. (7.6) is essentially identical to Eq. (7.4) upon replacing amplitudes by probabilities. So far, we have made rather standard predictions which are easily reproduced by our numerical simulations: the blue symbols in Fig. 7.3 show that n_t oscillates with the gate voltage V_g (Fig. 7.3(a)) and increases monotonously with V_p (Fig. 7.3(b)). Fig. 7.3(a) has been calculated with an intermediate value of $V_p \approx 0.5\delta$ so that the contrast of the interference pattern is not very large.

Having established the adiabatic limit, we can now turn to the more interesting limit of short pulses $\tau_p \ll \tau_F$ for which a proper time-resolved quantum theory is compulsory. Let us make a naive guess: a very short pulse can be viewed as a very localized perturbation that will propagate ballistically through the wire. Monitoring the current after the barriers, one observes a narrow peak when the perturbation has propagated up to the observation point. $2\tau_F$ later one observes a second peak corresponding to trajectories with one reflection on each barrier, new peaks (of increasingly smaller amplitudes) arrive sequentially every $2\tau_F$. As the perturbations coming from different trajectories do not coincide in time, they cannot interfere and one expects to observe the "classical" addition law $n_t = D_{AB}^{cl}\bar{n}$. The argument can also be made in the energy domain: a fast pulse excites electrons to a large spread in energy which results in an effectively random phase z and the interference pattern gets washed out. A rapid glance at the numerics does indeed confirm this picture. Fig. 7.4(b) shows the monitored current $I_t(t)$ which clearly shows the peaks described above. Perhaps more transparent is the corresponding color map of the local current $I(x,t)$

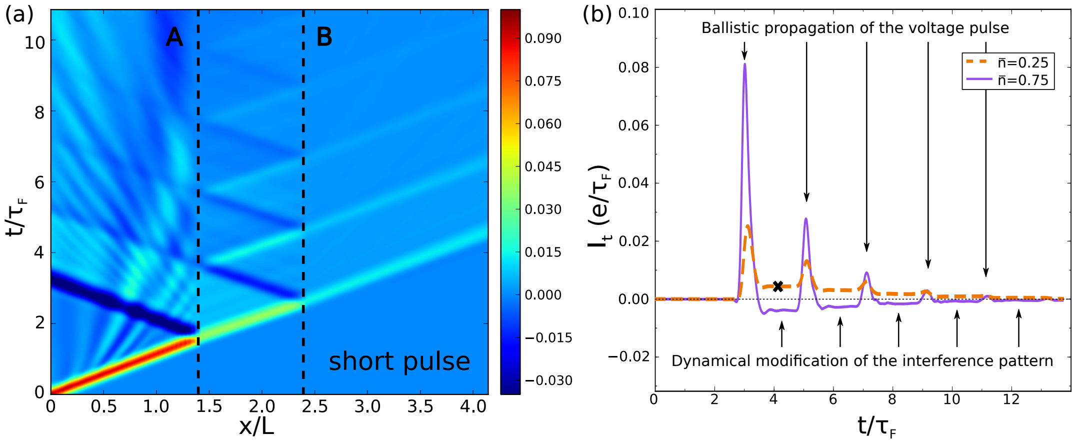

Figure 7.4 – (a) Local current $I_t(x,t)$ as a function of space (in unit of the length L of the cavity) and time (in unit of τ_F) for $V_p = 1.5\delta$, $\tau_p = \tau_F/3.5$ and the cavity is at resonance. The dashed lines indicate the positions of the barriers. (b) $I_t(x_0,t)$ for $x_0 = 2.5L$ on the right of the second barrier B. In orange: $V_p = 1.5\delta$, in purple: $V_p = 4.5\delta$ and for both curves $\tau_p = \tau_F/3.5$. The black cross ($\times$) marks the time associated with Fig. 7.1(c).

in Fig. 7.4(a) where the different trajectories with multiple reflections are clearly visible. In contrast, long pulses have an essentially featureless current $I_t(t)$ of the same shape as the voltage pulse, as can be seen in Fig. 7.5.

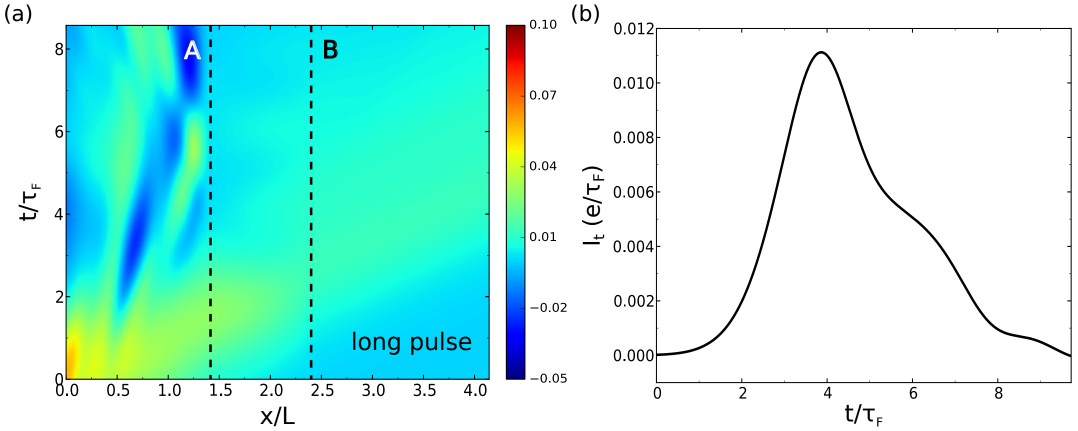

Figure 7.5 – (a) Local current $I_t(x,t)$ as a function of space (in unit of the length L of the cavity) and time (in unit of τ_F) for $V_p = 1.5\delta$, $\tau_p = 3\tau_F$ and the cavity is at resonance. The dashed lines indicate the positions of the barriers. (b) $I_t(x_0,t)$ for $x_0 = 2.5L$ on the right of the second barrier B.

The story could end here: slow pulses allow one to observe the interference effects (wave aspect of quantum mechanics) while fast pulses give access to the ballistic propagation and reflection/transmission of the charges injected by the pulse (particle aspect of quantum mechanics). A deeper look at the numerics reveals however a handful of rather counter-intuitive physical effects. First, one observes in the $I_t(t)$ plot of Fig. 7.4(b) that the current does not vanish in between consecutive peaks. Second, Fig. 7.3 shows that the total number of transmitted electrons in fact oscillates strongly with the gate voltage (Fig. 7.3(a)) in total contradiction with the above picture. Indeed, upon using faster pulses, one actually restores the interference pattern that was somewhat smeared in the long pulse case. Third, and even more striking, are Fig. 7.3(b) and Fig. 7.3(c) which show that the number of transmitted electrons actually *oscillates* with the number of injected electrons $\bar{n}$. Fig. 7.3(c) is particularly intriguing since for $\bar{n} = 0.8$, n_t, e.g. the DC current for a train of pulse, is *negative*. In other words, one raises the energy of the electrons on the left and the electrons flow *toward* the left electrode.

7.3 DYNAMICAL CONTROL OF INTERFERENCE PATTERN

To understand the regime of fast pulses, one needs to develop a proper representation of what a fast voltage pulse really does to the electronic wave function already present in the system (before any pulse was sent).

7.3.1 *Propagation of a phase domain wall*

The naive image where a voltage pulse generates some sort of localized wave packet that propagates through the system is, to a large extent, wrong. In contrast, stationary delocalized waves already exist before the pulse. Ignoring for a moment the presence of the interferometer (barriers), the stationary wave function is a simple plane wave $\Psi(x,t) = e^{ikx-iEt}$. Upon applying a voltage pulse $V(t)\theta(-x)$ (we suppose that the voltage drop is very abrupt spatially for the sake of the argument, $\theta(x)$ is the Heaviside function), the energy of the wave is increased and the wave function starts to accumulate an extra phase $\phi(t) = \int_{-\infty}^{t} du\; eV(u)/\hbar$ for $x < 0$. Noting that $\lim_{t\to\infty} \phi(t) = 2\pi\bar{n}$, one finds that the wave function after the pulse was sent takes the form,

$$\begin{aligned} \Psi(x,t) = e^{-i2\pi\bar{n}+ikx-iEt/\hbar} \quad &\text{for} \;\; x < 0 \\ \Psi(x,t) = e^{+ikx-iEt/\hbar} \quad &\text{for} \;\; x > 0. \end{aligned} \tag{7.7}$$

The effect of a voltage pulse is therefore to generate a kink in the phase of the electronic wave function $\Psi(x,t)$ (see Fig. 7.1(d) for a schematic). In other words, what propagates is essentially a “phase” domain wall between two regions which are characterized by an $e^{i2\pi\bar{n}}$ phase difference. Phases in quantum mechanics cannot be observed directly and one has to resort to interferences between different paths to observe them. The role of the electronic interferometers used here is to introduce these different paths. While the argument above is very naive, it correctly captures the main feature of the wave function which reads (for a linearized spectrum),

$$\Psi(x,t) = e^{-i\phi(t-x/v)+ikx-iEt/\hbar}, \tag{7.8}$$

where $v = (1/\hbar)\partial E/\partial k$ is the group velocity.

Let us now return to our Fabry-Perot cavity. In this case, the stationary wave is not a simple plane wave but a superposition of several waves corresponding to the different paths that the electrons can take (with zero, one, two... reflections) as shown in Fig. 7.1(c). When a voltage pulse is sent through this superposition of paths, it propagates through the various paths. Fig. 7.1(c) corresponds to a snapshot at a particular time where the pulse has emerged from the direct path (Path 1 of stationary amplitude $d_B d_A$) but not yet from the longer trajectories with multiple reflections (Path 2 of amplitude $d_B(r_A r_B)d_A$, Path 3 of amplitude $d_B(r_A r_B)^2 d_A \dots$). The time at which this snapshot is taken corresponds to the cross in the $I_t(t)$ plot of Fig. 7.4(b). If one looks at the wave function just after the barrier B at that particular time, one finds that the amplitude of Path 1 has an extra phase $e^{i2\pi\bar{n}}$ compared to its stationary value (rear of the pulse as compared to Path 2, 3,... which are still in the front of the pulse). Therefore at this particular time, the total amplitude is $e^{i2\pi\bar{n}} d_B d_A + d_B(r_A r_B)d_A + d_B(r_A r_B)^2 d_A \dots$ and is *dynamically modified* with respect to its stationary value. As time increases, the pulse will emerge from Path 2, Path 3...and the factor $e^{i2\pi\bar{n}}$ will progressively spread to all trajectories until one recovers the stationary amplitude (up to a now irrelevant global $e^{i2\pi\bar{n}}$ phase factor). After emerging from path p, the total amplitude of transmission reads,

$$d_{AB}^{(p)}(E) = d_{AB}^{(0)}(E) + (e^{i2\pi\bar{n}} - 1) d_A d_B \frac{1 - (r_A r_B z)^p}{1 - r_A r_B}, \tag{7.9}$$

where $d_{AB}^{(0)}(E)$ is given by Eq. (7.4). Hence we find the net current between paths p and $p+1$ with the Landauer-Büttiker formula,

$$I_t^{(p)} = \int dE f(E) \left[|d_{AB}^{(p)}(E)|^2 - |d_{AB}^{(0)}(E)|^2 \right], \tag{7.10}$$

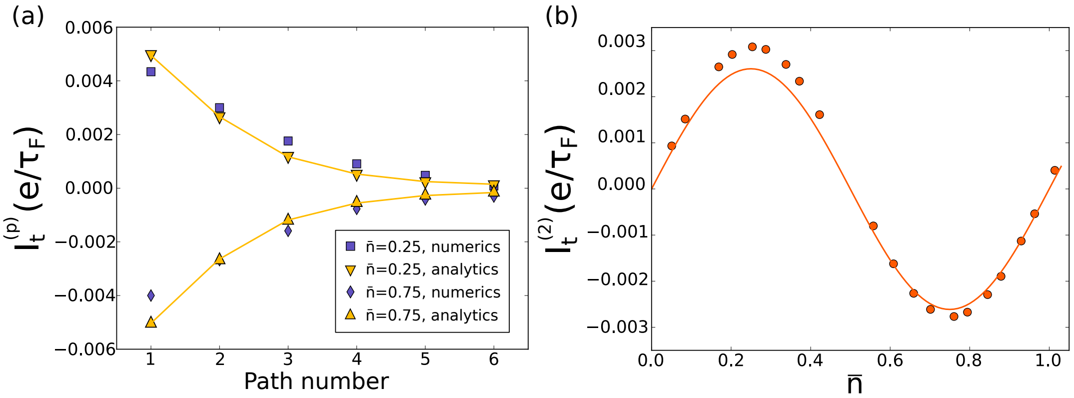

Figure 7.6 – Particle current resulting from the modification of the interference pattern. (a) Current between paths p and $p+1$. Purple symbols correspond to the numerical data of Fig. 7.4(b), and the yellow line marked by yellow symbols is the numerical evaluation of Eq.(7.11). (b) Current of the second plateau ($p = 2$) as a function of the number of injected particles $\bar{n}$. Symbols are the numerical data from the simulations, and the full line correspond to the evaluation of Eq. (7.11) with $p = 2$.

which yields,

$$I_t^{(p)} = \int dE f(E) D_{AB}(E) \left[|1 + (e^{i2\pi\bar{n}} - 1)(1 - (r_A r_B z)^p|^2 - 1 \right]. \quad (7.11)$$

The integral of Eq. (7.11) was calculated numerically and the result is shown in Fig. 7.6(a) for $\bar{n} = 0.25$ and $\bar{n} = 0.75$. The agreement with the numerics validates the above argument for the origin of the plateaus observed in Fig. 7.4(b). Fig. 7.6(b) shows that the value of the current oscillates with $2\pi\bar{n}$ which consequently explains the oscillations of n_t.

This mechanism, to which we refer to as the *dynamical control of the interference pattern*, is a key concept of this thesis.

7.3.2 *Analytical calculation of the number of transmitted particles*

As we just did for the current between the ballistic peaks, we can make the above arguments more quantitative also for the number of transmitted particles, and in particular properly take into account the Fermi statistics for the filling of the stationary states. Our starting point for the calculation of n_t is Eq. (4.25),

$$n_t = \int \frac{dE}{2\pi} \frac{dE'}{2\pi} |d(E', E)|^2 [f(E) - f(E')] \quad (7.12)$$

where $d(E', E)$ is the amplitude of probability for an incident electron coming from the left with energy E to be transmitted with energy E'. $d(E', E)$ can be further decomposed into

$$d(E', E) = d_v(E' - E) d_{AB}(E') \quad (7.13)$$

where the first (inelastic) term originates from the voltage drop while the second comes from the (elastic) Fabry-Perot cavity. For the derivation of Eq. (7.12), we have made use of the fact that the transmission amplitude $d'_v(E' - E)$ for electrons coming from the right is given by $d'_v(E' - E) = d^*_v(E - E')$. As we explained in chapter 4, Eq. (7.12) as a whole is a perfectly convergent integral whose integrand is concentrated around the Fermi level (assuming the voltage pulse is slow enough compared to $\hbar/E_F$). However each of its two sub terms spread over the entire band of the model, so one should refrain from calculating these two terms separately, if possible. Eq. (7.12) has a nice straightforward interpretation: one simply sums over the (incoherent) incoming states and calculates their total transmission probabilities regardless of the final energy. In the absence of voltage pulse the vanishing n_t comes from the compensation between electrons coming from the left and from the right.

Our model for the Fabry-Perot transmission amplitude has been given in the previous paragraph. In the limit where the pulse is slow $\tau_p \gg \hbar/E_F$, and $V_p \ll E_F/e$ is low compared to the Fermi energy, (the case of interest for our nanodevices), $d_v(E'-E)$ is given by Eq. (4.21) and we recover the result of [41],

$$d_v(E'-E) = \int dt e^{i(E'-E)t} e^{-i\phi(t)}. \tag{7.14}$$

To proceed, we expand $d_{AB}(E)$ in terms of the different paths

$$d_{AB}(E) = \sum_{n=0}^{\infty} d_A d_B (r_A r_B)^n e^{2i\tau_F(E+eV_g)n}, \tag{7.15}$$

and introducing $\epsilon = E' - E$, we get

$$\begin{aligned} n_t = \int \frac{dE}{2\pi}\frac{d\epsilon}{2\pi} \sum_{n,m} |d_v(\epsilon)|^2 D_A D_B (r_A r_B)^{n+m} \times e^{2i\tau_F(E+eV_g)(n-m)} \\ \times [f(E-\epsilon) - f(E)]. \end{aligned} \tag{7.16}$$

We can now perform the integration over E (at zero temperature) which binds together the two parts of the integral. The terms $n = m$ and $n \neq m$ need to be considered separately, and we get,

$$\begin{aligned} n_t = D_{AB}^{cl} \int \frac{d\epsilon}{2\pi} |d_v(\epsilon)|^2 \epsilon + \int \frac{d\epsilon}{2\pi} |d_v(\epsilon)|^2 \frac{D_a D_b}{2\pi} \\ \times \sum_{n \neq m} (r_a r_b)^{n+m} \frac{e^{i\alpha_g(n-m)}}{i2\tau_f(n-m)} (e^{i2\tau_f \epsilon(n-m)} - 1) \end{aligned} \tag{7.17}$$

with $\alpha_g = 2\tau_F(E_F + eV_g)/\hbar$. We can now replace $d_v(\epsilon)$ by its expression Eq. (7.14) and performing the integral over ϵ, we arrive at

$$\begin{aligned} n_t = D_{AB}^{cl}\bar{n} + \sum_n \sum_{m \neq n} \frac{D_A D_B}{2\pi} (r_a r_b)^{n+m} \frac{e^{i\alpha_g(n-m)}}{i2\tau_F(n-m)} \\ \times \int dt \left[e^{-i\phi(t)} e^{i\phi(t+2\tau_F(n-m))} - 1 \right] \end{aligned} \tag{7.18}$$

Eq. (7.18) applies for all pulses, short and long. Assuming an infinitely short pulse $\phi(t) = \theta(t) e^{i2\pi\bar{n}}$, we obtain after integration and resummation of the geometric series,

$$\boxed{\begin{aligned} n_t\big|_{short} = D_{AB}^{cl}\,\bar{n} + (D_{AB}(V_g) - D_{AB}^{cl}) \frac{\sin(2\pi\bar{n})}{2\pi} \\ - \frac{2 D_{AB}(V_g) D_{AB}^{cl} r_a r_b}{\pi D_A D_B} \sin^2(\pi\bar{n}) \sin(2\pi V_g/\delta). \end{aligned}} \tag{7.19}$$

In the case of very long pulses $\phi(t)$ evolves very slowly with respect to τ_F so that one expands $\phi(t + a\tau_F) \approx \phi(t) + a\tau_F eV(t)/\hbar$. In this limit, Eq. (7.18) allows one to recover the adiabatic result,

$$n_t\big|_{long} = \int dt \int_{E_F}^{E_F+V(t)} \frac{de}{2\pi} D_{AB}(e). \tag{7.20}$$

Eq. (7.19) contains two contributions of different kind: the first term, "particle" like, accounts for the ballistic propagation of the pulse while the second and third terms, "wave" like, corresponds to the dynamical modification of the interference pattern discussed above which originates from the difference of phase between the front and the back of the pulse. This interference effect dominates for a resonant Fabry-Perot in the tunneling regime ($D_A, D_B \ll 1$) where the "particle" term vanishes and one observes a purely oscillating signal $n_t = [\sin(2\pi\bar{n})]/(2\pi)$, see the right panel of Fig. 7.3. In particular for $\bar{n} = 3/4$, one finds a *negative* transmitted charge $n_t = -1/(2\pi)$ which is a pure interference effect: the $e^{i3\pi/2}$ phase of the pulse dynamically brings the Fabry-Perot cavity out of resonance and as a result, the particles coming from the left are temporarily blocked. The electrons coming from the right, on the contrary, are not affected by the pulse. Therefore the current compensation between left and right is temporarily withstood and one observes a negative net current (see the purple line in Fig. 7.4(b) for instance).

7.3.3 *Interference visibility with temperature and pulse characteristics*

The requirements to observe the above predictions experimentally are threefold. (i) One needs a device where Fabry-Perot interferences can be observed at DC which implies that the temperature $k_B T$ is smaller than the mean level spacing $\delta = h/2\tau_F$ of the cavity. (ii) One needs values of τ_F long enough compared to the speed of available pulse generators. (iii) An important ingredient of the modeling is that the voltage drop needs to be spatially abrupt (with respect to the distance L between the two barriers A and B). The spatial shape of the voltage drop is controlled by the ratio between the electric C and quantum $e^2\rho$ capacitances of the system, as discussed earlier in section 5.5. In order to obtain a large ratio $C/(e^2\rho)$ one needs a very small density of state ρ and/or to use nearby metallic gates in order to obtain an efficient screening of the charges inside the device. Requirement (iii) requires some care but various strategies can be used to enforce it, such as depositing screening gates close to the electron gas or using systems with extremely low density of states. One needs $\delta \geq 10 k_B T$ in order to fulfill (i) with a good contrast which translates into $\tau_F \leq 250$ ps for a typical dilution fridge temperature of 10 mK. This in turn imposes a pulse duration $\tau_p \approx 100$ ps to enter the regime of fast pulses. Such requirements are stringent but definitely within grasp of current technology.

Fig. 7.7(a) shows the resonant and off resonance signal $n_t/\bar{n}$ as a function of the maximum voltage V_p/δ for both short and long pulses. As the visibility of the fast pulses is sensitive to $\bar{n}$ and not to V_p/δ [Eq. (7.19)], we find that the system can retain a high visibility for $V_p > \delta$ while the interference pattern of the long pulse is totally smeared out. We study in Fig. 7.7(b) the temperature dependence of n_t at and off resonance. We find that a low $k_B T \leq 0.1\delta$ temperature is needed to observe interferences with a good visibility. This requirement is as stringent as the DC requirement but not more,

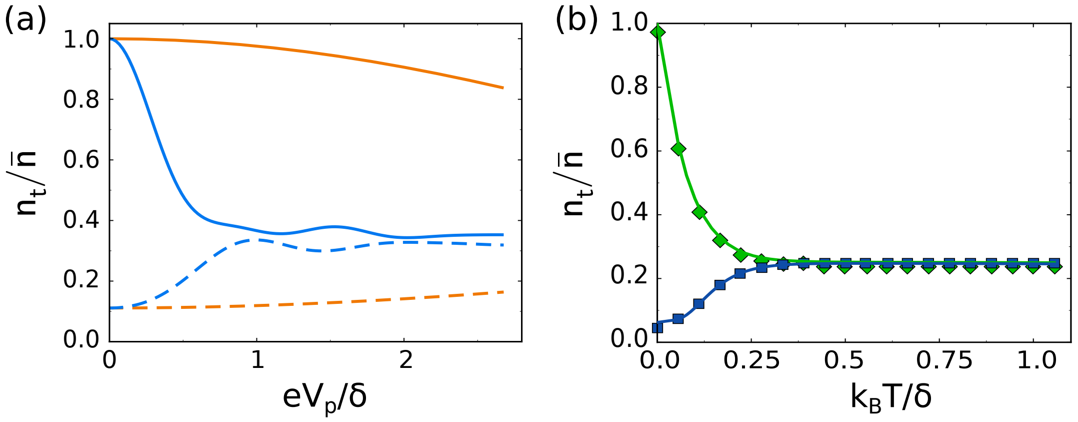

Figure 7.7 – (a) Transmission probability $n_t/\bar{n}$ as a function of V_p/δ for a system at resonance (full lines, $V_g = 0$) and off resonance (dashed line, $V_g = \delta/2$) for a short (orange, $\tau_p = \tau_F/7$) and long (blue, $\tau_p = 3\tau_F$) pulse. $D_A = D_B = 0.5$. (b) Transmission probability $n_t/\bar{n}$ as a function of temperature for the same short pulse and $V_p = 0.5\delta$. Symbols: numerical results, lines: energy average $\langle -D_{AB}(V_g, E)\partial_E f(E)\rangle_E$. The upper curves correspond to $V_g = 0$ (resonance) while the lower one is off resonance $V_g = \delta/2$.

so that temperature should not be a restriction for the observation of the effects predicted.

Regarding the specific question of the shape of the pulse, Fig. 7.8 presents the number of transmitted electrons as a function of the injected one for two different pulse shapes: a Gaussian pulse [Eq. (7.5)] and a Lorentzian one ($V(t) = V_p/(1 + 4t^2/\tau_p^2)$). We find, as expected from the analytical calculation, that the results are insensitive to the shape of the pulse in the fast pulse limit and we recover the oscillating behavior with respect to $\bar{n}$. We emphasize that this is in sharp contrast with the current noise in the single barrier case studied in [41].

7.4 TOWARDS EXPERIMENTS WITH THE MACH-ZEHNDER INTERFEROMETER

There are many possible systems where the physics we present could be measured. Recent progress on Thz detection were made with carbon nanotubes [54], for instance, although these objects are rather small (which implies small time of flight hence the THz physics). Here we explore an implementation, perhaps the simplest one, where the interferometer is constructed out of the edge states of a two-dimensional electron gas in the quantum Hall regime [112]. The one-dimensional edge states have very low density of states and can be further screened by nearby metallic gates or other nearby edge states (at filling factor two). With drift velocities $v_D \approx 10^4 - 10^5$ m.s^{-1} and a phase coherence length [113] $L_\phi \approx 20$ μm at

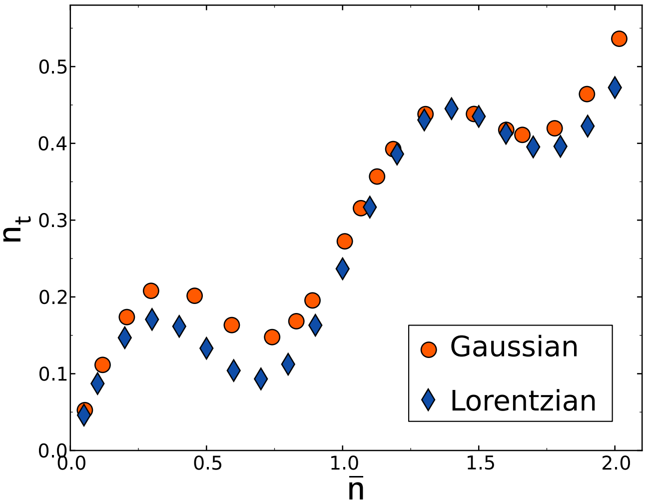

Figure 7.8 – Transmitted charge n_t as a function of total injected charge $\bar{n}$. The system is at resonance and V_p is varied with $D_A = D_B = 0.5$. Orange circles are the data of the short Gaussian pulse case from Fig. 7.3(b), blue diamonds correspond to a Lorentzian shaped pulse with width $\tau_p = \tau_F/7$.

20 mK, one finds that a rather large system of length of a few micrometers should meet the requirements.

7.4.1 *Simulation of an electronic Mach-Zehnder interferometer*

We simulated an electronic analogue of a Mach-Zehnder interferometer as represented in Fig. 7.9 and sketched in the inset of Fig. 7.11. The device is close to the ones measured experimentally, for example in [113] (although smaller owing to computational limitations) and simulated in DC in [103]. It consists of a two-dimensional gas under magnetic field with three terminals and two quantum point contacts which serve as beam splitters. This device differs from the Fabry-Perot in two ways: first it is simpler conceptually as only two paths contribute to the transport. Second, these two paths can be resolved spatially (the edge states being chiral, transmitted and reflected waves propagate on different edge states). We considered a 2 μm^2 GaAs/AlGaAs heterostructure with an electronic density of $n_s = 10^{11}$ cm^{-2}, mobility $\mu = 2 \times 10^6$ cm^2.V^{-1}.s^{-1} under a perpendicular magnetic field $B = 1.8$ T (corresponding to filling factor one, first Hall plateau). The velocity is measured to be $v = 7 \times 10^4$ m.s^{-1} with an abrupt confinement of the electrons so that the difference of time of flight between the two paths is $\tau_F = 64$ ps. Fast pulses of duration $\tau_p = 12$ ps were applied to electrode 0 to obtain the fast pulse limit. The system is modeled within the effective mass approximation in presence of a small static disorder. The Schrödinger equation is discretized on a mesh with a step $a = 3$ nm (so that 10^5 sites were used in the simulation) much smaller than both the Fermi wave length $\lambda_F = 79$ nm and magnetic length $l_B = 19$ nm of the system. The model and the in-

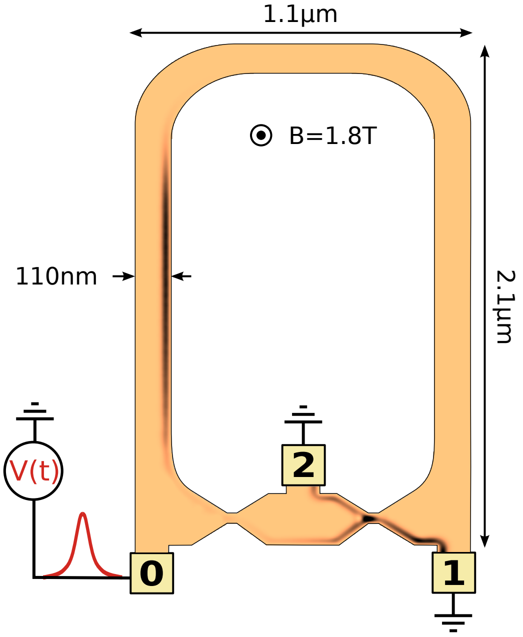

Figure 7.9 – Mach-Zehnder interferometer. Snapshot of the local electronic density at $t = 46$ ps. The color map indicates the deviation from equilibrium which goes from 0 (salmon) to 0.22×10^{11} cm^{-2} (black).

corporation of the magnetic field in the numerics are detailed in chapter 8. Fig. 7.10 shows the differential conductance dI_1/dV_0 as a function of magnetic field. We adjust the extra magnetic field to 1 mT such that the system is at(off) resonance for contact 1(2).

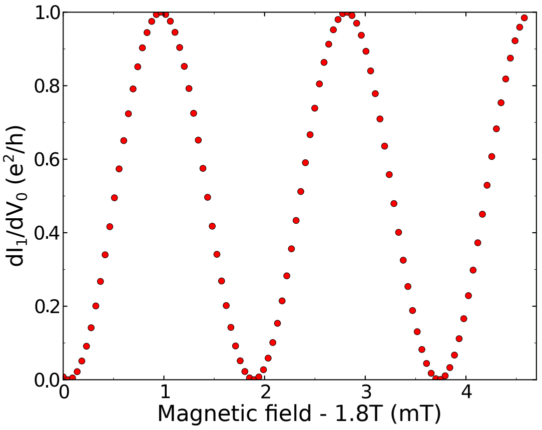

Figure 7.10 – Differential conductance dI_1/dV_0 for contact 1 in units of e^2/h as a function of magnetic field.

In the simulations, contacts 1 and 2 are grounded, while a voltage pulse is applied on contact 0 [same pulse as Eq. (7.5)]. The injected current follows

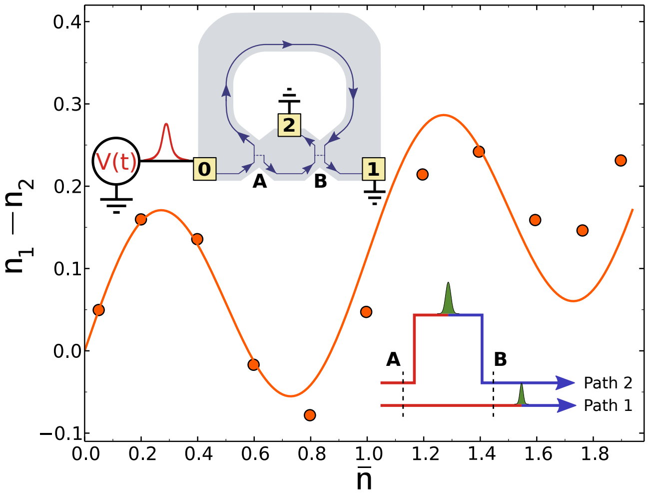

Figure 7.11 – Main figure: difference $n_1 - n_2$ between the transmitted charge into contact one and two as a function of the total injected charge $\bar{n}$. The full line corresponds to the analytical calculation $n_1 - n_2 = 0.12\bar{n} + 0.14 \sin(2\pi\bar{n})$ (see Method section). Upper inset: schematic of the system with the electron gas (light gray), the three contacts 0, 1, and 2 (yellow), the two semi-transparent quantum point contact A and B and the effective chiral edge states (blue arrows). Lower inset: schematic of the two paths which contribute to the stationary wave function. As the pulse propagates along the different trajectories, a phase difference $2\pi\bar{n}$ appears between the front (blue) and the rear (red) of the pulse.

the edge state and is split into two parts as it reaches the first quantum point contact (QPC). Both QPCs are set to be semi-transparent $D_A = D_B = 0.5$ and consequently act as beam splitters. The two parts of the initial current are recombined at the second QPC. Fig. 7.9 actually corresponds to a snapshot of the simulation at an intermediate time $t = 46$ ps. The color code indicates the deviation of the local electronic density with respect to the equilibrium value. At this intermediate time, the pulse has already passed through the first QPC and is split into two parts. The lower (transmitted) part is reaching the electrodes 1 and 2 while the upper (reflected) part is traveling along the longer arm of the interferometer.

The results of Fig. 7.11 confirm the oscillations of the transmitted charge with $\bar{n}$. The dynamical control of the phase between the two arms of the interferometer stands in this experimentally accessible geometry. Fig. 7.12(c) shows the current arriving in the electrode 1 as a function of time, in direct analogy with Fig. 7.4(b). The two peaks correspond respectively to the arrival of the pulse from the lower arm and upper arm of the interferometer while the plateau in between corresponds to the dynamical control of the interference pattern. We show for completeness the actual value of these currents at the first peak ($t = t_a$) and on the plateau ($t = t_b$) in Fig. 7.12(a) and Fig. 7.12(b) respectively. We find, as expected, that the first contribution increases with $\bar{n}$ while the latter oscillates as $\sin(2\pi\bar{n})$. The lower inset of

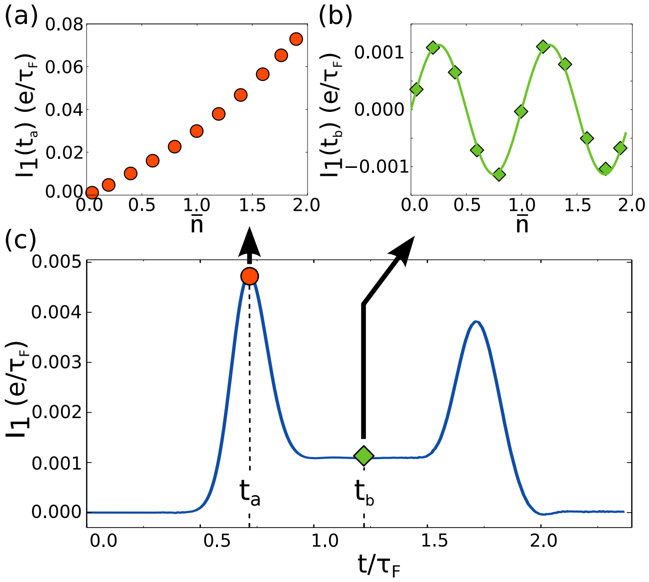

Figure 7.12 – Current I_1 at contact 1 for the Mach-Zehnder interferometer. (a,b) Amplitude of $I_1(t_a)$, $I_1(t_b)$, as a function of the number of injected particles $\bar{n}$. Symbols are numerical data. The line in (b) corresponds to $I_1(t_b) = 0.001 \sin(2\pi\bar{n})$. (c) Transmitted current $I_1(t)$ as a function of time for $\bar{n} = 0.2$.

Fig. 7.11 contains a schematic of a snapshot of the interference pattern at $t = t_b$.

The quantitative calculation of the number of transmitted particles for the Mach-Zehnder geometry proceeds along the same lines as for the Fabry-Perot case, and is even simplified by the presence of only two paths contributing to the transmission amplitude of the device. The transmission probabilities from lead 0 to 1 (2) reads,

$$|S^0_{10}(E)|^2 = D_A D_B + R_A R_B + 2\sqrt{D_A D_B R_A R_B} \cos(\phi + \tau_F(E - E_F)), \tag{7.21}$$

$$|S^0_{20}(E)|^2 = D_A R_B + R_A D_B - 2\sqrt{D_A D_B R_A R_B} \cos(\phi + \tau_F(E - E_F)), \tag{7.22}$$

with ϕ the total magnetic flux through the central depleted region (in unit of $\hbar/e$) and τ_F the extra time needed for the upper paths with respect to the lower one. After following the same steps as for the Fabry-Perot geometry, one obtains (in the limit of short pulses) the number of particles transmitted to contact 1 (2),

$$\boxed{\begin{aligned} n_1 &= (D_A D_B + R_A R_B)\bar{n} + \frac{2}{\pi}\sqrt{D_A D_B R_A R_B} \sin(\pi\bar{n}) \cos(\pi\bar{n} + \phi) \\ n_2 &= (D_A R_B + R_A D_B)\bar{n} - \frac{2}{\pi}\sqrt{D_A D_B R_A R_B} \sin(\pi\bar{n}) \cos(\pi\bar{n} + \phi) \end{aligned}} \quad \begin{aligned} (7.23) \\ (7.24) \end{aligned}$$

Fig. 7.13 shows the number of transmitted particles at contact 1 as a function of the magnetic flux ϕ for four different numbers of injected particles. We find that the numerics confirm the quantitative calculations.

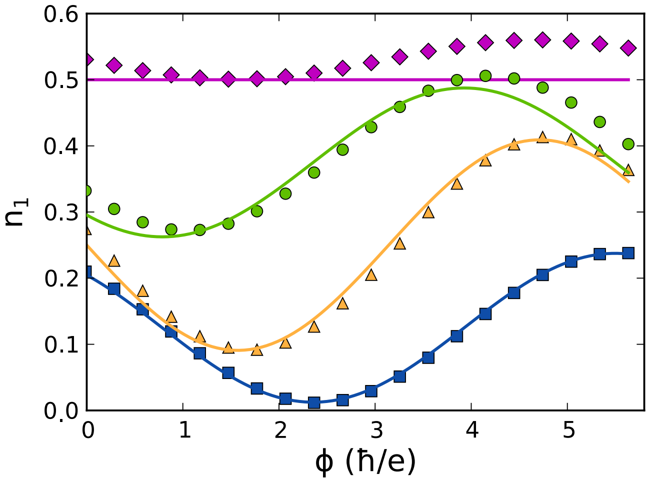

Figure 7.13 – Number of transmitted particles at contact 1 as a function of the total magnetic flux through the central depleted region. Symbols correspond to numerical data for $\bar{n} = 0.25$ (blue squares), $\bar{n} = 0.5$ (yellow triangles), $\bar{n} = 0.75$ (green circles), $\bar{n} = 1$ (magenta diamonds). Full lines correspond to the analytical result Eq. (7.23) with $D_A = D_B = 0.5$.

7.4.2 *A comment on electron-electron interactions*

A common difficulty encountered in time-dependent transport, which was pointed out by Büttiker some years ago [36], is the crucial role of electrostatics in restoring a gauge invariant, current conserving theory. Indeed, in the non-interacting theory used here, the conservation equation for the charge reads,

$$\partial_t \rho(x,t) + \partial_x I(x,t) = 0, \tag{7.25}$$

where $\rho(x,t)$ is the charge density and $I(x,t)$ the local current. In presence of time-dependent perturbations (such as the voltage pulse), the current is not conserved and a finite charge density temporarily accumulates in the system. An accumulation of charge costs however a tremendous amount of electrostatic energy so that in real systems, this charge density is screened by image charges in nearby gates. Those image charges result in a displacement current $I_d = \partial_t \rho(x,t)$ flowing in those electrodes. Only once this displacement current is taken into account does one recover current conservation. As a result of the presence of this time-dependent charge density, one should, at the mean field level include the corresponding time-dependent potential created by these charges into our time-dependent Schrödinger equation. Let us make a couple of specific remarks for the situation studied here. First, we study situations with a small number of injected particles $\bar{n}$, therefore one should be very careful with the mean field approach as one wants to avoid spurious self interacting terms present at the Hartree level. Second, all our calculations are done for a non-interacting model, and are therefore *a priori* expected to be valid in presence of metallic gates in close proximity to the quantum wire. Third, while the displacement currents and corresponding time-dependent potentials can modify the AC properties of the system, the total transmitted charge n_t shall not be affected by treating explicitly the electrostatic problem. Indeed, the total number of transmitted and reflected electrons are conserved and gauge invariant quantities (in the sense defined by Büttiker [36]) and therefore do not suffer from the flaws of their AC counterparts. In plainer words, the integral (over time) of the displacement currents as well as the corresponding time-dependent potentials is zero, therefore their presence do not modify n_t. Finally, recent experiments [42] with fast voltage pulses indicate that the non-interacting theory works remarkably well for those systems. Note that beside these aspects, the electrostatics remains crucial in the determination of the spatial profile of the voltage drop created by the voltage pulse. In order to observe the effects discussed in this chapter, one needs to be able to create spatially localized voltage drops that can subsequently propagate inside the interferometer. The corresponding condition has been discussed in section 5.5.

7.5 GENERALIZATION: THE AC JOSEPHSON EFFECT WITHOUT SUPERCONDUCTIVITY

The concept of dynamical control of interference pattern developed in the previous sections is very generic and applies beyond the physics of voltage pulses. Here we extend the concept to the raising of a DC voltage in the interferometers discussed above. We show that an oscillating signal is generated upon changing abruptly the bias voltage. The effect is analogous to the AC Josephson effect in superconductors [23]; a DC voltage bias V_b applied across a weak link between two superconductors creates an oscillating current with frequency $2eV_b/h$. The mechanism behind this effect is quite straightforward. The energy of the left superconductor is eV_b higher than the right one, so that its wave function gets an extra oscillating factor $e^{-i2eV_bt/\hbar}$. The junction produces an interference between these two wave functions, hence the oscillations.

We begin with the electronic Mach-Zehnder interferometer in the quantum Hall regime already described in the previous section and sketched in Fig. 7.14(a). At $t = 0$ one raises the bias voltage applied on contact 0 from $V(t < 0) = 0$ to $V(t > \tau_P) = V_b$. While the exact manner in which the voltage is raised is unimportant, the rise time τ_P must be sufficiently fast ($\tau_P < \tau_F$), and the voltage drop spatially sharp enough (compared to the length of the interferometer) as discussed in chapter 5. Fig. 7.14(b) shows the transmitted current $I_1(t)$ as a function of time t, and we can discern three distinct regimes. In the beginning (Fig. 7.14(a) left) the voltage bias did not have enough time to propagate up to contact 1, and $I_1(t) = 0$. During a transient regime of duration τ_F (Fig. 7.14(a) middle), the bias has arrived at contact 1 from the lower arm but not yet from the upper one. The current increases to a finite value. Finally (Fig. 7.14(a) right), the bias arrives from the upper arm and the current increases to its stationary value.

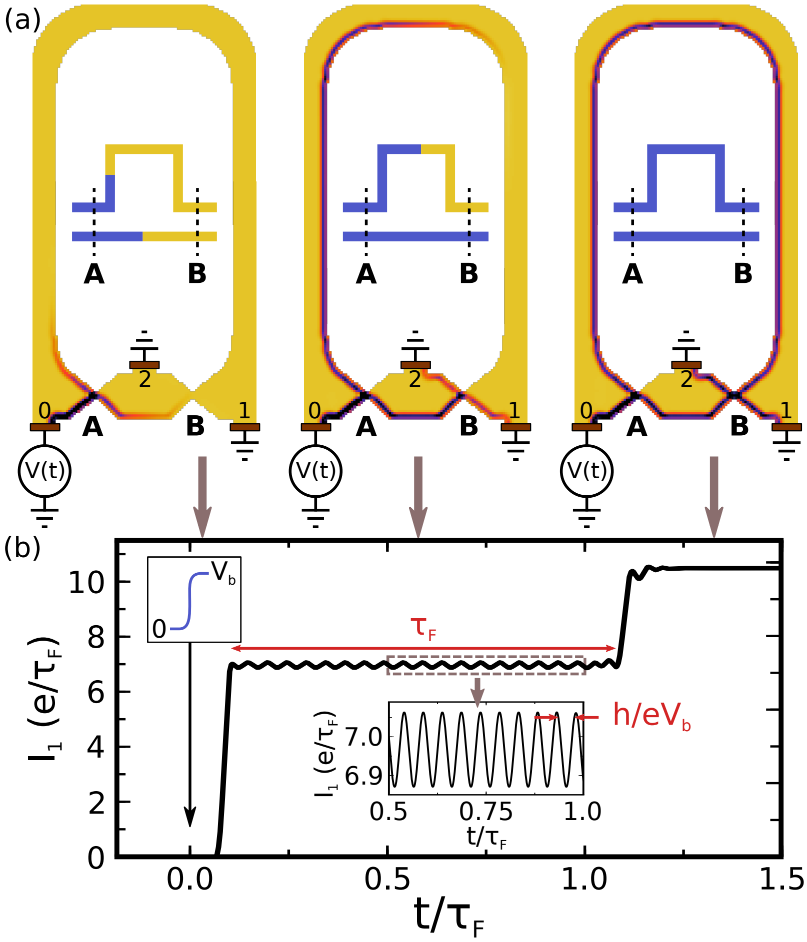

Figure 7.14 – (a) Color plot of the local electronic charge density (measured from equilibrium) in a 3 terminal Mach-Zehnder interferometer in the quantum Hall regime: from vanishing density (yellow), to 10^{11} cm^{-2} (red). At $t = 0$, the voltage bias is raised from $V(t < 0) = 0$ to $V_b = 20h/(e\tau_F)$. The three color plots correspond to three snapshots for different times as indicated by the arrows. A two-dimensional electron gas (yellow) is connected to three electrodes, the semi-transparent quantum point contacts A and B act as beamsplitters. Insets: schematics of the propagation of the voltage bias along the two arms of the interferometer. (b) Transmitted current at contact 1. Upper inset: schematic of the raising of the bias voltage. Lower inset: zoom on the oscillations of the current.

The most noteworthy feature of Fig. 7.14(b) lies in the transient regime; the current oscillates with frequency eV_b/h around a DC component. This transient oscillatory regime is the mesoscopic analogue of the AC Josephson effect. It is to the AC Josephson effect what persistent currents [2] are to supercurrents.

The theory required to obtain this transient oscillatory regime is the same as the one used in section 7.3.1. Within the time-dependent scattering approach, one finds that the wave function close to contact 0 is a plane wave that acquires an additional phase when the bias voltage is raised,

$$\Psi_0(x,t) = \frac{1}{\sqrt{k}} e^{ikx - iEt/\hbar - ieV_b t\theta(t-x/v)/\hbar} \tag{7.26}$$

where $\theta(x)$ is the Heaviside function, E is the incident energy of the electron, k the corresponding momentum, and the curved coordinate x follows the edge of the sample. We have assumed for simplicity a linear dispersion relation $E(k) = \hbar v k$ and the condition $\tau_P \ll \tau_F$. We see from Eq. (7.26) that raising the voltage induces an oscillating phase difference $e^{ieV_b t/\hbar}$ between the front and the rear of the wave. One can consider this phase difference as the time-dependent extension of the stationary case that was discussed in [40] and in the previous sections. The device uses the delay time τ_F between the two arms to create an interference between the rear and the front of the wave function, generating the oscillatory behavior. In the transient regime, the wave function close to contact 1 is the superposition of the contributions from the two paths and one finds,

$$\Psi_1(x,t) = \frac{1}{\sqrt{k}} e^{ikx - iEt/\hbar} d_1(t,E) \tag{7.27}$$

with the total time-dependent transmission amplitude $d_1(t,E)$ given by,

$$d_1(t,E) = d_u(E) e^{-iE\tau_F/\hbar} + d_l(E + eV_b) e^{-ieV_b t/\hbar}. \tag{7.28}$$

The amplitudes $d_{u/l}$ for the upper/lower arm are given in terms of the transmission (reflection) probabilities $D_{A/B}$ ($R_{A/B}$) of the quantum point contacts, $d_u = \sqrt{D_A D_B}$ and $d_l = \sqrt{R_A R_B}$. Using the time-dependent generalization of the Landauer formula Eq. 4.1 in the continuous limit,

$$I_1(t) = (e/h) \int dE |d_1(t,E)|^2 f(E) \tag{7.29}$$

[$f(E)$ is the Fermi function, Eq. (7.29) includes the equilibrium current injected from contact 0 which needs to be subtracted], we finally get the current at contact 1 during the transient regime,

$$\boxed{I_1(t) = \frac{e^2 V_b}{h} D_A D_B + \frac{e}{\pi \tau_F} \sqrt{D_A D_B R_A R_B} \cos\left(\frac{eV_b t}{\hbar} + \phi\right).} \tag{7.30}$$

Eq. (7.30) agrees with the direct microscopic numerical calculations presented above. While the precise coefficients depend on the particular interferometer considered, its structure is totally general. It contains a DC term plus an AC term at frequency eV_b/h, and the amplitude of the AC current is of the order of e/τ_F. For a typical micrometer sized Mach-Zehnder interferometer, the amplitude of the AC current is of the order of a few nA. Going back to our original Fabry-Perot device, Fig. 7.15 shows a sketch of the Fabry-Perot geometry together with a numerical calculation of the mea-

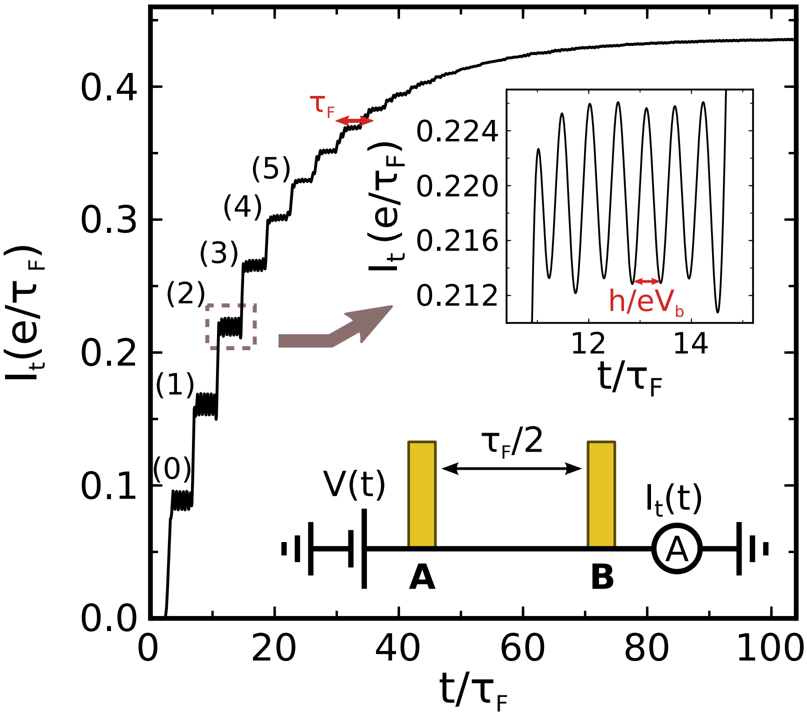

Figure 7.15 – Transmitted current (in units of e/τ_F, where τ_F is twice time of flight between the two barriers) as a function of time for a Fabry-Perot cavity. At $t = 0$, the voltage bias is raised from $V(t < 0) = 0$ to $V_b = 6h/(e\tau_F)$. Upper inset: zoom on the oscillations of the current on a plateau. Lower inset: schematic of the Fabry-Perot cavity ($D_a = D_b = 0.1$).

sured current as a function of time (τ_F is now twice the time of flight to allow for a direct comparison with the Mach-Zehnder case). The $I_t(t)$ curve now features many steps that correspond to the arrival of the path with direct transmission (0), the path with one reflection on B and A (1), two reflections (2) and so on, as discussed extensively in the previous sections. Again, each of these steps is accompanied by oscillations at the frequency eV_b/h. On decreasing the transparencies of the barriers, D_A and D_B, the Fabry-Perot resonances gradually become true bound states and the duration of the transient regime increases accordingly. This situation is very close, mathematically, to the true Andreev bound states that occur in a Josephson junction [13].

For an easier observation of the transient AC signal, it might be convenient to replace the abrupt voltage change described above by a train of square pulses (with a "slow" period $\sim \tau_F$). Such a train of pulses would stabilize the AC signal and should permit its observation with current technology. Finally, it is worth mentioning that the electrical currents calculated so far identify to the particle currents only, as we did not take the displacement currents into account. While this is important when looking for quantitative numerical values, it does not question the oscillatory behavior discussed here.

8

NUMERICAL SIMULATIONS OF TIME-RESOLVED QUANTUM TRANSPORT IN THE QUANTUM HALL EFFECT REGIME

Electronic states in the quantum Hall regime—obtained for instance by applying a strong magnetic field to a two-dimensional heterostructure—are very peculiar; with a vanishing velocity in the bulk of the system, they only propagate (in a chiral way) on the edges of the sample. Following its initial discovery some thirty years ago [114], the quantum Hall effect is now used for the metrological measurements of the quantum of conductance e^2/h [115, 116] as well as a model system for mesoscopic physics, for example electronic interferometers [16, 17, 18] such as the one simulated in chapter 3. The corresponding transport properties can be understood quantitatively using the Landauer-Büttiker scattering theory and the associated concept of one-dimensional chiral edge states [109]. These edge states can take place on the actual edges of the sample—the mesa of the two-dimensional electron gas—or can be defined by electrostatic gates put on top of the device.

In this chapter we first introduce the standard prescriptions for numerical simulations in the quantum Hall regime in section 8.1. We continue with some additional requirements for the time-dependent transport in section 8.2. These are mainly technical obstacles we dealt with during this work, and we provide our solutions. The last section is devoted to a conceptually intriguing proposal. Upon applying radio-frequency pulses on the electrostatic gates of a device, we propose to stop an electron from an initial voltage pulse (applied to an Ohmic contact) in the bulk of a two-dimensional electron gas in the quantum Hall regime. The DC numerical settings are known material, while all other sections are original work and results.

We will consider throughout this chapter a two-dimensional electron gas (2DEG) with perpendicular magnetic field $\vec{B}$. Our Hamiltonian reads,

$$\hat{\mathbf{H}}(t) = \int\int dx\, dy\, \psi^\dagger(x,y)\frac{(-i\hbar\nabla - e\vec{A})^2}{2m^*}\psi(x,y) + \epsilon(x,y,t)\psi^\dagger(x,y)\psi(x,y), \tag{8.1}$$

where the field operator $\psi(x,y)$ [$\psi^\dagger(x,y)$] destroys (creates) an electron at position (x,y), $\epsilon(x,y,t)$ is a time-dependent potential containing contributions from the mesa boundary, voltages applied at the Ohmic contacts and the electric field due to possible gates. $\vec{A} = \nabla \times \vec{B}$ is the vector potential, m^* is the effective mass of the system.

We begin with the prescriptions to perform numerical DC simulations in presence of magnetic field.

8.1.1 *Magnetic field in numerical calculations*

Let us suppose, for simplicity, that Eq. (8.1) does not contain any time-dependent potential. The discretization of the model on a square lattice with lattice parameter a yields,

$$\hat{\mathbf{H}}(t) = -\gamma \sum_{\langle i,j \rangle} e^{-i\Phi_{ij}} c_i^\dagger c_j + \sum_{i=1}^{N} V_i c_i^\dagger c_i + h.c., \tag{8.2}$$

where c_i $[c_i^\dagger]$ destroys (creates) a particle on site i, N is the number of sites inside the central region of the system, and $\langle\ \rangle$ refers to nearest neighbor coupling (with hopping amplitude $\gamma = \hbar^2/(2m^* a^2)$). The magnetic field is incorporated by means of the Peierls phase $\Phi_{ij} = e/\hbar \int_{r_j}^{r_i} \vec{A} \cdot d\vec{r}$. In the Landau gauge $\vec{A} = Bx\hat{y}$, Φ_{ij} reads,

$$\Phi_{ij} = 2\pi\Phi(n_{y_i} - n_{y_j}) \frac{n_{x_i} + n_{x_j}}{2}, \tag{8.3}$$

with $\Phi = Ba^2/\Phi_0$, where $\Phi_0 = h/e$ is the flux quantum and (n_{x_i}, n_{y_i}) is the position of site i on the lattice along x and y. Note that in the chosen gauge, only the hoppings in the y-direction are modified. More remarkable is that the Peierls phase depends on the y-coordinates of sites i and j only through their difference. This is of importance for incorporating the magnetic field into the leads. Indeed within the Landau gauge, the Hamiltonian matrix of a vertical unit cell, $H_{\bar{m}}$, as well as the coupling matrix $V_{\bar{m}}$ (both defined in section 3.2) do not depend on the layer, which allows for the calculation of self-energies with standard techniques [95].

Introducing a magnetic field into the Schrödinger equation brings new characteristic quantities to the problem. Table 8.1 relates the experimental parameters to the discretized model. We shall see in the following how to set these parameters to enter the quantum Hall effect regime. In order

Experimental parameter	Discretized model
Magnetic field B	$\Phi\Phi_0/a^2$
Cyclotron frequency $\omega_c = eB/m^*$	$4\pi\Phi\gamma/\hbar$
Magnetic length $l_B = \sqrt{\hbar/(eB)}$	$a/\sqrt{2\pi\Phi}$

Table 8.1 – Relation between experimental parameters and the discretized model ones. We chose the electronic charge $e = 1$ in the discretized model parameters.

to ease the discussion, we pose $\hbar = 1$ and use dimensionless (arbitrarily reduced) lengths such that the lattice parameter becomes $\tilde{a}$ and the magnetic length $\tilde{l}_B = 1/\sqrt{2\pi\Phi}$.

8.1.2 *DC settings for the quantum Hall effect regime*

We consider a simple quasi one-dimensional ribbon with $\tilde{a} = 1$ as a model system for this discussion, see Fig. 8.1. The magnetic field is set via the previously defined phase Φ. The color plot in Fig 8.2(a) shows the transmission of the ribbon as a function of energy and Φ. This fractal structure, so-called Hofstadter butterfly [117], is due to the magnetic length becoming smaller than the lattice constant. Indeed as we increase the magnetic field, we decrease the magnetic length. When $\Phi \geqslant 0.1$ (roughly) the discretization is too coarse with respect to the magnetic length to properly render the physical reality and one obtains numerical artifacts. Fig. 8.2(b,c) show the transmission and the band structure for an intermediate value $\Phi = 0.07$. At

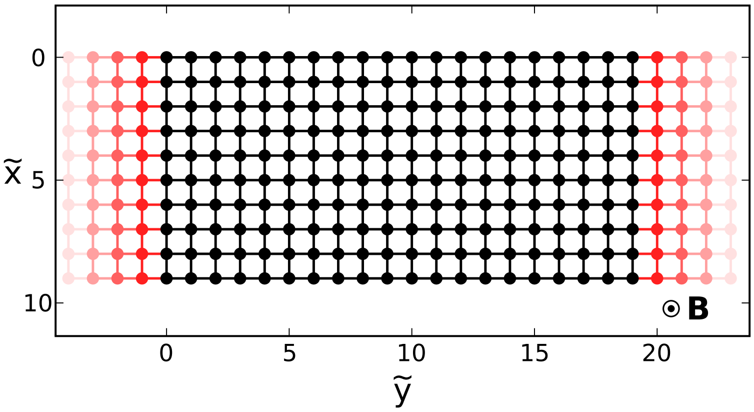

Figure 8.1 – Quasi one-dimensional system discretized with $\tilde{a} = 1$ in presence of a magnetic field B. The black dots and connections correspond to the central region, and the red ones correspond to a few layers of the semi-infinite leads.

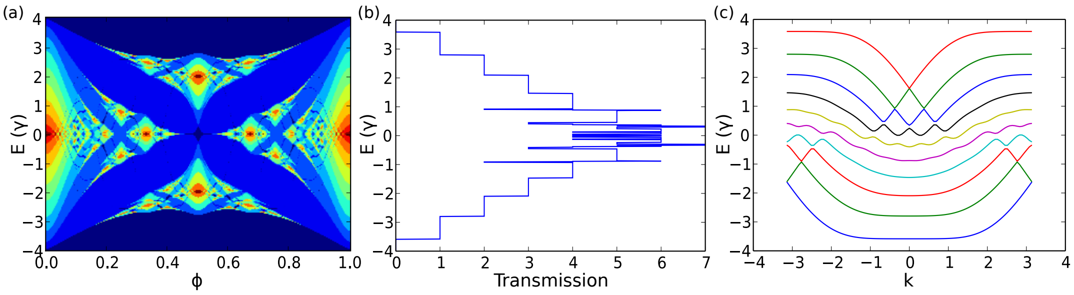

Figure 8.2 – DC characterization of a quasi one-dimensional system in presence of magnetic field. (a) Color map of the transmission as a function of the number of flux quanta Φ and energy. (b) Energy as a function of the transmission of the system. (c) Local band structure of the system. The system is discretized with $\tilde{a} = 1$. (b,c) $\Phi = 0.07$.

low energy we recover the quantization of the transmission corresponding to the opening of Landau levels in Fig. 8.2(c).The bands are flat (dispersionless) only in the middle of the system (small wave vector k). They are bended by the confining potential created by edges of the system. At higher energy finite size effects again creates spurious effects as can be seen both in the transmission and the band structure.

8.2 ADDITIONAL SETTINGS FOR TIME-DEPENDENT NUMERICS

Time-dependent numerics differs from its DC counterpart as we are now forced to integrate over a wide range of energies to compute observables (see Eq. (4.25)). In addition, time-dependent perturbations, such as voltage pulses, tend to excite energies above the Fermi level in a very badly defined manner. As transport properties may vary greatly with energy, such as velocity, spurious effects in numerical results are easily obtained.

8.2.1 *Filtering slow propagating modes*

We already addressed the integration over energy required by our wave function approach in section 5.4. The filtering procedure we came up with calls for a few comments.

- The slow modes and their effects are completely physical. The time-dependent perturbation excites all energies below the Fermi level, it is then normal to get contributions from the whole band.
- These effects disappear in the long time limit, where only the contributions close to the Fermi level remain significant.
- As opposed to real experiments, we cannot simulate this infinitely long-time limit. As a result the filtering operation is only a way to simulate the relevant part of the full physical reality.

Here we show how to engineer the spatial shape of the filtering potential in presence of magnetic field. We consider the same system as in the previous section modeled by the Hamiltonian Eq. (8.1) where we add a few layers between the left contact and the central region to apply an onsite potential that only depends on the y-coordinate. We also include a Gaussian voltage pulse, $V(t) = V_p \exp(-4\log(2)t^2/\tau_p^2)$, of amplitude $V_p = 0.05\gamma$ and duration $\tau_p = 10\gamma^{-1}$ sent through the system via the left contact. We work in a regime where only the lowest Landau levels (LLL) contribute to the transport properties. Fig. 8.3 shows the current density coming from the left contact (see sketch in Fig. 8.1). Similarly to Fig. 5.7, Fig. 8.3(a) shows that without filtering, contributions from the bottom of the band relax very slowly. However our previous filter consisting of a step potential placed after the voltage drop does not work anymore, as can be seen in Fig. 8.3(b). This is due to the high density of slow propagating states which characterizes the quantum Hall effect regime. We take this feature into account and engineer a tunneling barrier as shown in the inset of Fig. 8.3(c). The color

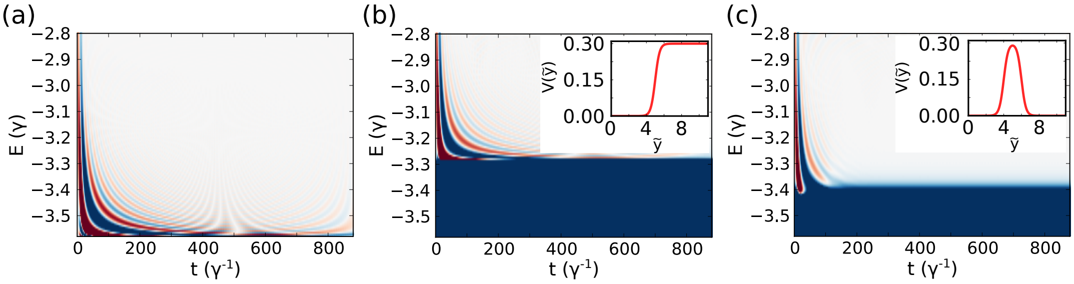

Figure 8.3 – Contribution $I(E,t)$ of the bottom lead to the current $I(t)$ as a function of time and injected energy. We inject a Gaussian pulse in the quasi 1D system, $V(t) = V_P e^{-4log(2)t^2/\tau_p^2}$, with amplitude $V_P = 0.05\gamma$ and duration $\tau_p = 10\gamma^{-1}$. Red (blue) indicates values above (below) one. (a) No filter is applied. (b) The filter is a step voltage (see inset). (c) The filter is a localized barrier (see inset).

plot of Fig. 8.3 indicates that the central region was cleared from any slow propagating states, resulting in a recovery of the numerical convergence.

8.2.2 *Dealing with abrupt geometries*

Building our time-dependent numerical scheme on top of a powerful DC package, KWANT [96], allows us to simulate two-dimensional systems of any geometry very easily. We already showed an example with the Mach-Zehnder interferometer in chapter 7. Here we show how a coarse, but acceptable (i. e. $\tilde{a} < \tilde{l}_B$), discretization can lead to unexpected numerical results by mixing the Landau levels. We consider a rectangular shaped system where half a disk was cut out as sketched in Fig. 8.4(a). Since we use a square lattice, the circling edge is rough with numerous steps as can be seen in the inset (lattice parameter $\tilde{a} = 0.5$). As previously, we initially work in a regime where only the LLL participates in the electronic transport. The color plot of Fig. 8.4(a) actually shows the electronic density $d\rho(x,y)/dV$ upon applying a DC bias voltage V at the left (inner state) or right (outer state) contact.

We set the Fermi energy (E_F) slightly below the second LL as shown in the band structure of Fig. 8.4(b), and apply a Gaussian voltage pulse, $V(t) = V_p \exp(-4\log(2)t^2/\tau_p^2)$, of amplitude $V_p = 0.12\gamma$ and duration $\tau_p = 50\gamma^{-1}$ on the left contact. Fig 8.5(a,b) show the deviation of the local electronic density from equilibrium as a function of the curved coordinate along the circle and time. We used two values of the discretization parameter, $\tilde{a} = 1$ [Fig. 8.5(a)] and $\tilde{a} = 0.5$ [Fig. 8.5(b)]. While Fig. 8.5(b) displays a seamless propagation similar to what could be obtained in a one-dimensional quantum wire, Fig. 8.5(a) exhibits chaotic features. In order to understand this behavior we need to combine both characteristics of the discretization and the voltage pulse. The numerics were obtained for a reduced magnetic length $\tilde{l}_B = 1.5$ (corresponding to $\Phi = 0.07$). It implies that $\tilde{a} = 1$ yields a crude discretization and does not allow one to separate

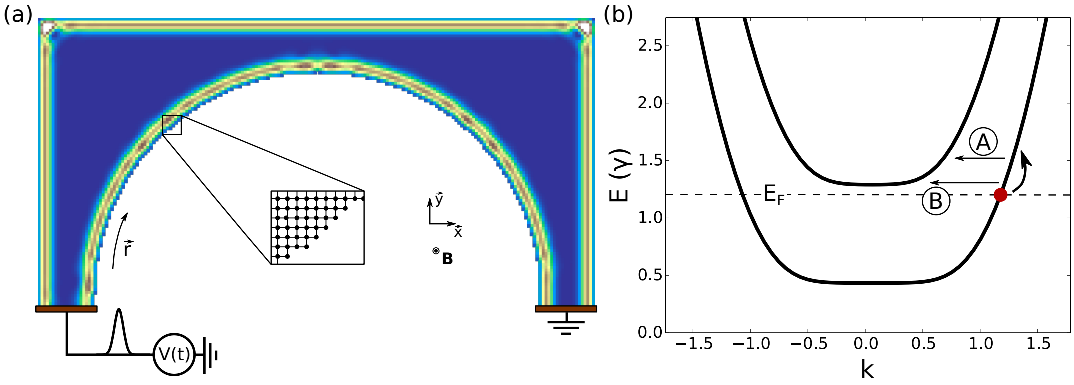

Figure 8.4 – Color map of $d\rho(x,y)/dV$ of the system showing the edge states at the Fermi level as defined by the dashed line in (b). Inset: zoom on the lattice, $\tilde{a} = 0.5$. (b) Band structure of the system. The dashed line is the Fermi level. The curved arrow starting from the state at Fermi energy (red dot) indicates the energy of particles injected in the device by means of a voltage pulse. The mixing of the Landau levels is illustrated with two cases. Case A, the particle is transfered into the second LL in a state with finite velocity. Case B, the particle ends up in a state with vanishing velocity.

properly the edge states appearing at higher energy than E_F on the circling part of the system. Since at equilibrium only one edge state is available at the Fermi energy (see the red dot in Fig. 8.4(b)), one could think that this is not an issue. This is where the voltage pulse comes into play. Its role is to transfer particles initially in the lead below E_F inside the system at energies above E_F, on an energy scale given by $\max(V_p, \hbar/\tau_p)$ as indicated by the ascending arrow in Fig. 8.4(b). The particles in the voltage pulse have now enough energy to access the second LL, which implies acquiring a different group velocity. This is illustrated by the horizontal arrows in Fig. 8.4(b). In case A, the particle ends up in a state with a lower, but finite, velocity. This is the origin of the second branch that grows around the curved coordinate $r = 20$ in Fig. 8.5(a). In case B, the particle is transfered in a dispersionless state (bottom of the second LL). This gives rise to the exotic charge fluctuations shown in Fig. 8.5(a), and makes numerical convergence difficult. This result is similar to what we obtained earlier when applying a voltage pulse without filtering the slow propagating modes. The difference is that these modes are now populated by the pulse propagation inside the system.

The mixing of Landau levels arises in our example only because of a bad discretization (no disorder in our model). In order to remedy this issue it appears obvious that one should use a smaller discretization with respect to the magnetic length, as shown in Fig. 8.5(b). However this can lead to a significant increase in the number of sites in the system (halve the lattice parameter amounts to quadruple the number of sites), and eventually limit our ability to simulate realistic devices. Another route can be followed when considering the physics one wants to model. Indeed if one is only interested in the physics of the LLL, one should use voltages variations much

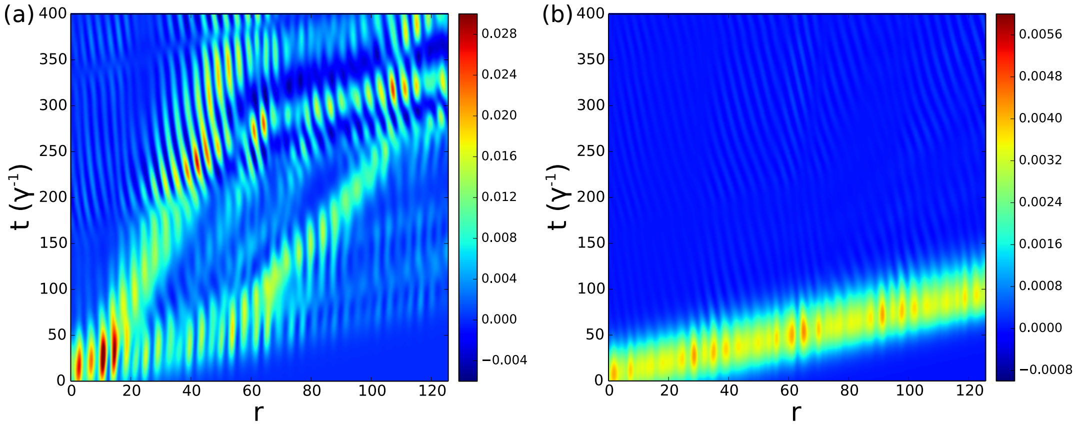

Figure 8.5 – Deviation of the local electronic charge from equilibrium as a function of the curved coordinate $\vec{r}$ along the inner circle of the system and time, for a Gaussian voltage pulse of amplitude $V_p = 0.12\gamma$ and duration $\tau_p = 50\gamma^{-1}$. Square lattice parameter: (a) $\tilde{a} = 1$, (b) $\tilde{a} = 0.5$.

smaller than the cyclotron frequency ($\max(V_p, \hbar/\tau_p) \ll \omega_c$ for a voltage pulse) to avoid any spurious cross-talk. It is worth mentioning though, that it does not prevent one to have $\tilde{a} < \tilde{l}_B$.

We now turn to a concrete example of time-resolved simulation that goes beyond the technical requirements exposed so far.

8.3 RADIO-FREQUENCY (RF) PROTOCOL FOR STOPPING VOLTAGE PULSES

The field effect obtained by applying voltages on electrostatic gates put on top of a device is very peculiar. Not only does it allow one to close or open conducting paths (as in conventional field effect transistors), but it also modifies the actual paths taken by the electrons or even partitions the edge states into the superposition of two paths [16, 17].

Here we discuss a possibility allowed by the flexibility of the edge state in the quantum Hall regime, namely the dynamical manipulation of the path taken by the electron, using fast RF modification of the gate voltages. The system is probed by sending charge pulses from an Ohmic contact. We will show that these charge pulses can be dynamically manipulated with the help of the gate voltages; they can be stopped, stored and their trajectories switched dynamically.

8.3.1 *Mechanism for stopping single electron pulses*

We start with defining our "stopping" protocol and the associated physical mechanism. Fig. 8.6(a,b) shows the first (simulated) sample that we consider. Our usual 2DEG under high magnetic field is connected to two Ohmic contacts. We work again in a regime where only the LLL contribute to the transport properties. As we concluded from the previous section, it imposes that all variations of voltages are slow compared to the cyclotron

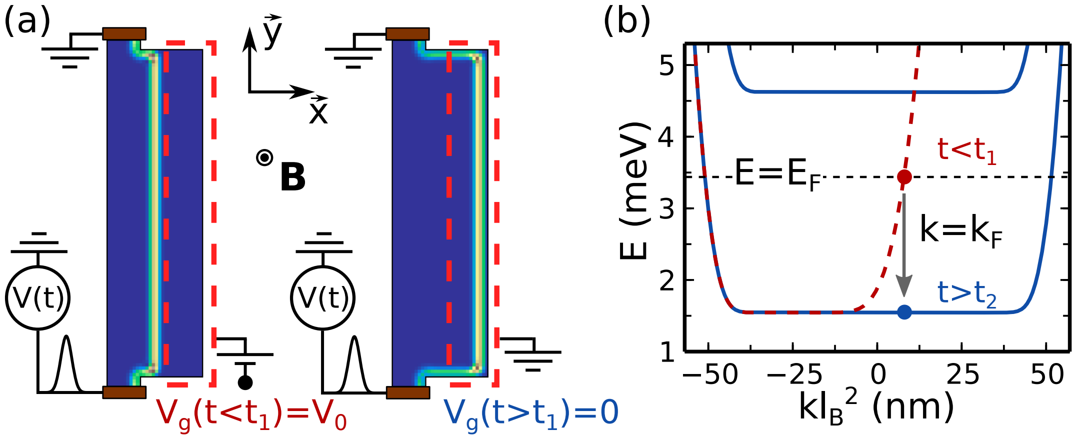

Figure 8.6 – (a) Color maps of $d\rho(x,y)/dV$ of the system indicating the position of the edge states at the Fermi level. A gate voltage V_g is applied to the electrostatic gate (red dashed rectangle) and allows one to shift the position of the edge states: $V_g = V_0$ (left), $V_g = 0$ (right). (b) Band structure of the system with polarized gate ($V_g = V_0$: dashed red) and with grounded gate ($V_g = 0$: blue line). The times t_1 and t_2 refer to the stopping protocol described in Fig. 8.7

frequency. The upper contact is grounded while the lower one is used to send voltage pulses through the system. A side gate, capacitively coupled to the right-hand side of the system (dashed line) allows one to modify the propagating edge states. When the gate voltage $V_g = V_0$ the current propagates through the middle of the sample [Fig. 8.6(a) left] while when the gate is grounded, the current propagates on the right edge of the sample [Fig. 8.6(a) right]. Fig. 8.6(a,b) are not simple schematics of the edge states but correspond to the extra electronic density $d\rho(x,y)/dV$ that appears in the 2DEG on imposing a DC bias voltage V at the lower contact.

The upper part of Fig. 8.7(a) shows our "stopping" protocol. At time $t = 0$ we send a voltage pulse $V(t)$ through the lower contact in presence of a gate voltage $V_g = V_0$ [Fig. 8.6(a)]. We wait until the pulse has propagated up to (roughly) one third of the sample and at time t_1 we start decreasing the gate voltage V_g. At time t_2, $V_g = 0$ and the gate is grounded [Fig. 8.6(b)]. The snapshots in Fig. 8.7(a) show that this protocol actually stops the propagation of the pulse which stays frozen in the system for $t > t_2$. The mechanism behind this behavior can be easily understood from an analysis of the eigenstates of the system. We model our system with the Hamiltonian Eq. (8.1). In the absence of RF pulses, and assuming that our system is invariant by translation along the y-direction (which it is except close to the contacts but this is irrelevant), the LLL [that diagonalize Eq. (8.1)] are localized along the x-direction and the plane waves along the y-direction read,

$$\Psi_k(x,y) = e^{-(x-kl_B^2)^2/2l_B^2}\, e^{iky}. \tag{8.4}$$

Fig. 8.6(b) shows the, numerically calculated, dispersion relations for $V_g = V_0$ (dashed red) and $V_g = 0$ (blue). In the absence of confining potential, the LLL are degenerate with an energy $E(k) = E_0$ (central part of the LLL

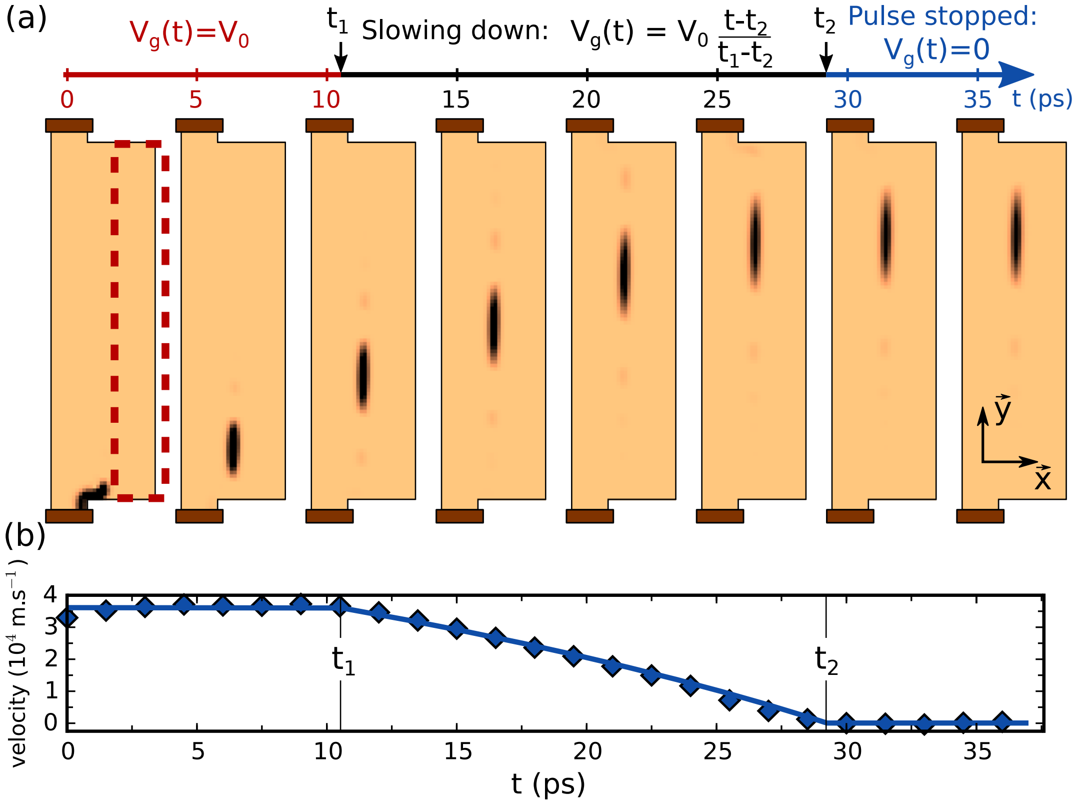

Figure 8.7 – (a) Color map of the charge density at various times during the "stopping" protocol. The gate is polarized for $t < t_1$, and slowly grounded between t_1 and t_2. At t_2 the pulse is stopped. (b) Velocity $v(t)$ of the pulse as a function of time. Diamonds correspond to numerical data, the full line to the analytical result.

in Fig. 8.6(b)). Consequently they are dispersionless with vanishing velocity as $v_k = (1/\hbar)\partial E/\partial k$. The presence of a confining potential $V(x)$ breaks this degeneracy (bending of the bands in Fig. 8.6(b)). Assuming for the sake of the argument that $V(x)$ is smooth on the scale of l_B, then the LLL remain eigenstates of the Hamiltonian in presence of the confining potential and their energy is simply raised by the value of $V(x)$ at the center of the state, $E(k) = E_0 + V(kl_B^2)$. The corresponding LLL are propagating on the edges.

Let us now go back to the "stopping" protocol. After we have sent the voltage pulse ($0 < t < t_1$), the system is in a superposition of LLL with energies close to the Fermi energy E_F (we use $V(t) \ll E_F$), $\Psi(t) = \sum_k a_k \Psi_k e^{-iE(k)t}$. At $t > t_1$, we start changing the gate voltage V_g. Although $V(x,t)$ now depends on time, we should bear in mind that the system remains invariant by translation along the y-direction at all times. As a result the momentum k is a good quantum number and the linear superposition of LLL is unmodified. The dispersion relation is now time-dependent with $E(k,t) = E_0 + V(kl_B^2, t)$ and the wave function reads, $\Psi(t) = \sum_k a_k \Psi_k e^{-i\int_0^t du E(k,u)}$. In other words, the energy decreases at fixed momentum k, as indicated by the arrow in Fig. 8.6(b). In particular the velocity of the pulse,

$$v(t) = \frac{1}{\hbar} \frac{\partial E(k,t)}{\partial k}\bigg|_{k_F}, \tag{8.5}$$

decreases until it vanishes at $t = t_2$ where the pulse stops. This argument does not depend on the speed at which the gate voltage is varied as long as it is fast enough for the pulse not to escape the gated region before the velocity vanishes. The quantum Hall effect therefore gives us a way to modify the dispersion relation dynamically and trap particles in a region of vanishing velocity.

8.3.2 *Numerical results*

We turn to direct numerical simulations of our RF protocol in order to check the above argument. Equation (8.1) is discretized on a square lattice according to the prescriptions of the above sections with a lattice parameter $a = 13$ nm. We consider a 2DEG made out of a GaAs/AlGaAs heterostructure with density $n_s = 10^{11}$ cm^{-2}, corresponding to a Fermi energy $E_F = 3.47$ meV or equivalently to a Fermi wave length $\lambda_F = 79$ nm. A magnetic field $B = 1.8$ T is applied to the system yielding a magnetic length $l_B = 19$ nm and a cyclotron frequency $\hbar\omega_c = 3.1$ meV (same set of parameters used for the Mach-Zehnder interferometer of section 7.4). We used a realistic confining potential for the gate that corresponds to a drift velocity $v = 5 \times 10^4$ m.s^{-1} but we did not actually solve the associated electrostatics. In Fig. 8.7(a), a Gaussian pulse $V(t) = V_p \exp(-4\log(2)t^2/\tau_p^2)$ of duration $\tau_p = 2$ ps and amplitude $V_P = 0.4$ mV is sent through the system. Fig. 8.7(a) actually shows the difference between two simulations performed with and without the voltage pulse. Indeed, upon decreasing V_g, the system relaxes to a new equilibrium (with electrons entering the system in order to fill the formerly forbidden region). We discuss this aspect briefly towards the end of the chapter. As expected, we find that the pulse is indeed stopped for $t > t_2$. More importantly, Fig. 8.7(b) shows a quantitative agreement between the numerics and the analysis made above. The symbols show the velocity of the pulse as measured from the time-dependent numerics (by looking at the time evolution of the center of mass of the electronic density carried by the pulse) while the line corresponds to Eq. (8.5).

Now that we have established the mechanism for stopping the pulse, we proceed with a slightly different sample with 4 terminals and an additional top gate, see Fig. 8.8. The first part of the protocol of Fig. 8.8 is the same as previously. We sent a pulse at $t = 0$ (now the pulse is sent from the lower left contact and the left gate is polarized) and stop it by gradually grounding the left gate between t_1 and t_2. For $t_2 < t < t_3$ the voltage pulse is stuck in the middle of the sample. After waiting for some time, until t_3, we do one of two things. Either we increase again the voltage of the left gate (upper panels) in order to restart the pulse, or we increase the

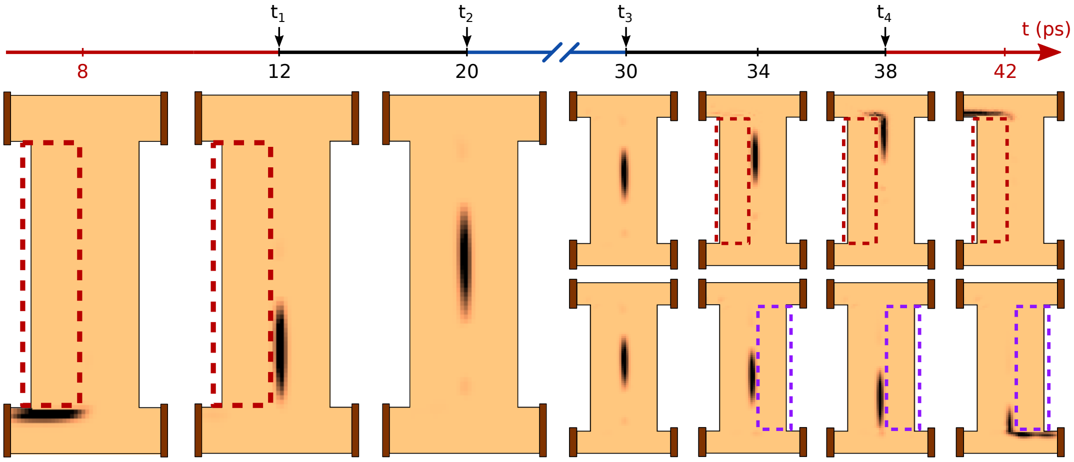

Figure 8.8 – Charge density color map for the "stop and release" protocol. The two gates on each side of the system (red/blue dashed rectangles) control the edge states (hence the direction of propagation of the pulse). The left gate is polarized for $t \leq t_1$ and grounded for $t \geq t_2$. At t_2, the pulse is frozen. At $t = t_3$ one of the two gates is polarized again, which releases the pulse. Top: the left gate is polarized, the pulse follows its original edge state and is collected in the top left electrode. Bottom: the right gate is polarized, the pulse follows the right hand side edge state and is collected in the bottom right electrode.

voltage of the other (right) gate (lower panels) which also restarts the pulse but in a different direction. From a theoretical point of view, both cases are very similar and are essentially the counter-part of the stopping protocol (and can be analyzed accordingly). However, in practice they illustrate the versatility of what could be accomplished with this dynamical modification of the paths of the electrons. This RF protocol allows one to stop a charge pulse, then store it for a while in a region with vanishing velocity, and finally release it in a direction of our choice.

8.3.3 *Mach-Zehnder analysis of the voltage pulse*

We now turn to an analysis of the nature of the "stop and release" protocol. In the sample sketched in Fig. 8.9(a), we send a voltage pulse, stop it with a gate (as previously), wait for some time τ_w, and release the pulse (again, as previously). However, instead of directly collecting the current in the electrode, it is sent through the electronic Mach-Zehnder interferometer already used in section 7.4. Fig. 8.9(b) shows the difference between the total number of electrons collected at electrodes 1 (n_1) and 2 (n_2) as a function of the waiting time τ_w. The result is at first sight rather intriguing, $n_1 - n_2$ oscillates with τ_w as $\cos((E_F - E_0)\tau_w)$. To understand this behavior, one needs to remember that a voltage pulse is not simply a localized charge pulse propagating in vacuum, indeed a delocalized plane wave (LLL) $\Psi \propto e^{iky-iEt}$ already exists before the pulse is sent. As one raises the bias voltage $V(t)$, the part of the wave at higher voltage starts accumu-

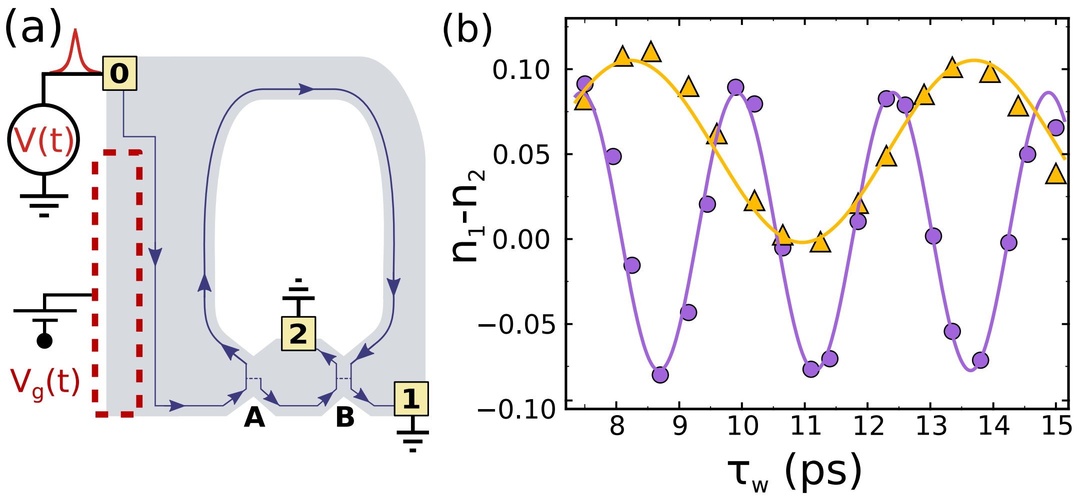

Figure 8.9 – (a) Schematic of a Mach-Zehnder interferometer with a "stop and release" gate. The blue line shows the two paths of the interferometer. (b) Difference $n_1 - n_2$ between the transmitted charges into contacts 1 and 2 as a function of the waiting time of the pulse τ_w for $E_F = 3.47$ meV (purple circles) and $E_F = 2.5$ meV (yellow triangles). Lines correspond to the fit $n_1 - n_2 = a_1 + a_2 \sin^2([(E_F - E_0)/2]\tau_w)$.

lating an extra phase $\phi(t) = \int^t du\ eV(u)/\hbar$. Noting that $\phi(\infty) = 2\pi\bar{n}$ ($\bar{n}$: number of injected particles) and supposing the voltage drop to be concentrated around $y = 0$, the wave function just after the pulse takes the form $\Psi \propto e^{iky - i2\pi\bar{n}\theta(-y)}$ where $\theta(y)$ is the Heaviside function. The kink in the phase of the wave function and the associated propagating phase domain wall were extensively discussed in chapter 7. The $2\pi\bar{n}$ phase difference between the front and the rear of the pulse causes oscillations of $n_1 - n_2$ with $\bar{n}$ owing to the "dynamical control of interference pattern". We now come back to our "stop and release" protocol (ignoring the presence of the voltage pulse). We suppose that the part of the edge state which is affected by the gate corresponds to $y \in [0, L]$ (using curved coordinates that follow the edge state). Before t_1, we have a plane wave $\Psi \propto e^{iky - iEt}$. After t_2, the inner part for $y \in [0, L]$ oscillates as $e^{iky - iE_0 t}$ while the rest of the wave, unaffected by the gate, still oscillates as $e^{iky - iEt}$ as sketched in Fig. 8.10. Therefore, after the waiting time τ_w, a phase difference $2\pi\bar{n}_w = (E - E_0)\tau_w$ has been accumulated between the inner part and the outer one. When one releases the pulse again at time t_3, the wave function reads $\Psi \propto e^{iky + i2\pi\bar{n}_w \theta(y)\theta(L-y)}$. In other words, the "stop and release" procedure is equivalent to introducing two voltage pulses in series separated by a distance L, one effective pulse of $\bar{n}_w$ electrons followed by a counter-pulse of $-\bar{n}_w$ electrons. The oscillation shown in Fig. 8.9(b) simply follows from the dynamical control of interference pattern of chapter 7 applied to this series of two pulses.

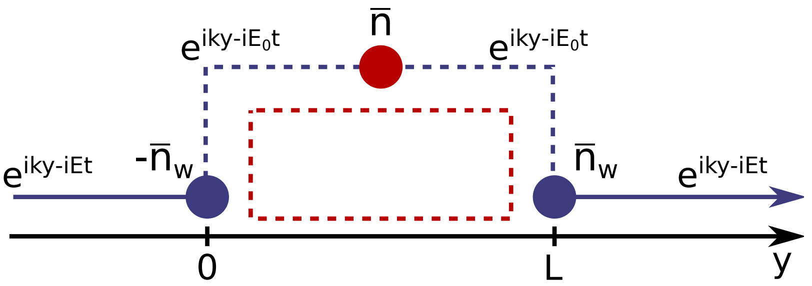

Figure 8.10 – Wave function of the system for $t_2 < t < t_3$. The (full and dashed) blue line shows the edge state and the red dashed rectangle is the top gate. The red dot corresponds to the voltage pulse containing $\bar{n}$ particles, and the blue dots correspond to the effective pulses created by the stopping protocol and containing $\bar{n}_w = (E_F - E_0)\tau_w/(2\pi)$ particles.

8.3.4 *Effect of the disorder on the "stop and release" protocol*

We present some additional data on the effect of static disorder on the "stop and release" protocol described above. In the presence of a disorder potential, the bulk states of the LLL are no longer dispersionless but form localized states whose typical extension is the correlation length of the disorder potential. The argument given for the mechanism of the "stop and release" protocol (the energy decreases at fixed momentum k) applies equally well to these localized states with one difference. After being "stopped", the voltage pulse will locally follow the small circular trajectories defined by the equi-potential of the disorder potential (instead of being fully frozen). Fig. 8.11 shows the same "stop and release" protocol as Fig. 8.8 in presence of a finite disorder (modeled by a white random potential) corresponding to a mobility $\mu = 3 \times 10^6$ cm^2.V^{-1}.s^{-1} (a typical value for a high mobility GaAs/GaAlAs heterostructure). One finds that the "stop and release" protocol works as discussed above. The efficiency of the protocol is 100% for the stopping part and 80% for the releasing part (i.e. only 80% of what is injected eventually arrives at the expected contact) which we attribute to the fact that the localized states only partially overlap with the region underneath the gate and partly with the rest of the sample that is not covered by the gate. When the releasing RF pulse is applied, it weakly affects the charge that has spread in the uncovered region.

Fig. 8.12 shows the total efficiency of the protocol as a function of the mobility. Except for the very disordered case where even the DC quantum Hall effect is affected by disorder (for the rather small sample used in the simulations), the stopping protocol always works. The releasing part is more sensitive to disorder. For mobilities above 10×10^6 cm^2.V^{-1}.s^{-1}, disorder plays no role, while 3×10^6 cm^2.V^{-1}.s^{-1} is enough for the protocol to work with good probability. Below 10^6 cm^2.V^{-1}.s^{-1}, the 2DEG is not clean enough for the procedure to be operational. Let us recall that the current state of the art for high mobility two-dimensional electron gas lies

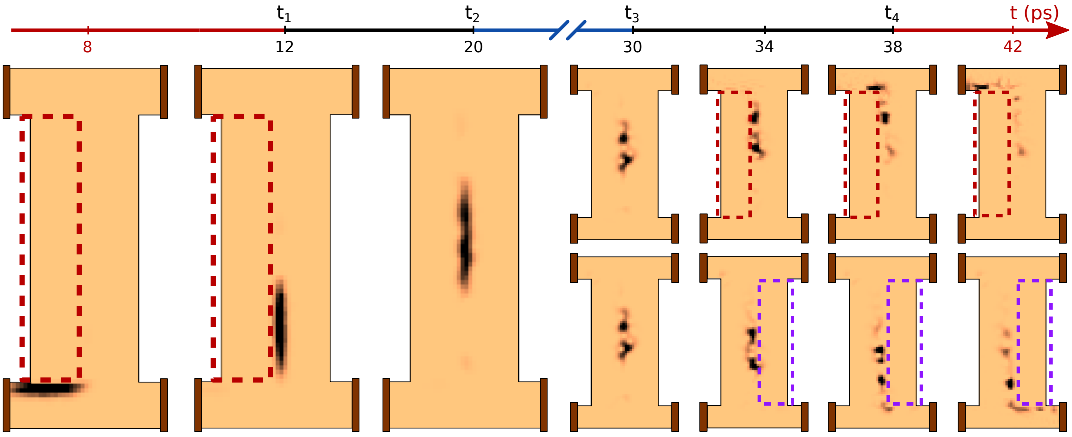

Figure 8.11 – Stop and release protocol in presence of disorder. The setting is identical to Fig. 8.8 of the main manuscript except that a white disorder was added corresponding to a finite mobility of 3×10^6 cm^2.V^{-1}.s^{-1}

around 30×10^6 cm^2.V^{-1}.s^{-1} while the value 3×10^6 cm^2.V^{-1}.s^{-1} is rather common [118].

8.3.5 *A comment on charge relaxation*

We now discuss what happens in the "stopping" protocol when one does not send any voltage pulse in the system. Unfortunately we shall not enter into any detail of the relaxation of the charge below the gate as our model is not adapted to its description. We suppose, for the sake of the argument, that the gate is grounded very abruptly ($t_2 = t_1$). Just after t_2 the former edge state is frozen as discussed extensively above. On the other hand, a new one (which was at very high energy before t_2) now appears on the edge of the mesa. This edge state is initially empty and gets gradually filled as electrons pour in from the electrode. In our non-interacting model, only the propagating modes get filled in, leaving an empty puddle in the region of the 2DEG where the velocity vanishes (most of the area under the gate). This is of course unphysical as it raises the electrostatic energy of the system. As the new edge state is filled, the corresponding charges create a local electric field; the neighboring edge states become dispersive, and start to get filled as well. This process continues until all the LLL below the gate are filled and the system has relaxed to its equilibrium. This relaxation process should be very slow as the whole area underneath the gate needs to be filled while the electrons can only be poured in through one-dimensional edge states. A proper treatment of this physics would require solving the Poisson equation self-consistently with quantum mechanics. It would allow one to describe the charge relaxation using the compressible and incompressible regions discussed in [119]. We expect however that the (current carrying) compressible stripes behave essentially in the same way as the edge states of the non-interacting theory used in this thesis. Combining a Poisson equation solver with our wave function approach is the next step

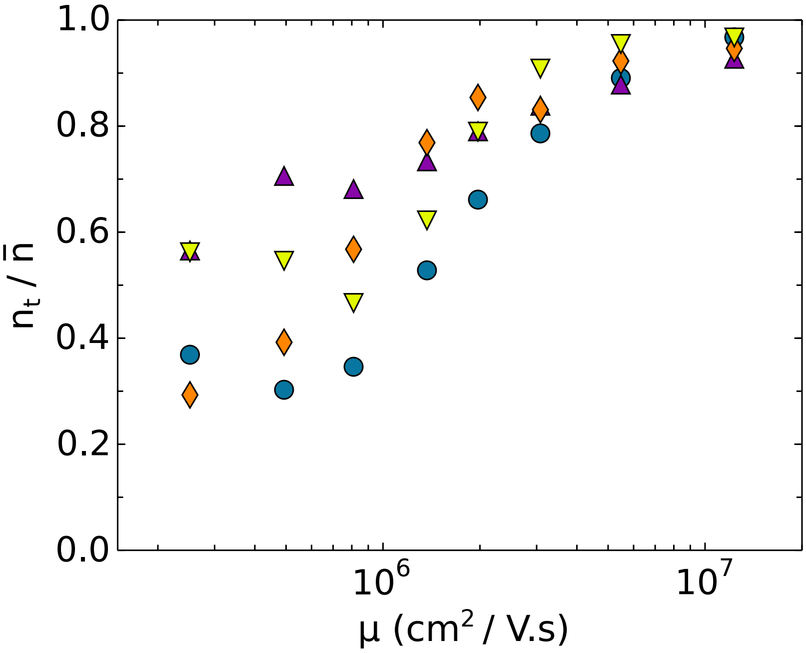

Figure 8.12 – Efficiency of the "stop and release" protocol as a function of the strength of the disorder. The plot shows $n_t/\bar{n}$ (the number of transmitted particles n_t in the top left contact divided by the number of injected particles $\bar{n}$ in the lower left contact) as a function of the mobility μ. Different symbols correspond to different disorder configurations.

beyond this thesis work to simulate these phenomena. In any case, performing the difference between two simulations (with and without charge pulse) allows us to disentangle the pulse physics (of interest here) from the charge relaxation (poorly described by our model). A similar protocol should be followed experimentally.

Similarly to the dynamical control of interference of chapter 7, the practical implementation of the proposals presented here imply delicate experiments where one injects high frequency pulses in a dilution fridge setup. The measurement scheme however should not be too difficult as, by periodically repeating the pulse sequences, measuring the number of electrons received in one electrode amounts to measuring DC currents.

Part IV

GENERAL CONCLUSION

9

CONCLUSION (ENGLISH)

High frequency experiments that are starting to be realized at low temperature and the possibility to manipulate single electron states are the motivations of this work. The objectives were to establish a theoretical framework capable of describing these experiments and to propose new concepts. At the end of these pages we can appraise our contribution to time-dependent quantum transport at different levels: formalism, numerical algorithm, experimental concepts.

Let us start with the foundation of it all, the *mathematical framework*. We began this work like everyone else did before us in this field, i. e. fighting with the NEGF formalism. It is only after we rewrote the main Green's functions in terms of a more tractable wave function that we were able to advance our understanding of the whole problem. The energy–time representation of our wave function approach seems now natural to describe the time-dependent transport. Upon applying a time-dependent perturbation to a system, one searches for its effects *in time* on the propagating states taken at an initial energy E. The choice of these original states is only a matter of boundary conditions. For instance, in the scattering theory one fixes spatial boundary conditions valid at all times, while in the partition-free approach one specifies an initial condition at time $t < 0$ in the entire system. Our final contribution related to the formalism focused on voltage pulses in multiterminal systems. We generalized the Landauer-Büttiker formula to the number of particles transmitted between the contacts. We showed that the latter quantity was particularly relevant in time-dependent quantum transport as it is conserved and gauge invariant.

Based on our formalism we made progress on the *numerical aspects* of time-dependent quantum transport. We started with an integro-differential equation (Retarded Green's function) and a double integral (Lesser Green's function) on matrices, and ended up with a simple differential equation and a single integral over energy for wave functions. The best algorithm we proposed scales now linearly with the simulated time and the volume of the system. Because of this breakthrough we were able to simulate a system with 10^5 sites, which is *a thousand times better than the state of the art*. This is where we actually benefited from the KWANT software package developed in the lab. Building our wave function approach on top of a readily usable and powerful DC code saved us an incredible amount of time.

Combining our analytical and numerical work we investigated the physics of voltage pulses in various situations going beyond the seminal work of Levitov *et al.* [110, 40, 41]. We first investigated the propagation and spreading of a charge pulse. On the one hand, we found that the propagation of a pulse is accompanied by oscillations that spread diffusively; on the other hand the envelope of the charge pulse spreads linearly with time. While we understood that a pulse generates excitations with energies of the order of $max(V_p, \hbar/\tau_p)$, we distinguished between a classical and a quantum spreading. We then focused on the quantum regime in systems possessing a characteristic time scale smaller than the Fermi energy (or the bandwidth of the model). We found that a voltage pulse should be thought of as a *phase domain wall* propagating ballistically and modifying the phase of the stationary states already present in the system. The *dynamical modification of interference* was first shown for voltage pulses in a Fabry-Perot cavity as well as in a Mach-Zehnder interferometer. The concept was further generalized to the raising of a DC bias in the aforementioned interferometers. We found that upon raising a voltage bias to a finite value V_b, there exists a universal transient regime where the current oscillates at frequency eV_b/h in analogy to the AC Josephson effect. It is worth noticing that the control of interference shown here is very generic and could be applied to Andreev resonant states which form on the boundary of superconductors, or to the oscillatory magnetic exchange interaction in magnetic multilayers. Finally, we used the quantum Hall regime to manipulate single electrons in a conceptually new approach. By using time-dependent gate voltages, we proposed to *stop, store and release a charge pulse*.

Fast quantum electronics is still an emerging field experimentally and, one might even say, theoretically. We have shown very intriguing and, in some extent, counter intuitive effects even in the simplest system. This gives a glimpse of the conceptually new physics that is about to emerge. We shall now end this manuscript with some perspectives of future work. In the light of our understanding of voltage pulses, we may consider calculating the noise associated with their excitations. In particular, we could come back to the noiseless property of excitations created by a Lorentzian voltage pulse [40, 42]. What does make these pulses so special? What would be the result of a slower pulse? Is it even related to the speed of the pulse? Our numerical approach together with analytical calculations might help answering these questions. A second perspective is to improve our numerical simulations where the Hamiltonian would depend on some arbitrary operator in addition of the usual time as $\hat{\mathbf{H}}(t, \hat{\mathbf{O}}(t))$. This allows us to incorporate electron–electron interactions at the mean field level (solving the Poisson equation and our wave function self-consistently). It might seem as a wishful thinking only designed to please the referees of our publications. However it would open the way to a wealth of new simulations like electron–electron collision, and Coulomb drag to name a few.

10

CONCLUSION (FRANÇAIS)

Des expériences à hautes fréquences commencent à être réalisées à basse température. Ces travaux sont motivés par la possibilité de manipuler des électrons uniques. Les objectifs de ce travail de thèse étaient d'établir un cadre pour traiter ces expériences et proposer de nouveaux concepts. Au bout de ces pages nous pouvons évaluer notre contribution au transport quantique dépendent du temps suivant différents aspects : le formalisme, les algorithmes numériques, les concepts expérimentaux.

Commençons par la base la plus essentielle, le *formalisme mathématique*. Nous avons débuté ce travail comme de nombreux autres thésards avant nous dans ce domaine, c'est-à-dire en se battant avec le formalisme NEGF. Ce n'est qu'après avoir réécrit les fonctions de Green principales en termes d'une fonction d'onde bien plus maniable, que nous avons pu faire avancer notre compréhension du problème dans sa globalité. La représentation énergie–temps de notre approche semble maintenant naturelle pour décrire le transport dépendent du temps. Dorénavant lorsqu'on applique une perturbation dépendente du temps à un système, on cherche ses effets *en temps* sur les états pris à l'énergie E qui se propagent. De plus, nous avons vu que le choix de ces états initiaux n'est qu'une question de conditions de bord. Par exemple, dans la théorie de scattering on fixe des conditions au bord dans l'espace et valables à tout temps, alors que dans l'approche dite "partition-free" on spécifie une condition initiale pour $t < 0$ pour l'ensemble du système. Notre contribution finale au formalisme porte sur les pulses de tension dans des systèmes multiterminaux. Nous avons généralisé la formule de Landauer pour le nombre de particules transmises entre les contacts. Nous avons montré que cette quantité est particulièrement pertinente dans le cadre du transport dépendent du temps de par sa conservation et son invariance de jauge.

En s'appuyant sur notre formalisme nous avons fait progresser les *aspects numériques* du transport dépendent du temps. Nous sommes partis d'une équation intégro-différentielle (fonction de Green Retardée) et d'une double intégrale (fonction de Green Lesser), pour arriver à une simple équation différentielle et une intégrale sur l'énergie pour des fonctions d'onde. Notre meilleur algorithme peut maintenant être amélioré pour donner un temps de calcul évoluant linéairement avec le temps simulé et le volume du système. Grâce à ce progrès nous avons simulé un système contenant plus de 10^5 sites, ce qui est *1000 fois mieux que l'état de l'art*. C'est ici que nous avons bénéficié du programme KWANT développé au laboratoire. Développer notre approche par fonction d'onde au-dessus d'un code DC puissant et prêt à l'emploi a été une source de gain de temps considérable.

En combinant nos méthodes analytiques et numériques, nous avons ensuite étudié la physique des pulses de tension dans des situations diverses au-delà des travaux fondateurs de Levitov *et al.* [110, 40, 41]. Nous avons d'abord étudié la propagation et l'étalement à une dimension d'un pulse de charges. Nous avons trouvé que la propagation du pulse est accompagnée d'oscillations de la densité de charge et du courant qui s'étalent de façon diffusive. Puis dans un deuxième temps nous avons remarqué que l'enveloppe de la densité de charge s'étale linéairement avec le temps. Nous avons alors trouvé que ce dernier étalement se composait de deux régimes, classique et quantique, séparés par le nombre de particules contenues dans le pulse de tension initial. Nous nous sommes ensuite concentrés sur le régime quantique (nombre de particules injectées de l'ordre de un) dans des systèmes possédant un temps caractéristique plus petit que l'énergie de Fermi (ou que la bande passante du modèle). Nous avons compris qu'un pulse de tension devait être vu comme une *paroi de domaine de phase* qui se propage ballistiquement et modifie localement la phase des états stationnaires déjà présents dans le système. La *modification dynamique du motif d'interférence* a d'abord été montrée dans une cavité Fabry-Perot puis dans un interféromètre de Mach-Zehnder. Nous avons enuite généralisé le concept à la montée d'une tension DC dans les interféromètres cités. Nous avons trouvé que monter une tension continue V_b donnait lieu à un régime transitoire universel où le courant oscille à la fréquence eV_b/h en complète analogie avec l'effet Josephson AC. Il est à noter que le contrôle d'interférence présenté ici est très générique et pourrait s'appliquer aux états d'Andreev résonants qui se forment à l'interface de jonctions supraconductrices, ou encore à l'interaction d'échange dans des multicouches magnétiques. Enfin, nous avons utilisé l'effet Hall quantique pour manipuler des électrons dans une approche conceptuellement nouvelle. En utilisant des tensions de grille dépendentes du temps, nous avons proposé de *stopper, stocker et relâcher* un pulse de charge.

L'électronique quantique rapide est toujours un domaine naissant expérimentallement et, dans une certaine mesure, aussi du point de vu théorique. Nous avons donné des résultats souvent intrigants, et parfois contre intuitifs même dans le cas de systèmes simples. Cela donne donc un aperçu de la physique nouvelle qui est en train d'émerger. Nous terminons avec quelques perspectives. A la lumière de notre compréhension des pulses de tension, on peut maintenant considérer calculer le bruit associé aux excitations qu'ils créent. En particulier, on pourrait revenir aux propriétés spéciales prêtées aux pulses Lorentziens [40, 42]. Que rend ces pulses si spéciaux ? Que donnerait un pulse plus lent ? L'absence d'excitation de trou est-elle liée à la vitesse de montée du pulse ? Notre combinaison de méthodes analytiques et numériques semble aujourd'hui bien adaptée pour traiter ce problème. Une seconde perspective est d'améliorer notre outil de simulation numérique pour traiter un Hamiltonien dépendent d'une observable $\hat{\mathbf{H}}(t, \hat{\mathbf{O}}(t))$. Cela permettrait d'incorporer les interactions électrons–électrons au niveau du champ moyen (en résolvant l'équation de Poisson de façon auto-consistente). On pourrait croire ici à un voeu pieux n'ayant pour but que de satisfaire les referees de nos publications. Cependant une telle implémentation ouvrirait la voie à de nouvelles simulations telles que les collisions électrons–électrons ou le Coulomb drag.

Part V

APPENDIX

A

DYSON EQUATION FOR THE RETARDED AND LESSER GREEN'S FUNCTIONS

We provide here the derivation of the Dyson equation for the Retarded (Eq. (3.17)) and Lesser (Eq. (3.21)) Green's functions. For more clarity we introduce a compact notation for the convolution product. Be A and B two time-dependent functions, the convolution product C reads,

$$C(t,t') = \int du A(t,u)B(u,t') = A * B \tag{A.1}$$

We start from the Dyson equation of the Green's function matrix $\hat{G}$, Eq. (3.16),

$$\hat{G}(t,t') = \hat{g} + \int du\ \hat{g}(t,u)\mathbf{H}^{'}(u)\sigma_z\hat{G}(u,t'). \tag{A.2}$$

The diagonal and off-diagonal parts respectively yields,

$$\mathcal{G}^{<} + \mathcal{G}^{R} = g^{<} + g^{R} + (g^{<} + g^{R}) * \mathbf{H}^{'} * (\mathcal{G}^{<} + \mathcal{G}^{R}) - g^{<} * \mathbf{H}^{'} * \mathcal{G}^{>} \tag{A.3}$$

$$\mathcal{G}^{<} = g^{<} + g^{R} * \mathbf{H}^{'} * \mathcal{G}^{<} + g^{<} * \mathbf{H}^{'} * \mathcal{G}^{A} \tag{A.4}$$

where $\mathcal{G}^{A}(t,t') = [\mathcal{G}^{R}(t',t)]^{\dagger}$ is the Advanced Green's function. We dropped the time arguments for convenience and we will continue to do so unless there is any ambiguity. We shall now focus on the Dyson equations for the projections of the Green's functions on the central region G^{R} and $G^{<}$.

Subtracting Eq. (A.3) and Eq. (A.4), we obtain,

$$\mathcal{G}^{R} = g^{R} + g^{R} * \mathbf{H}^{'} * \mathcal{G}^{R} + g^{<} * \mathbf{H}^{'} * \left([\mathcal{G}^{R} - \mathcal{G}^{A}] - [\mathcal{G}^{>} - \mathcal{G}^{<}]\right) \tag{A.5}$$

which reduces to

$$\mathcal{G}^{R} = g^{R} + g^{R} * \mathbf{H}^{'} * \mathcal{G}^{R}, \tag{A.6}$$

upon using the identity $[\mathcal{G}^{R} - \mathcal{G}^{A}] = [\mathcal{G}^{>} - \mathcal{G}^{<}]$ resulting from the definitions of all the Green's functions aforementioned. Eq. (A.6) is the Dyson equation for the Retarded Green's function of the whole system (central region and leads). Projecting this result on the central region $\bar{0}$ yields,

$$\mathcal{G}^{R}_{\bar{0}\bar{0}} = g^{R}_{\bar{0}} + g^{R}_{\bar{0}} * \mathbf{H}^{'}_{\bar{0}\bar{0}} * \mathcal{G}^{R}_{\bar{0}\bar{0}} + \sum_{\bar{m}=1}^{\bar{M}} g^{R}_{\bar{0}} * \mathbf{H}^{'}_{\bar{0}\bar{m}} * \mathcal{G}^{R}_{\bar{m}\bar{0}}, \tag{A.7}$$

with

$$\mathcal{G}^{R}_{\bar{m}\bar{0}} = g^{R}_{\bar{m}} * \mathbf{H}^{'}_{\bar{m}\bar{0}} * \mathcal{G}^{R}_{\bar{0}\bar{0}}. \tag{A.8}$$

Subtituting $\mathcal{G}^R_{\bar{m}\bar{0}}$ in Eq. (A.7) by Eq. (A.8) yields,

$$\mathcal{G}^R_{\bar{0}\bar{0}} = g^R_{\bar{0}} + g^R_{\bar{0}} * \left[\mathbf{H}'_{\bar{0}\bar{0}} + \sum_{\bar{m}=1}^{\bar{M}} \mathbf{H}'_{\bar{0}\bar{m}} * g^R_{\bar{m}} * \mathbf{H}'_{\bar{m}\bar{0}} \right] * \mathcal{G}^R_{\bar{0}\bar{0}}, \tag{A.9}$$

where we identify the Retarded self-energy in the second term of the bracket. A more compact form reads,

$$G^R = g^R_{\bar{0}} + g^R_{\bar{0}} * \left[\mathbf{H}'_{\bar{0}\bar{0}} + \Sigma^R \right] * G^R, \tag{A.10}$$

which concludes the derivation of Eq. (3.17).

Following the exact same steps for the derivation of Eq. (A.4) yields,

$$G^< = g^<_{\bar{0}} + g^R_{\bar{0}} * \left[\mathbf{H}'_{\bar{0}\bar{0}} + \Sigma^R \right] * G^< + g^R_{\bar{0}} * \Sigma^< * G^A + g^<_{\bar{0}} * \left[\mathbf{H}'_{\bar{0}\bar{0}} + \Sigma^A \right] * G^A \tag{A.11}$$

We apply $[i\partial_t - \mathrm{H}^0_{\bar{0}\bar{0}}]$ on the left side of Eq. (A.11) and obtain,

$$\left[i\partial_t - \mathrm{H}^0_{\bar{0}\bar{0}} - \mathrm{H}'_{\bar{0}\bar{0}} - \Sigma^R \right] * G^< = \Sigma^< * G^A, \tag{A.12}$$

where we used the identities,

$$i\partial_t g^R_{\bar{0}}(t,t') - \mathrm{H}^0_{\bar{0}\bar{0}} g^R_{\bar{0}}(t,t') = \delta(t-t') \tag{A.13}$$

$$i\partial_t g^<_{\bar{0}}(t,t') - \mathrm{H}^0_{\bar{0}\bar{0}} g^<_{\bar{0}}(t,t') = 0 \tag{A.14}$$

as can be shown from the definitions of $g^R_{\bar{0}}$ and $g^<_{\bar{0}}$. Now inserting the equation of motion for G^R (Eq. (3.20)) as an additional convolution product to the right-hand side of Eq. (A.12). We finally obtain the Dyson equation for the Lesser Green's function on the central region $\bar{0}$

$$G^< = G^R * \Sigma^< * G^A. \tag{A.15}$$

B

VARIOUS ANALYTICAL RESULTS FOR GREEN'S FUNCTIONS OF THE 1D CHAIN

We gather here a few analytical results for the 1d chain that were used to benchmark the numerical results shown in this thesis. Given an analytic function f our convention for Fourier transforms is

$$f(t) = \int \frac{dE}{2\pi} f(E) e^{-iEt} \tag{B.1}$$

$$f(E) = \int dt\, f(t) e^{iEt} \tag{B.2}$$

The expressions below correspond to the Hamiltonian Eq. (5.1) for the perfect one dimensional chain ($\epsilon_i = 0$). The Lesser Green's functions were computed at zero temperature with $E_F = 0$. Energies are written in units of the hopping parameter γ, and times are in units of γ^{-1}.

We begin with self-energies in energy for a semi-infinite lead,

$$\Sigma^R(E) = \begin{cases} \frac{E}{2} - i\sqrt{1-(\frac{E}{2})^2} & \text{if } |E| \leq 2 \\ \frac{E}{2} - \sqrt{(\frac{E}{2})^2 - 1} & \text{if } E > 2 \\ \frac{E}{2} + \sqrt{(\frac{E}{2})^2 - 1} & \text{if } E < -2 \end{cases} \tag{B.3}$$

$$\Sigma^<(E) = \begin{cases} 2i\sqrt{1-(\frac{E}{2})^2} & \text{if } -2 \leq E \leq E_F \\ 0 & \text{else} \end{cases} \tag{B.4}$$

The corresponding Fourier transforms in time yields,

$$\Sigma^R(t) = -i\frac{J_1(2t)}{t}\theta(t) \tag{B.5}$$

$$\Sigma^<(t) = i\frac{J_1(2t)}{2t} - \frac{H_1(2t)}{2t} \tag{B.6}$$

where J_n is the Bessel function of the first kind, and H_n is the Struve function of order n.

We also computed Green's functions for the infinite 1D chain at equilibrium. The diagonal elements of the Retarded and Lesser Green's functions in energy read,

$$G^R_{xx}(E) = \begin{cases} \frac{1}{2i\sqrt{1-(\frac{E}{2})^2}} & \text{if } |E| \leq 2 \\ \frac{1}{2\sqrt{(\frac{E}{2})^2-1}} & \text{if } E > 2 \\ \frac{1}{-2\sqrt{(\frac{E}{2})^2-1}} & \text{if } E < -2 \end{cases} \tag{B.7}$$

$$G^<_{xx}(E) = \begin{cases} \frac{i}{\sqrt{1-(\frac{E}{2})^2}} & \text{if } -2 \leq E \leq E_F \\ 0 & \text{else} \end{cases} \tag{B.8}$$

and their counterparts in the time domain,

$$G^R_{xx}(t) = -iJ_0(2t)\theta(t) \tag{B.9}$$

$$G^<_{xx}(t) = \frac{i}{2}J_0(2t) - \frac{H_0(2t)}{2} \tag{B.10}$$

The off diagonal element $G^<_{x,x+1}$ in energy and time domains read,

$$G^<_{x,x+1}(E) = \begin{cases} \frac{iE/2}{\sqrt{1-(\frac{E}{2})^2}} & \text{if } -2 \le E \le E_F \\ 0 & \text{else} \end{cases} \tag{B.11}$$

$$G^<_{x,x+1}(t) = \frac{J_1(2t)}{2} - \frac{i}{2}H_{-1}(2t). \tag{B.12}$$

BIBLIOGRAPHY

[1] Y. Imry. The physics of mesoscopic systems. In G. Grinstein and G. Mazenko, editors, *Directions in Condensed Matter Physics*. World Scientific Press, 1986.

[2] Y. Imry. *Introduction to mesoscopic physics*. Oxford University Press, second edition, 2002.

[3] L. Saminadayar, C. Bäuerle, and D. Mailly. Equilibrium properties of mesoscopic quantum conductors. In H.S. Nalwa, editor, *Encyclopedia of Nanoscience and Nanotechnology*, volume 3, pages 267–285. American Scientific Publishers, 2004.

[4] C. Kittel. *Introduction to Solid State Physics*. Wiley, 6th edition, 1986.

[5] B. T. Matthias, T. H. Geballe, and V. B. Compton. Superconductivity. *Rev. Mod. Phys.*, 35:1–22, 1963.

[6] C. W. J. Beenakker and H. van Houten. Quantum transport in semiconductor nanostructures. In Henry Ehrenreich and David Turnbull, editors, *Semiconductor Heterostructures and Nanostructures*, volume 44 of *Solid State Physics*, pages 1 – 228. Academic Press, 1991.

[7] E. Akkermans and G. Montambaux. *Mesoscopic Physics of Electrons and Photons*. Cambridge University Press, 2007.

[8] Y. Aharonov and D. Bohm. Significance of Electromagnetic Potentials in the Quantum Theory. *Phys. Rev.*, 115:485–491, 1959.

[9] R. A. Webb, S. Washburn, C. P. Umbach, and R. B. Laibowitz. Observation of he Aharonov-Bohm Oscillations in Normal-Metal Rings. *Phys. Rev. Lett.*, 54:2696–2699, 1985.

[10] M. Yamamoto, S. Takada, C. Bauerle, K. Watanabe, A. Wieck, and S. Tarucha. Electrical control of a solid-state flying qubit. *Nature Nanotechnology*, 7:247, 2012.

[11] W. Liang, M. Bockrath, D. Bozovic, J. H. Hafner, M. Tinkham, and H. Park. Fabry - Perot interference in a nanotube electron waveguide. *Nature*, 411:665–669, 2001.

[12] L. G. Herrmann, T. Delattre, P. Morfin, J.-M. Berroir, B. Plaçais, D. C. Glattli, and T. Kontos. Shot Noise in Fabry-Perot Interferometers Based on Carbon Nanotubes. *Phys. Rev. Lett.*, 99:156804, 2007.

[13] C. W. J. Beenakker and H. van Houten. Josephson current through a superconducting quantum point contact shorter than the coherence length. *Phys. Rev. Lett.*, 66:3056–3059, 1991.

[14] A. V. Kretinin, R. Popovitz-Biro, D. Mahalu, and H. Shtrikman. Multimode Fabry-Perot Conductance Oscillations in Suspended Stacking-Faults-Free InAs Nanowires. *Nano Letters*, 10:3439, 2010.

[15] J. P. Bird, K. Ishibashi, M. Stopa, Y. Aoyagi, and T. Sugano. Coulomb blockade of the Aharonov-Bohm effect in GaAs/$Al_xGa_{1-x}As$ quantum dots. *Phys. Rev. B*, 50:14983–14990, 1994.

[16] Y. Ji, Y. Chung, D. Sprinzak, M. Heiblum, D. Mahalu, and H. Shtrikman. An electronic Mach-Zehnder interferometer. *Nature*, 422(6930):415–418, 2003.

[17] P. Roulleau, F. Portier, P. Roche, A. Cavanna, G. Faini, U. Gennser, and D. Mailly. Direct Measurement of the Coherence Length of Edge States in the Integer Quantum Hall Regime. *Phys. Rev. Lett.*, 100:126802, 2008.

[18] G. Haack, M. Moskalets, J. Splettstoesser, and M. Büttiker. Coherence of single-electron sources from Mach-Zehnder interferometry. *Phys. Rev. B*, 84:081303, 2011.

[19] P. K. Tien and J. P. Gordon. Multiphoton process observed in the interaction of microwave fields with the tunneling between superconductor films. *Phys. Rev.*, 129:647–651, 1963.

[20] Y. V. Nazarov and Y. M. Blanter. *Quantum Transport: Introduction to Nanoscience*. Cambridge University Press, 2009.

[21] L.-H. Reydellet, P. Roche, D. C. Glattli, B. Etienne, and Y. Jin. Quantum partition noise of photon-created electron-hole pairs. *Phys. Rev. Lett.*, 90:176803, 2003.

[22] A. A. Clerk, M. H. Devoret, S. M. Girvin, F. Marquardt, and R. J. Schoelkopf. Introduction to quantum noise, measurement, and amplification. *Rev. Mod. Phys.*, 82:1155–1208, 2010.

[23] B. D. Josephson. Possible new effects in superconductive tunnelling. *Physics Letters*, 1(7):251 – 253, 1962.

[24] K. K. Likharev. *Dynamics of Josephson Junctions and Circuits*. Gordon and Breach, New York, 1986.

[25] P. W. Brouwer. Scattering approach to parametric pumping. *Phys. Rev. B*, 58:R10135–R10138, 1998.

[26] F. Zhou, B. Spivak, and B. Altshuler. Mesoscopic Mechanism of Adiabatic Charge Transport. *Phys. Rev. Lett.*, 82:608–611, 1999.

[27] H. Pothier, P. Lafarge, C. Urbina, D. Esteve, and M. H. Devoret. Single-electron pump based on charging effects. *Europhys. Lett.*, 17:249–254, 1992.

[28] F. Giazotto, P. Spathis, S. Roddaro, S. Biswas, F. Taddei, M. Governale, and L. Sorba. A josephson quantum electron pump. *Nat. Phys.*, 7:857–861, 2011.

[29] J. Gabelli, G. Fève, T. Kontos, J.-M. Berroir, B. Placais, D. C. Glattli, B. Etienne, Y. Jin, and M. Büttiker. Relaxation Time of a Chiral Quantum *R-L* Circuit. *Phys. Rev. Lett.*, 98:166806, 2007.

[30] E. Zakka-Bajjani, J. Ségala, F. Portier, P. Roche, D. C. Glattli, A. Cavanna, and Y. Jin. Experimental test of the high-frequency quantum shot noise theory in a quantum point contact. *Phys. Rev. Lett.*, 99:236803, 2007.

[31] E. Zakka-Bajjani, J. Dufouleur, N. Coulombel, P. Roche, D. C. Glattli, and F. Portier. Experimental determination of the statistics of photons emitted by a tunnel junction. *Phys. Rev. Lett.*, 104:206802, 2010.

[32] J. Gabelli and B. Reulet. Shaping a time-dependent excitation to minimize the shot noise in a tunnel junction. *Phys. Rev. B*, 87:075403, 2013.

[33] M. Büttiker, H. Thomas, and A. Prêtre. Mesoscopic capacitors. *Physics Letters A*, 180(4–5):364 – 369, 1993.

[34] M. Büttiker, A. Prêtre, and H. Thomas. Admittance of small conductors. *Phys. Rev. Lett.*, 71:465–465, 1993.

[35] M. Büttiker. Capacitance, admittance, and rectification properties of small conductors. *Journal of Physics: Condensed Matter*, 5(50):9361, 1993.

[36] M. Büttiker, A. Prêtre, and H. Thomas. Dynamic conductance and the scattering matrix of small conductors. *Phys. Rev. Lett.*, 70:4114–4117, 1993.

[37] M. Büttiker. Time-dependent current partition in mesoscopic conductors. *Il Nuovo Cimento*, 110B:509–522, 1995.

[38] M. V. Moskalets. *Scattering matrix approach to non-stationary quantum transport*. Imperial College Press, London, 2012.

[39] O. Shevtsov and X. Waintal. Numerical toolkit for electronic quantum transport at finite frequency. *Phys. Rev. B*, 87:085304, 2013.

[40] L. S. Levitov, H. Lee, and G. B. Lesovik. Electron counting statistics and coherent states of electric current. *Journal of Mathematical Physics*, 37:4845, 1996.

[41] J. Keeling, I. Klich, and L. S. Levitov. Minimal excitation states of electrons in one-dimensional wires. *Phys. Rev. Lett.*, 97:116403, 2006.

[42] J. Dubois, T. Jullien, F. Portier, P. Roche, A. Cavanna, Y. Jin, W. Wegscheider, P. Roulleau, and D. C. Glattli. Minimal-excitation states for electron quantum optics using levitons. *Nature*, 502:659 – 663, 2013.

[43] J. Dubois, T. Jullien, C. Grenier, P. Degiovanni, P. Roulleau, and D. C. Glattli. Integer and fractional charge lorentzian voltage pulses analyzed in the framework of photon-assisted shot noise. *Phys. Rev. B*, 88:085301, 2013.

[44] G. Fève, A. Mahé, J.-M. Berroir, T. Kontos, B. Plaçais, D. C. Glattli, A. Cavanna, B. Etienne, and Y. Jin. An on-demand coherent single-electron source. *Science*, 316:1169, 2007.

[45] A. Mahé, F. D. Parmentier, E. Bocquillon, J.-M. Berroir, D. C. Glattli, T. Kontos, B. Plaçais, G. Fève, A. Cavanna, and Y. Jin. Current correlations of an on-demand single-electron emitter. *Phys. Rev. B*, 82:201309, 2010.

[46] F. D. Parmentier, E. Bocquillon, J.-M. Berroir, D. C. Glattli, B. Plaçais, G. Fève, M. Albert, C. Flindt, and M. Büttiker. Current noise spectrum of a single-particle emitter: Theory and experiment. *Phys. Rev. B*, 85:165438, 2012.

[47] Y. Sherkunov, N. d'Ambrumenil, P. Samuelsson, and M. Büttiker. Optimal pumping of orbital entanglement with single-particle emitters. *Phys. Rev. B*, 85:081108, 2012.

[48] C. Grenier, R. Hervé, G. Fève, and P. Degiovanni. Electron Quantum Optics In Quantum Hall Edge Channels. *Modern Physics Letters B*, 25(12n13):1053–1073, 2011.

[49] E. Bocquillon, F. D. Parmentier, C. Grenier, J.-M. Berroir, P. Degiovanni, D. C. Glattli, B. Plaçais, A. Cavanna, Y. Jin, and G. Fève. Electron quantum optics: Partitioning electrons one by one. *Phys. Rev. Lett.*, 108:196803, 2012.

[50] E. Bocquillon, V. Freulon, J.-M Berroir, P. Degiovanni, B. Plaçais, A. Cavanna, Y. Jin, and G. Fève. Coherence and indistinguishability of single electrons emitted by independent sources. *Science*, 339(6123):1054–1057, 2013.

[51] J. D. Fletcher, P. See, H. Howe, M. Pepper, S. P. Giblin, J. P. Griffiths, G. A. C. Jones, I. Farrer, D. A. Ritchie, T. J. B. M. Janssen, and M. Kataoka. Clock-controlled emission of single-electron wave packets in a solid-state circuit. *Phys. Rev. Lett.*, 111:216807, 2013.

[52] S. Hermelin, S. Takada, M. Yamamoto, S. Tarucha, A. D. Wieck, L. Saminadayar, C. Bauerle, and T. Meunier. Electrons surfing on a sound wave as a platform for quantum optics with flying electrons. *Nature*, 477:435, 2011.

[53] R. P. G. McNeil, M. Kataoka, C. J. B. Ford, C. H. W. Barnes, D. Anderson, G. A. C. Jones, I. Farrer, and D. A. Ritchie. On-demand single-electron transfer between distant quantum dots. *Nature*, 477:439, 2011.

[54] Z. Zhong, N. M. Gabor, J. E. Sharping, A. Gaetal, and P. L. McEuen. Terahertz time-domain measurement of ballistic electron resonance in a single-walled carbon nanotube. *Nature Nanotechnology*, 3:201, 2008.

[55] D. P. DiVincenzo. Quantum computation. *Science*, 270(5234):255–261, 1995.

[56] B. M. Terhal, M. M. Wolf, and A. C. Doherty. Quantum Entanglement: A Modern Perspective. *Phys. Today*, 56:46, 2003.

[57] C. W. J. Beenakker, C. Emary, M. Kindermann, and J. L. van Velsen. Proposal for Production and Detection of Entangled Electron-Hole Pairs in a Degenerate Electron Gas. *Phys. Rev. Lett.*, 91:147901, 2003.

[58] M. D. Barrett, J. Chiaverini, T. Schaetz, J. Britton, W. M. Itano, J. D. Jost, E. Knill, C. Langer, D. Leibfried, R. Ozeri, and D. J. Wineland. Deterministic quantum teleportation of atomic qubits. *Nature*, 429:737–739, 2004.

[59] Nielsen M. A. and I. L. Chuang. *Quantum Computation and Quantum Information*. Cambridge University Press, 2000.

[60] J. Rammer and H. Smith. Quantum field-theoretical methods in transport theory of metals. *Rev. Mod. Phys.*, 58:323, 1986.

[61] J. Rammer. *Quantum field theory of non-equilibrium states*. Cambridge Univ. Press, 2007.

[62] M. Cini. Time-dependent approach to electron transport through junctions: General theory and simple applications. *Phys. Rev. B*, 22:5887–5899, 1980.

[63] S. Kurth, G. Stefanucci, A. Almbladh, C.-O. Rubio, and E. K. U. Gross. Time-dependent quantum transport: A practical scheme using density functional theory. *Physical Review B*, 72:035038, 2005.

[64] G. E. Kimball and G. H. Shortley. The Numerical Solution of Schrödinger's Equation. *Phys. Rev.*, 45:815–820, 1934.

[65] C. Caroli, R. Combescot, P. Nozieres, and D. Saint-James. Direct calculation of the tunneling current. *J. Phys. C*, 4:916, 1971.

[66] L. V. Keldysh. Diagram technique for non-equilibrium processes. *Sov. Phys. JETP*, 20:1018, 1965.

[67] H. M. Pastawski. Classical and quantum transport from generalized Landauer-Büttiker equations. II. Time-dependent resonant tunneling. *Phys. Rev. B*, 46:4053–4070, 1992.

[68] C. Caroli, R. Combescot, P. Nozieres, and D. Sain-James. A direct calculation of the tunnelling current: IV. Electron-phonon interaction effects. *Journal of Physics C: Solid State Physics*, 5(1):21, 1972.

[69] T. E. Feuchtwang. Tunneling theory without the transfer Hamiltonian formalism. V. A theory of inelastic-electron-tunneling spectroscopy. *Phys. Rev. B*, 20:430–445, 1979.

[70] N. S. Wingreen, A.-P. Jauho, and Y. Meir. Time-dependent transport through a mesoscopic structure. *Phys. Rev. B*, 48:8487, 1993.

[71] A.-P. Jauho, N. S. Wingreen, and Y. Meir. Time-dependent transport in interacting and noninteracting resonant-tunneling systems. *Phys. Rev. B*, 50:5528, 1994.

[72] Y. Meir and N. S. Wingreen. Landauer formula for the current through an interacting electron region. *Phys. Rev. Lett.*, 68:2512, 1992.

[73] Y. M. Blanter and M. Büttiker. Shot noise in mesoscopic conductors. *Physics Reports*, 336(1–2):1 – 166, 2000.

[74] Y. Zhu, J. Maciejko, T. Ji, H. Guo, and J. Wang. Time-dependent quantum transport: Direct analysis in the time domain. *Phys. Rev. B*, 71:075317, 2005.

[75] E. C. Cuansing and G. Liang. Time-dependent quantum transport and power-law decay of the transient current in a nano-relay and nano-oscillator. *Journal of Applied Physics*, 110(8):083704, 2011.

[76] A. Prociuk and B. D. Dunietz. Modeling time-dependent current through electronic open channels using a mixed time-frequency solution to the electronic equations of motion. *Physical Review B*, 78:165112, 2008.

[77] J. Maciejko, J. Wang, and H. Guo. Time-dependent quantum transport far from equilibrium: An exact nonlinear response theory. *Phys. Rev. B*, 74:085324, 2006.

[78] A. Croy and U. Saalmann. Propagation scheme for nonequilibrium dynamics of electron transport in nanoscale devices. *Phys. Rev. B*, 80:245311, 2009.

[79] D. Hou, Y. He, X. Liu, J. Kang, J. Chen, and R. Han. Time-dependent transport: Time domain recursively solving NEGF technique. *Physica E*, 31:191, 2006.

[80] Y. Wei and J. Wang. Current conserving nonequilibrium ac transport theory. *Phys. Rev. B*, 79:195315, 2009.

[81] D. Kienle, M. Vaidyanathan, and F. Léonard. Self-consistent ac quantum transport using nonequilibrium Green functions. *Phys. Rev. B*, 81:115455, 2010.

[82] Y. Wang, C.-Y. Yam, Th. Frauenheim, G. H. Chen, and T. A. Niehaus. An efficient method for quantum transport simulations in the time domain. *Chemical Physics*, 391(1):69 – 77, 2011.

[83] J. Wang. Time-dependent quantum transport theory from nonequilibrium green's function approach. *Journal of Computational Electronics*, 12(3):343–355, 2013.

[84] H. Xie, F. Jiang, H. Tian, X. Zheng, Y. Kwok, S. Chen, C. Yam, Y. Yan, and G. Chen. Time-dependent quantum transport: An efficient method based on Liouville-von-Neumann equation for single-electron density matrix. *The Journal of Chemical Physics*, 137(4):044113, 2012.

[85] I. Knezevic and B. Novakovic. Time-dependent Transport in Open Systems Based on Quantum Master Equations. *J. Comput. Electron.*, 12(3):363–374, 2013.

[86] P. Bokes, F. Corsetti, and R. W. Godby. Stroboscopic Wave-Packet Description of Nonequilibrium Many-Electron Problems. *Phys. Rev. Lett.*, 101:046402, 2008.

[87] M. Konôpka and P. Bokes. Stroboscopic wave packet description of time-dependent currents through ring-shaped nanostructures. *The European Physical Journal B*, 86(3):1–15, 2013.

[88] G. Stefanucci and C. O. Almbladh. Time-dependent partition-free approach in resonant tunneling systems. *Physical Review B*, 69:195318, 2004.

[89] E. Perfetto, G. Stefanucci, and M. Cini. Time-dependent transport in graphene nanoribbons. *Phys. Rev. B*, 82:035446, 2010.

[90] G. Stefanucci, S. Kurth, A. Rubio, and E. K. U. Gross. Time-dependent approach to electron pumping in open quantum systems. *Physical Review B*, 77:075339, 2008.

[91] E. Khosravi, S. Kurth, G. Stefanucci, and E. K. U. Gross. The role of bound states in time-dependent quantum transport. *Applied Physics A: Materials Science & Processing*, 93:355, 2008.

[92] J. Schwinger. Brownian motion of a quantum oscillator. *Sov. Phys. JETP*, 2:407, 1961.

[93] L. P. Kadanoff and G. Baym. *Quantum Statistical Mechanics*. Benjamin, New York, 1962.

[94] S. Datta. *Electronic Transport in Mesoscopic Systems*. Cambridge University Press, 1997.

[95] M. Wimmer. *Quantum transport in nanostructures: From computational concepts to spintronics in graphene and magnetic tunnel junctions*. PhD thesis, Universität Regensburg, 2006.

[96] C. W. Groth, M. Wimmer, A. R. Akhmerov, and X. Waintal. Kwant: a software package for quantum transport. *New Journal of Physics*, 16(6):063065, 2014.

[97] I. Rungger and S. Sanvito. Algorithm for the construction of self-energies for electronic transport calculations based on singularity elimination and singular value decomposition. *Phys. Rev. B*, 78:035407, 2008.

[98] D. S. Fisher and P. A. Lee. Relation between conductivity and transmission matrix. *Phys. Rev. B*, 23:6851–6854, 1981.

[99] G. Stefanucci and R. van Leeuwen. *Nonequilibrium Many-Body Theory of Quantum Systems: A Modern Introduction*. Cambridge University Press, Cambridge, 2013.

[100] F. Mahfouzi, J. Fabian, N. Nagaosa, and B. K. Nikolić. Charge pumping by magnetization dynamics in magnetic and semimagnetic tunnel junctions with interfacial rashba or bulk extrinsic spin-orbit coupling. *Phys. Rev. B*, 85:054406, 2012.

[101] M. Büttiker. Four-terminal phase-coherent conductance. *Phys. Rev. Lett.*, 57:1761–1764, 1986.

[102] L. M. Delves and J. L. Mohamed. *Computational methods for integral equations*. Cambridge University Press, 1988.

[103] K. Kazymyrenko and X. Waintal. Knitting algorithm for calculating Green functions in quantum systems. *Phys. Rev. B*, 77:115119, 2008.

[104] S. Li, S. Ahmed, G. Klimeck, and E. Darve. Computing entries of the inverse of a sparse matrix using the FIND algorithm. *Journal of Computational Physics*, 227:9408, 2008.

[105] D. E. Petersen and S. Li and K. Stokbro and H. H. B. Sørensen and P. C. Hansen and S. Skelboe and E. Darve. A hybrid method for the parallel computation of Green's functions. *Journal of Computational Physics*, 228:5020 – 5039, 2009.

[106] E. Bettelheim, A. G. Abanov, and P. Wiegmann. Nonlinear Quantum Shock Waves in Fractional Quantum Hall Edge States. *Phys. Rev. Lett.*, 97:246401, 2006.

[107] E. Bettelheim and L. Glazman. Quantum ripples over a semiclassical shock. *Phys. Rev. Lett.*, 109:260602, 2012.

[108] I. V. Protopopov, D. B. Gutman, P. Schmitteckert, and A. D. Mirlin. Dynamics of waves in one-dimensional electron systems: Density oscillations driven by population inversion. *Phys. Rev. B*, 87:045112, 2013.

[109] M. Büttiker. Absence of backscattering in the quantum Hall effect in multiprobe conductors. *Phys. Rev. B*, 38:9375–9389, 1988.

[110] G. B. Lesovik and L. S. Levitov. Noise in an ac biased junction: Nonstationary Aharonov-Bohm effect. *Phys. Rev. Lett.*, 72:538–541, 1994.

[111] H. W. Ivanov, D. A.and Lee and L. S. Levitov. Coherent states of alternating current. *Phys. Rev. B*, 56:6839–6850, 1997.

[112] B. J. van Wees, L. P. Kouwenhoven, C. J. P. M. Harmans, J. G. Williamson, C. E. Timmering, M. E. I. Broekaart, C. T. Foxon, and J. J. Harris. Observation of zero-dimensional states in a one-dimensional electron interferometer. *Phys. Rev. Lett.*, 62:2523–2526, 1989.

[113] P. Roulleau, F. Portier, P. Roche, A. Cavanna, G. Faini, U. Gennser, and D. Mailly. Direct Measurement of the Coherence Length of Edge States in the Integer Quantum Hall Regime. *Phys. Rev. Lett.*, 100:126802, 2008.

[114] K. v. Klitzing, G. Dorda, and M. Pepper. New Method for High-Accuracy Determination of the Fine-Structure Constant Based on Quantized Hall Resistance. *Phys. Rev. Lett.*, 45:494–497, 1980.

[115] A. Hartland, K. Jones, J. M. Williams, B. L. Gallagher, and T. Galloway. Direct comparison of the quantized Hall resistance in gallium arsenide and silicon. *Phys. Rev. Lett.*, 66:969–973, 1991.

[116] T. J. B. M. Janssen, A Tzalenchuk, S Lara-Avila, S Kubatkin, and V I Fal'ko. Quantum resistance metrology using graphene. *Reports on Progress in Physics*, 76(10):104501, 2013.

[117] D. R. Hofstadter. Energy levels and wave functions of Bloch electrons in rational and irrational magnetic fields. *Phys. Rev. B*, 14:2239–2249, 1976.

[118] R. L. Willett, C. Nayak, K. Shtengel, L. N. Pfeiffer, and K. W. West. Magnetic-Field-Tuned Aharonov-Bohm Oscillations and Evidence for Non-Abelian Anyons at ν=5/2. *Phys. Rev. Lett.*, 111:186401, 2013.

[119] D. B. Chklovskii, B. I. Shklovskii, and L. I. Glazman. Electrostatics of edge channels. *Phys. Rev. B*, 46:4026–4034, 1992.

LIST OF PUBLICATIONS

- — *AC Josephson effect without superconductivity*, B. Gaury, J. Weston, and X. Waintal, arXiv:1407.3911, (2014).
- — *Classical and quantum spreading of a charge pulse*, B. Gaury, J. Weston, C. Groth and X. Waintal, Proceedings to IEEE 17th International Workshop on Computational Electronics 2014, 1–4.
- — *Stopping electrons with radio-frequency pulses in the quantum Hall regime*, B. Gaury, J. Weston and X. Waintal, arXiv:1405.3520, to appear in Phys. Rev. B Rapid Communications (2014).
- — *Dynamical control of interference using voltage pulses in the quantum regime*, B. Gaury and X. Waintal, Nat. Commun., **5**, 3844 (2014).
- — *Numerical simulations of time resolved quantum electronics*, B. Gaury, J. Weston, M. Santin, M. Houzet, C. Groth and X. Waintal, Phys. Rep. **531**, 1, 1–37 (2014).

With the recent technical progress, single electron sources have moved from theory to the lab. Conceptually new types of experiments where one probes directly the internal quantum dynamics of the devices are within grasp. In this thesis we develop the analytical and numerical tools for handling such situations. The simulations require appropriate spatial resolution for the systems, and simulated times long enough so that one can probe their internal characteristic times. So far the standard theoretical approach used to treat such problems numerically—known as Keldysh or NEGF (Non Equilibrium Green's Functions) formalism—has not been very successful mainly because of a prohibitive computational cost. We propose a reformulation of the NEGF technique in terms of the electronic wave functions of the system in an energy–time representation. The numerical algorithm we obtain scales now linearly with the simulated time and the volume of the system, and makes simulation of systems with $10^5 - 10^6$ atoms/sites feasible. We leverage this tool to propose new intriguing effects and experiments. In particular we introduce the concept of dynamical modification of interference pattern of a quantum system. For instance, we show that when raising a DC voltage V to an electronic interferometer, the transient current response oscillates as $\cos(eVt/\hbar)$. We expect a wealth of new effects when nanoelectronic circuits are probed fast enough. The tools and concepts developed in this work shall play a key role in the analysis and proposal of upcoming experiments.

Keywords: quantum transport, time-dependent, numerics, interference

Grâce aux progrès techniques récents, les sources d'électrons uniques sont passées de la théorie au laboratoire. Des expériences conceptuellement nouvelles où l'on sonde directement la dynamique quantique interne des systèmes sont désormais possibles. Dans cette thèse nous développons les outils analytiques et numériques pour analyser et comprendre ces problèmes. Les simulations requièrent une résolution spatiale appropriée pour les systèmes, et des temps simulés suffisament longs pour sonder leurs temps caractéristiques. Jusqu'à présent l'approche théorique standard utilisée pour traiter de tels problèmes numériquement—connue sous les dénominations de formalisme Keldysh ou NEGF (Fonctions de Green Hors Equilibre)—n'a pas été très fructueuse, principalement à cause du coût en temps de calcul prohibitif. Nous proposons une reformulation de cette technique sous la forme des fonctions d'onde électroniques du système dans une représentation énergie–temps. Le coût de calcul de notre algorithme numérique est maintenant linéaire avec le temps simulé et le volume du système, rendant possible la simulation de système contenant $10^5 - 10^6$ atomes/sites. Nous utilisons cet outil pour proposer de nouveaux effets intrigants ainsi que des expériences. Nous introduisons la modification dynamique du motif d'interférence d'un système quantique. Nous montrons, par exemple, que la montée d'une tension DC V sur un interféromètre électronique produit un régime transitoire où le courant oscille comme $\cos(eVt/\hbar)$. Nous prévoyons une grande variété d'effets nouveaux lorsque les circuits de nanoélectronique sont sondés très rapidement. Les outils et concepts développés dans cette thèse auront un rôle clé dans l'analyse et les propositions des expériences à venir.

Mots-clés : transport quantique, dynamique, numérique, interférence